Okinawa Institute of Science and Technology
Graduate University

Thesis submitted for the degree

Doctor of Philosophy

Spatially and temporally resolved microscopy of traps in hybrid organic-inorganic perovskites

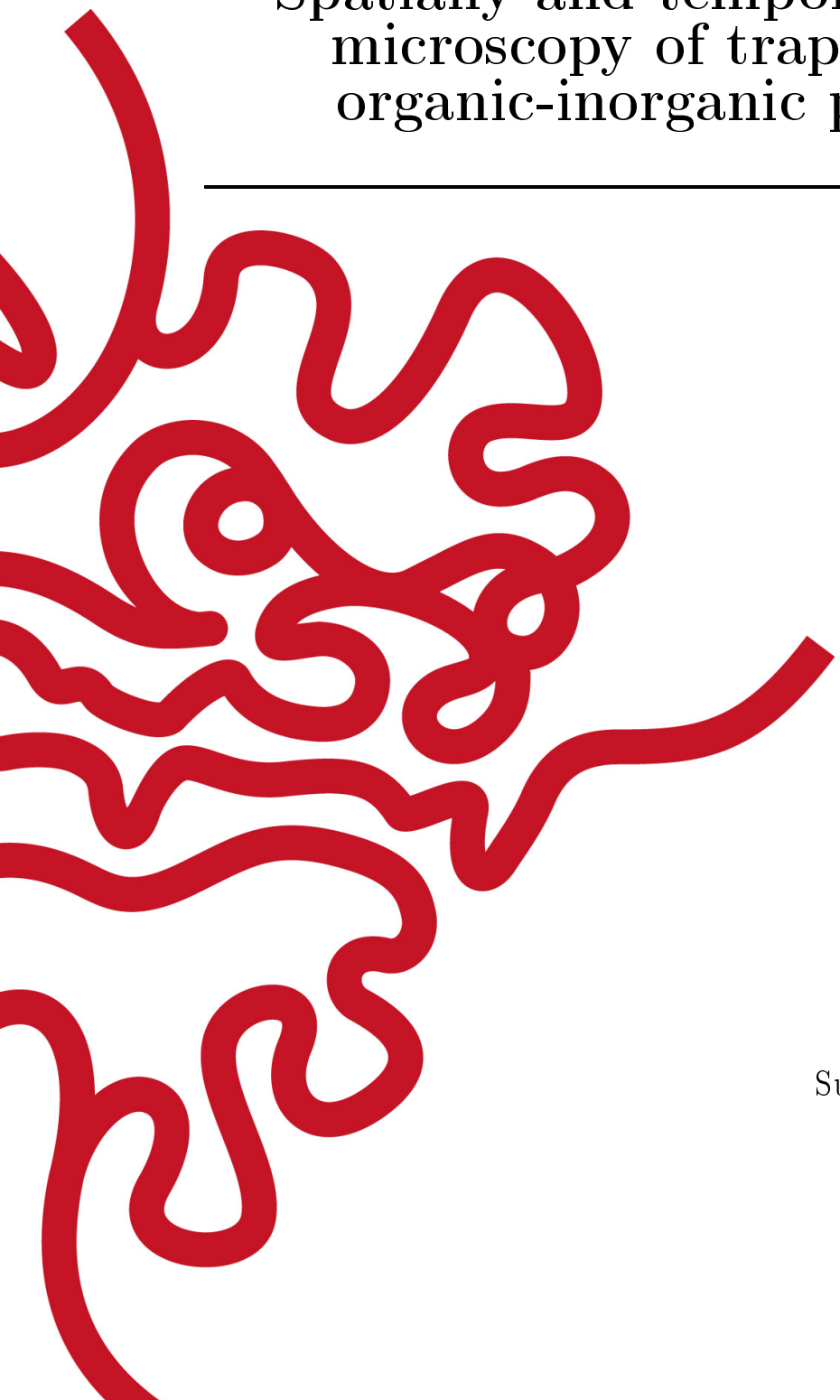

by

Andrew J. Winchester

Supervisor: **Keshav M. Dani**

October, 2020

Declaration of Original and Sole Authorship

I, Andrew J. Winchester, declare that this thesis entitled *Spatially and temporally resolved microscopy of traps in hybrid organic-inorganic perovskites* and the data presented in it are original and my own work.

I confirm that:

- No part of this work has previously been submitted for a degree at this or any other university.
- References to the work of others have been clearly acknowledged. Quotations from the work of others have been clearly indicated, and attributed to them.
- In cases where others have contributed to part of this work, such contribution has been clearly acknowledged and distinguished from my own work.
- None of this work has been previously published elsewhere, with the exception of the following:
  - "Performance-limiting nanoscale trap clusters at grain junctions in halide perovskites", T. A. S. Doherty, A. J. Winchester, et al., Nature 580, 360-366 (2020)

Date: October, 2020

Signature: 

Abstract

Spatially and temporally resolved microscopy of traps in hybrid organic-inorganic perovskites

In recent years the class of materials known as hybrid organic-inorganic perovskite (HOIP) have received notable attention for use in photovoltaic applications, with record solar conversion efficiencies reaching other established thin film systems. Despite their rapid development, there are still ongoing issues related to heterogeneous film properties which limit device performance. It has been suggested that sites which capture charge carriers (traps) could be localized on a micrometer or smaller size scale, leading to regions of poor efficiency. Understanding the electronic properties of such regions, in particular on how they influence carrier recombination, will therefore provide crucial information about the carrier loss pathways in HOIP films, which will be essential for developing new strategies to minimize losses and create more efficient devices. In order to gain information about the ultrafast charge carrier recombination dynamics on nanoscale length scales, specialized techniques which can provide information with both high spatial and temporal resolution will be necessary. Here, we utilize time resolved photoemission electron microscopy (TR-PEEM) as a novel technique to study the nanoscale ultrafast properties of photo excited carriers and their relation to heterogeneous film properties in HOIP thin film materials. Following this overall theme, the work in this thesis will address several nanoscale properties and phenomenon. First, we will uncover the nanoscale distribution of carrier traps in a HOIP film which result in non-radiative losses. We then will describe in depth the ultrafast carrier trapping processes happening at nanoscale trap clusters. Following this, we will then discuss other novel information and studies on the traps in HOIP which can be realized using TR-PEEM, namely on effects of light treatments and morphological information. By gaining a deeper understanding in these directions, we hope to contribute to the broader goal of improving HOIP photovoltaic device efficiency and showcase TR-PEEM as a novel technique for studying photocarrier dynamics in semiconductor materials.

Acknowledgment

This thesis work would not have been possible without the contributions of so many people, whom I would like to acknowledge below.

I would first like to thank Stuart Macpherson (Cambridge) for helping to analyze and interpret the trapping kinetics and for his ideas, help, and work in the project studying light-soaking effects using PEEM, which we worked together on during his visit to OIST under a JSPS fellowship. I also thank him for providing perovskite samples and taking photoluminescence data. In addition, I want to also thank him for his help in preparing the first manuscript submitted from this thesis work, as well as for all the fruitful and interesting scientific discussions related to perovskites and TR-PEEM.

I would next like to thank Tiarnan Doherty (Cambridge) for his discussions about perovskite materials, in particular about their nanoscale properties such as strain, composition, and crystal structure. I thank him immensely for his part of our collaborative work to understand these properties as related to my PEEM and TR-PEEM results, which has resulted in our shared first-authorship *Nature* paper, which he also contributed writing to.

I thank Dr. E Laine Wong (OIST) for working together with me during the beginning of my thesis work as we learned and developed the instrumentation, analysis, and interpretation behind using the TR-PEEM technique at OIST. I also want to thank her for teaching me about ultrafast optics and for mentoring me as the senior (and first) graduate student from our group.

I next thank Vivek Pareek (OIST), who was largely responsible for building the third and fourth harmonic generation setup used throughout this thesis work in PEEM and TR-PEEM measurements, without which most, if not all of the measurements shown here would have been impossible or impractical. I also thank him for taking photoluminescence data, for many discussions about ultrafast carrier recombination processes and interactions in semiconductors, and lastly for moral support during my thesis work.

I also thank Dr. Mojtaba Abdi-Jalebi (Cambridge) and Zahra Andaji-Gamaroudi (Cambridge) for preparing and sending perovskite samples, especially at the beginning of this thesis work.

I would also like to thank Sonya Kosar (OIST) for learning and continuing to explore with TR-PEEM several of the ideas and directions started from this thesis work, as well as for moral support. In particular, I want to thank her for her work in taking and analyzing the high-resolution PEEM images which contributed greatly towards our publication in *Nature*.

I next need to thank Dr. Michael Man (OIST) for teaching me so much of the detail and intricacies behind using, maintaining, and interpreting LEEM and PEEM experiments and instrumentation. I also thank him for his hard work in establishing TR-PEEM within our group. I thank him for his help with interpretation and analysis of data, including help with computer programming. I lastly thank him for being a scientific role model and mentor for me during my thesis.

I next thank Dr. Julien Madéo (OIST) for teaching me so much about ultrafast optics, lasers, and carrier recombination processes in condensed matter. I also thank him for helping Vivek Pareek to build and design the third and fourth harmonic generation setup. Lastly, I thank him for his help in keeping the laser system central to my experiments running in good condition and teaching me how to maintain it.

I thank Dr. Chris Petoukhoff (OIST) for his help with interpreting data and for his discussions about perovskite and organic photovoltaic materials.

I thank Prof. Bala Murali Krishna Mariserla (OIST) for teaching me about ultrafast optics and laser systems.

I thank Prof. Samuel Stranks (Cambridge) for providing us the opportunity to study his group's perovskite material, helping interpret our results and to identify and direct the interesting and relevant points of our results to the perovskite community. I also thank him for his help with preparing the first manuscript submitted from this thesis work and for many useful and interesting discussions about perovskite materials and photovoltaic applications.

In, addition, I would like to thank Prof. Samuel Stranks and the rest of his group at Cambridge for their hospitality and interesting scientific discussions during my visit there.

I would lastly like to thank Prof. Keshav Dani (OIST) for providing me the opportunity to undertake a very unique and challenging thesis project in his group and for his help in directing this research for the very young field of TR-PEEM in semiconductors, which has been a very challenging and rewarding task for everyone involved. I thank him for his guidance in directing, analyzing, and interpreting the research. I also thank him for teaching me about ultrafast optics and lasers, his help with preparing the manuscript submitted from this thesis work, as well as his help and guidance in writing scientific documents, preparing for conference presentations, and in choosing career paths.

I especially want to thank Prof. Keshav Dani for creating the environment of the Femtosecond Spectroscopy Unit (FSU) at OIST, who has become like a second family. Together, the FSU has shared in the joys, excitement, and hardships of research at a newly established university. I am deeply grateful for the support of the FSU during my thesis work.

And last, but not least, I also thank my parents and family for their love and support throughout my thesis work. I deeply appreciate that they have continued supporting me throughout my academic life so far, even despite being a (literal) world apart after moving to Japan for my thesis.

皆さん、本当にありがとうございました！

Abbreviations

AFM	atomic force microscopy
ARPES	angle resolved photoemission spectroscopy
BBO	beta barium borate
BP	band pass
Br	bromine
CB	conduction band
CCD	charge coupled device
Cs	cesium
EQE	external quantum efficiency
eV	electron volt
FA	formamidinium
FOV	field of view
fs	femtosecond
FTO	fluorine tin oxide
FWHM	full width at half maximum
GaAs	gallium arsenide
HeNe	Helium Neon
HOIP	hybrid organic-inorganic perovskite
I-Br	iodine and bromine mixed cation HOIP
I-only	iodine only mixed cation HOIP
IR	infrared
ITO	indium tin oxide
K-pass	potassium passivated mixed cation mixed halide HOIP
LED	Light Emitting Diode
LEEM	low energy electron microscopy
MA	methylammonium
$MAPbI_3$	methylammonium lead iodide
nm	nanometer
ns	nanosecond
O_2	oxygen (gas)
Pb	lead
PEEM	photoemission electron microscopy
PL	photoluminescence
ps	picosecond
PV	photovoltaic
QE	quantum efficiency

SED	scanning electron diffraction
SEM	scanning electron microscopy
SRH	Shockley-Read-Hall
TEM	transmission electron microscopy
TR-PEEM	time-resolved photoemission electron microscopy
UHV	ultra high vacuum
UPS	ultraviolet photoelectron spectroscopy
UV	ultraviolet
VB	valence band
XRD	x-ray diffraction
XRF	x-ray fluorescence
XPS	x-ray photoelectron spectroscopy

Contents

Declaration of Original and Sole Authorship iii

Abstract v

Acknowledgment vii

Abbreviations ix

Contents xi

List of Figures xiii

List of Tables xv

Introduction 1

1 Hybrid organic-inorganic perovskites 3
1.1 Photovoltaic properties and development of HOIP . . . 3
1.2 Fundamental limits and issues . . . 4
1.3 Triple cation perovskite . . . 6

2 Time resolved photoemission electron microscopy 11
2.1 Photoemission electron microscopy . . . 11
2.1.1 General photoemission process . . . 11
2.1.2 Photoemission microscopy . . . 13
2.2 Time-resolved photoemission electron microscopy . . . 17
2.3 Considerations for TR-PEEM . . . 22
2.3.1 Space Charge . . . 22
2.3.2 Laser Noise . . . 24
2.3.3 Signal Interpretation . . . 26
2.4 PEEM Discussion . . . 28

3 Photoemission microscopy and spectroscopy of HOIP 29
3.1 PEEM imaging of heterogeneity . . . 29
3.2 Photoemission spectroscopy of trap states . . . 32
3.3 Discussion of trap origins and implications . . . 36

4 Steady-state recombination losses **39**
4.1 PL microscopy 39
4.2 Correlations between PL and trap sites 42
4.3 Non-radiative loss discussion 44

5 Time-resolved microscopy of trapping dynamics **47**
5.1 Time Resolved Imaging 47
5.2 Trapping Kinetics 52
5.2.1 Fluence Dependence 52
5.2.2 Trap Assisted Auger 56
5.2.3 Diffusion Limited Trapping 60
5.3 Time-resolved discussion 69

6 Light and Environmental Control of Traps **71**
6.1 In-situ light exposure 71
6.2 Ex-situ environmental exposure 74
6.3 Light-treatment Discussion 77

7 Film morphology from PEEM **81**

Conclusion **85**

Bibliography **87**

List of Figures

1.1 Perovskite Structure 4
1.2 QE SRH rates 5
1.3 Triple Cation Sample 7
1.4 Triple Cation Perovskite Morphology 8

2.1 Photoemission Schematic 12
2.2 PEEM diagram 14
2.3 Time Resolved Photoemission 18
2.4 Laser Spectrum 19
2.5 TR-PEEM Diagram 20
2.6 Space Charge Images 23
2.7 Space Charge Spectrum 23
2.8 Laser Stability and Noise 25
2.9 GaAs signal example 27

3.1 PEEM images of HOIP 30
3.2 Spot statistics 31
3.3 PES of HOIP Traps 33
3.4 PES comparison 34
3.5 Equilibrium energy diagrams 35

4.1 Iodine-only PL map 40
4.2 Iodine-only PL-PEEM overlay 41
4.3 Mixed-halide PL-PEEM overlays 42
4.4 PL-PEEM correlations 43
4.5 PL-PEEM statistics correlations 45

5.1 TR-PEEM Images 48
5.2 TR-PEEM dynamics 49
5.3 Time constant dependence on intensity 51
5.4 Fluence dependent TR-PEEM 53
5.5 Fluence dependence of TR-PEEM fitting 55
5.6 Trap Assisted Auger Dynamics 58
5.7 Trap Assisted Auger Coefficients 59
5.8 Diffusion limited trapping 62
5.9 Kinetic diffusion-trapping solutions 64
5.10 Diffusion simulation with de-trapping included 65

5.11 2D Diffusion Schematic 67
5.12 2D Diffusion Simulation 68

6.1 In-situ Light Soaking Images 72
6.2 In-situ Light Soaking Photoemission Spectroscopy 73
6.3 Ex-situ Light Soaking in Oxygen Images 75
6.4 Ex-situ Light Soaking in Oxygen Photoemission Spectroscopy 76
6.5 Trapping Kinetics after ex-situ Light Soaking in Oxygen 78

7.1 AFM and PEEM comparison 82
7.2 High resolution PEEM imaging 83

List of Tables

5.1 Double exponential fit results at fixed 1.55 eV pump fluences 50

Introduction

Over the course of the latter half of the twentieth and ongoing into the twenty first century, there has been a growing push to pursue and develop "green", or more specifically, alternate, renewable, and efficient energy sources. In particular, solar cell technologies have been one of the most prominent solutions towards achieving "green" energy. The development of solar cells since the demonstration of practical silicon-based devices by Bell labs in the 1950s [1] is one full of new materials, advanced processing methods, and device design and architecture. However, one of the important challenges, central to the operation of all solar cells and photovoltaic (PV) devices, is overcoming the effects of unwanted charge carrier losses within the absorbing material. In particular, understanding the properties of defects which act as charge carrier trapping and recombination centers within the solar material is central to achieving higher device efficiency. Park, *et al.* [2] recently gave a nice overview of the development of defect understanding in silicon, thin-film, and the currently expanding field of hybrid organic-inorganic perovskite (HOIP) materials, which underlines the importance of understanding how defects influence the properties of solar cell devices. One of the surprising discoveries about HOIP materials has been that despite the relatively high density of carrier traps measured (as compared to inorganic photovoltaic materials), quite good performance can be achieved in thin film devices [3]. However, most HOIP devices still operate in a regime where the efficiency is limited by unwanted recombination losses. Hence, understanding the details behind the properties of defects and their role on carrier trapping has become a greater research focus over the last few years, as solving issues related to carrier traps still represents an important direction for improving future devices.

Stepping back for a moment, it is also important to consider how advances in material understanding have been linked to improvements in experimental tools and techniques. In particular, advances in electron microscopy techniques have seen tremendous success for material study. In the last two decades, a new sub-field of electron microscopy has started to emerge, following the availability of commercial ultrafast pulsed laser sources, which is known generally or loosely as time-resolved or ultrfast electron microscopy. This provides ways to perform high spatial resolution imaging of dynamic events on time scales down to picoseconds, femtoseconds, or potentially even attoseconds, which are the relevant time scales for studying many electronic processes in materials. The most well known example is that of 4-dimensional electron microscopy using transmission electron microscopy (TEM) [4], where electron pulses are generated and used to image samples. However, there are several related techniques emerging in this field which offer different strengths and possibilities. In particular, the technique of time-resolved photoemission electron microscopy (TR-PEEM) is well

suited for studying the nanoscale dynamics of photoexcited carriers in semiconductors [5], where pulses of light are used to emit electrons from the sample itself that are then imaged in the microscope. This technique has only recently started being applied to semiconductor materials, and offers new avenues for understanding the relaxation of excited states in matter and in particular in heterogeneous systems, where nanoscale material differences, charge transfer, and interactions will be of interest.

With these two general ideas in mind, the overall goal of my thesis work was then to gain insight into the properties and recombination processes of defects in HOIP materials by application of an ultrafast electron microscopy technique, namely TR-PEEM. In the following chapters of this thesis, I will first discuss in more detail the properties of the HOIP materials studied in relation to their use in solar cell devices and ongoing issues in chapter 1. I will then introduce in depth the methodology behind TR-PEEM and discuss its merits and limits in chapter 2. In chapters 3 and 4, I will show the first major results of my work on using steady-state PEEM to identify nanoscale traps in HOIP thin films and their effects on non-radiative carrier losses, respectively. I will then discuss the results of my TR-PEEM measurements in studying the recombination processes at these trap sites in chapter 5. Following the development of our understanding of the traps in these HOIP films, the last two chapters will focus on other directions and applications of PEEM and TR-PEEM for understanding the defect nature in these films. In chapter 6, I will show how PEEM can be used to study the light-soaking phenomenon often seen in HOIP films, while in chapter 7 I will show the possibility for using PEEM to observe the heterogeneous grain morphology in-situ. Finally, I will end the thesis by summarizing the main results of my work, as well as the ideas and implications arising from them in the conclusion.

Chapter 1

Hybrid organic-inorganic perovskites

The aim of this chapter will be to review and highlight the important properties and discoveries related to hybrid organic-inorganic perovskite (HOIP) materials in order to motivate the research direction of the rest of the thesis. In section 1.1 I will introduce the general properties and use of HOIP materials in relation to their photovoltaic applications. In section 1.2, I will then discuss some of the relevant and ongoing fundamental issues towards their use in solar cells. I will lastly discuss more specifically in section 1.3 the general properties of the triple cation samples studied in this thesis.

1.1 Photovoltaic properties and development of HOIP

HOIP are a class of material which has recently seen tremendous interest for use in photovoltaic applications. They follow the general chemical formula for the perovskite crystal structure of ABX_3, where the A and B species are cations and the X species is an anion. This forms a crystal structure comprised of BX_6 octahedra which surround the A cation, as depicted in figure 1.1. In order to satisfy the perovskite structure, the radii of the different ions (R_A, R_B, R_X) generally follow the Goldschmidt tolerance factor t [6], ranging between 0.8 and 1, where $t = \frac{R_A+R_B}{\sqrt{2}(R_B+R_X)}$. Perovskites containing organic cations were first extensively studied starting from the late 1970s [7]. These HOIPs typically have halide anions (X) such as chlorine (Cl^-), bromine (Br^-), or iodine (I^-) and metal cations (B) such as lead (Pb^{2+}) or tin (Sn^{2+}) forming the inorganic part. The remaining cation (A) is then a small organic molecule such as methylammonium ($CH_3NH_3^+$, MA^+) or formamidinium ($HC(NH_2)_2^+$, FA^+). However, it wasn't until the work by Kojima, *et al.* in 2009 where the application of HOIPs towards photovoltaic applications was first demonstrated, resulting in a HOIP-sensitized solar cell with about 3.8% conversion efficiency [8].

Following the first demonstration by Kojima, there was a tremendous increase in using HOIP materials when it was realized they could be fabricated in a thin-film solid state device [9–11]. The ability to construct such a solar cell with good efficiency is due to the combination of several desirable properties that HOIP materials were found to possess. First and foremost, they have direct band gap transitions with energies between 1.5-3.1 eV [12]. Accordingly, the absorption coefficient in the visible part of the spectrum is quite high for these materials, and may also be enhanced due to excitonic

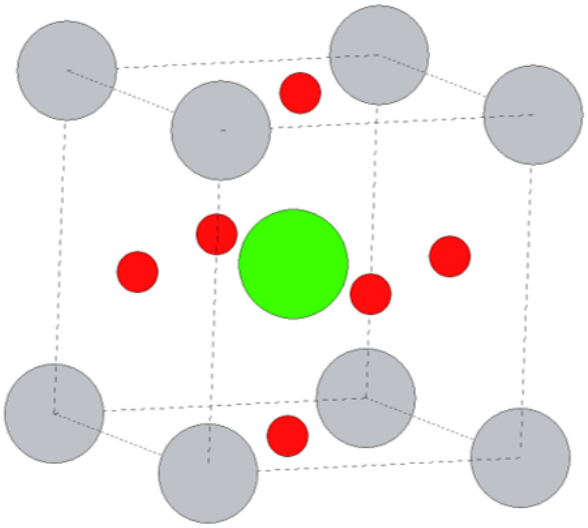

Figure 1.1: Crystal structure of perovskite. Green and gray spheres are the A and B cations, while the smaller red spheres are the X anions.

effects [12]. This makes HOIP materials excellent absorbers for much of the solar spectrum and allows even for thin films ($< 1\ \mu m$) to absorb a large fraction of incident light. Second, it was found that HOIP films can have moderate charge carrier mobility with carrier lifetimes ranging from tens of nanoseconds to microseconds [13]. These result in large effective carrier diffusion lengths, reaching a micrometer or potentially longer [14, 15]. This implies that thin film HOIP devices should be very efficient at extracting photo-generated carriers from the solar material before they can recombine.

As another boon to their application, the composition of HOIPs can be continuously tuned in many cases by mixing the halide anions. This allows for direct control over the band gap, and leads to interesting applications such as tandem HOIP solar cells and light emitting diode (LED) devices [16]. Lastly, HOIP thin films can be readily produced through low temperature solution-based fabrication methods [11], making them very attractive for low cost and flexible solar cell applications. Together, this combination of properties has lead to the unprecedented development of HOIP solar cells over the last decade, with record device efficiencies improving from 3.8% in 2009 [8] to over 23% in single junction cells in 2019 [17], surpassing other established thin-film technologies and now competing with single crystal silicon cells.

1.2 Fundamental limits and issues

Despite the rapid development of HOIP based solar cells, there are however several ongoing fundamental and materials-related issues. One, in particular, is the complete understanding of the nature of defects or carrier traps in HOIP [2, 3, 19]. While traps in HOIP are often considered benign compared to traditional inorganic materials [2, 3], especially considering the low-temperature processing methods used, they are still very important to consider for device applications. For example, given the band gap of methylammonium lead iodide ($MAPbI_3$), the prototypical HOIP material, of

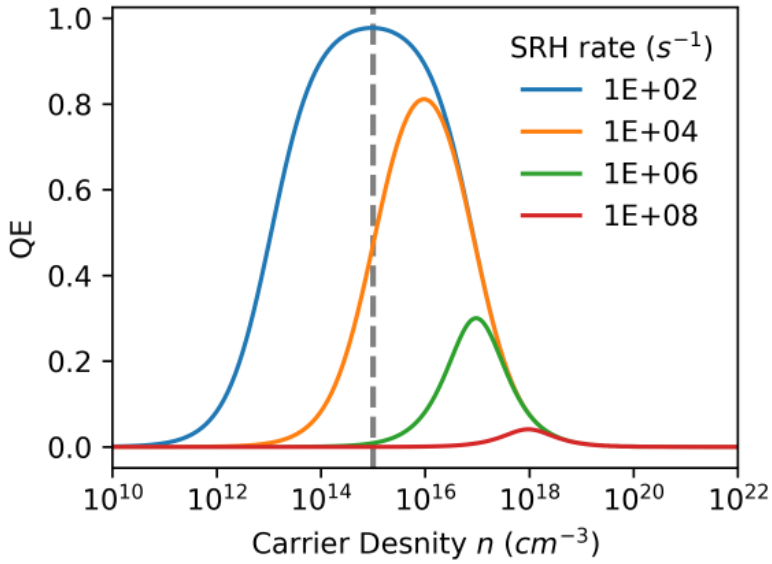

Figure 1.2: Calculated variation of QE at different rates of SRH recombination using equation 1.1. The B and C constants are taken from literature for $MAPbI_3$ [18]. The dashed gray line represents the approximate carrier density generated under a 1-sun illumination. The reduced QE at high carrier density is due to the increased rate of Auger recombination.

about 1.5 eV, a single junction solar cell under ideal conditions is predicted to achieve about 30% conversion efficiency [20]. The main limiting factor preventing current cells from reaching this efficiency is the presence of non-radiative carrier recombination [20], which acts as a loss channel that results in fewer carriers being harvested by the solar cell. In particular, Shockley-Reed-Hall (SRH) [21] recombination at deep energy levels is expected to contribute significantly to the losses when the illumination intensity is approximately 1-sun (about 1 W/m^2) [20]. Therefore, strategies to reduce or modify the carrier traps in HOIP are essential towards reaching performance limits. For example, as shown in figure 1.2 for different rates of SHR recombination, the calculated quantum efficiency (QE), or ratio of emitted photons (i.e. useful carrier recombination [20, 22]) to the total carrier recombination can change dramatically at the 1-sun intensity condition (dashed line). Here, the QE is given by:

$$QE = \frac{Bn^2}{An + Bn^2 + Cn^3} \tag{1.1}$$

Where n is the carrier density, and A, B, and C are the rate coefficients for SRH (monomolecular), radiative (bimolecular), and Auger (many-body) recombination processes [22]. B and C are generally fixed material properties, thus controlling A is the most significant way to affect the QE at lower carrier densities, as illustrated in figure 1.2. Hence, gaining a detailed understanding of carrier traps and how they affect recombination in these materials is necessary for engineering future devices.

One of the more common ways to asses carrier trapping in photovoltaic materials is through photoluminescence (PL) spectroscopy and microscopy. It provides a way to

asses the ratio of emitted photons to the total generated carriers, or external quantum efficiency (EQE, related to QE), which can be used to experimentally determine the steady-state recombination rates of the different processes [22]. This has been used, for example, to estimate the amount of SRH recombination in HOIP films [23, 24]. One of the interesting findings of PL microscopy measurements has been that the apparent carrier losses can have a significant spatial heterogeneity. Several works have identified that relative EQE can vary between adjacent or nearby material grains, which are often a few 100 nanometers to about a micrometer in size [25–29]. However, at this length scale the interpretation of PL measurements becomes more complicated for several reasons. First, PL measurements are limited in spatial resolution by the optical diffraction limit to typically around 300 nm, which is often comparable to or a significant fraction of a single grain. Second, as introduced in section 1.1, measurements have shown that the carrier diffusion length can reach micrometers. Thus, there are additional considerations on how individual grains are connected, which will greatly affect how carriers recombine spatially [27–29]. For example, two grains, one with a high density of traps, which are connected will effectively reduce the EQE of both grains and make interpretation complicated. Lastly, while PL is a useful tool, it ultimately only gives direct information about the radiative carrier recombination; non-radiative recombination processes have to be inferred. Due to these limitation, there is some disagreement and conflicting reports in the literature regarding the role of carrier traps, particularly at the grain boundaries [25, 27, 28], where traps might be expected to play a larger role [30].

To overcome these limitations, there is a need to utilize other methods which can access the spatial distribution of traps within the film. In addition, it would be beneficial to use methods which can also measure the recombination kinetics on fast time scales. This requires a method which has high spatial resolution (below visible optical diffraction limit), ability to distinguish trap sites, and high temporal sensitivity (femtosecond to picosecond). In light of these requirements, the technique which we are developing to achieve this is time resolved photoemission electron microscopy (TR-PEEM), which I will describe in detail in chapter 2.

1.3 Triple cation perovskite

After discussing the more general properties of HOIP materials in the previous two sections and before moving to the methods and results, I will discuss the properties of the specific samples used for the study in the rest of this thesis work. As mentioned in section 1.1, the ability to use mixtures of the halide ion (X) has been demonstrated for tuning the material properties. Beyond this, more recently it was found that the organic cation (A) can also use mixed compositions. In particular, certain mixtures of MA and FA with a small fraction of cesium (Cs) can satisfy the Goldschmidt tolerance factor and provide several benefits. These include much more stable films against degradation, more reproducible devices, additional band gap tuning, and reduced segregation of mixed halide compositions [31–33]. These improvements have resulted in higher performing solar cell devices overall.

Following this, we have chosen to focus our study on these triple cation HOIP

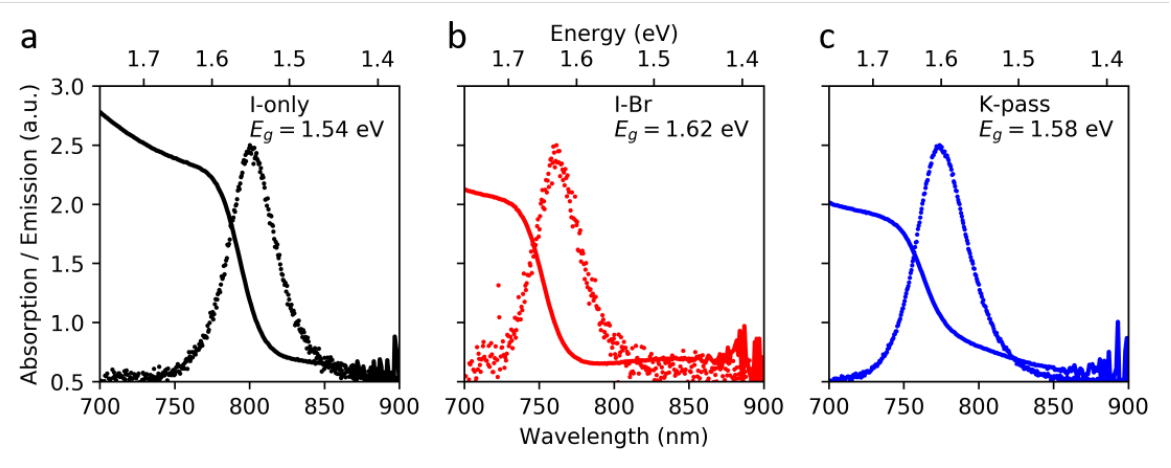

Figure 1.3: Optical characterization of the triple cation samples studied. Absorption (solid lines) and normalized PL emission (dots) from a) iodine only, b) I-Br, and c) K-passivated samples. The band gaps obtained from an extrapolation of the band edge absorption in a Tauc plot are shown in each panel. The absorption was measured with a Thermo Scientific Evolution 600 UV-VIS in transmission geometry. For PL, the excitation wavelength was 532 nm at an intensity of about 4 W/cm^2 in a confocal microscope setup (Nanofinder30, Tokyo Instruments) and averaged over an area of several micrometers.

films, which represent the cutting edge in materials development for PV applications. In this thesis work, I have looked at three slightly different compositions, consisting of $Cs_{0.05}FA_{0.78}MA_{0.17}PbI_3$ (iodine-only), mixed halide $Cs_{0.05}FA_{0.78}MA_{0.17}Pb(Br_{0.17}I_{0.83})_3$ (I-Br), and I-Br with 10% potassium (K) incorporation (K-passivated). These samples were all produced through a low temperature solution-process by our collaborator Prof. Stranks and his group at Cambridge [34] on indium tin oxide (ITO) or fluorine tin oxide (FTO) coated glass substrates. Film thickness were nominally 500 nm. All samples were produced, shipped, and stored under an inert nitrogen atmosphere to prevent exposure to oxygen and water contamination.

There are two main differences between these three samples. First, changing the halide ratio and potassium content slightly changes the band gap, as seen from the absorption and PL emission in figures 1.3 a-c. Second, incorporation of potassium greatly improves the radiative efficiency by reducing non-radiative losses in the film [34]. For these samples, we also have solution deposited gold platelets to use as position markers (figure 1.4 a), which allows us to measure the exact same sample area with different techniques, for example the scanning electron microscopy (SEM) image in figure 1.4 b. Lastly, I show SEM images of the I-only, I-Br, and K-pass films in figures 1.4 c, d, and e, respectively. From this, I find that the typical grain size is around 100-200 nm in the I-only sample, while it is slightly larger for the mixed halide compositions.

Now, following the basic characterization of these films and after introducing the general issue of understanding traps in these materials, I will spend some time in chapter 2 discussing the technique of TR-PEEM and how it will allow me to provide

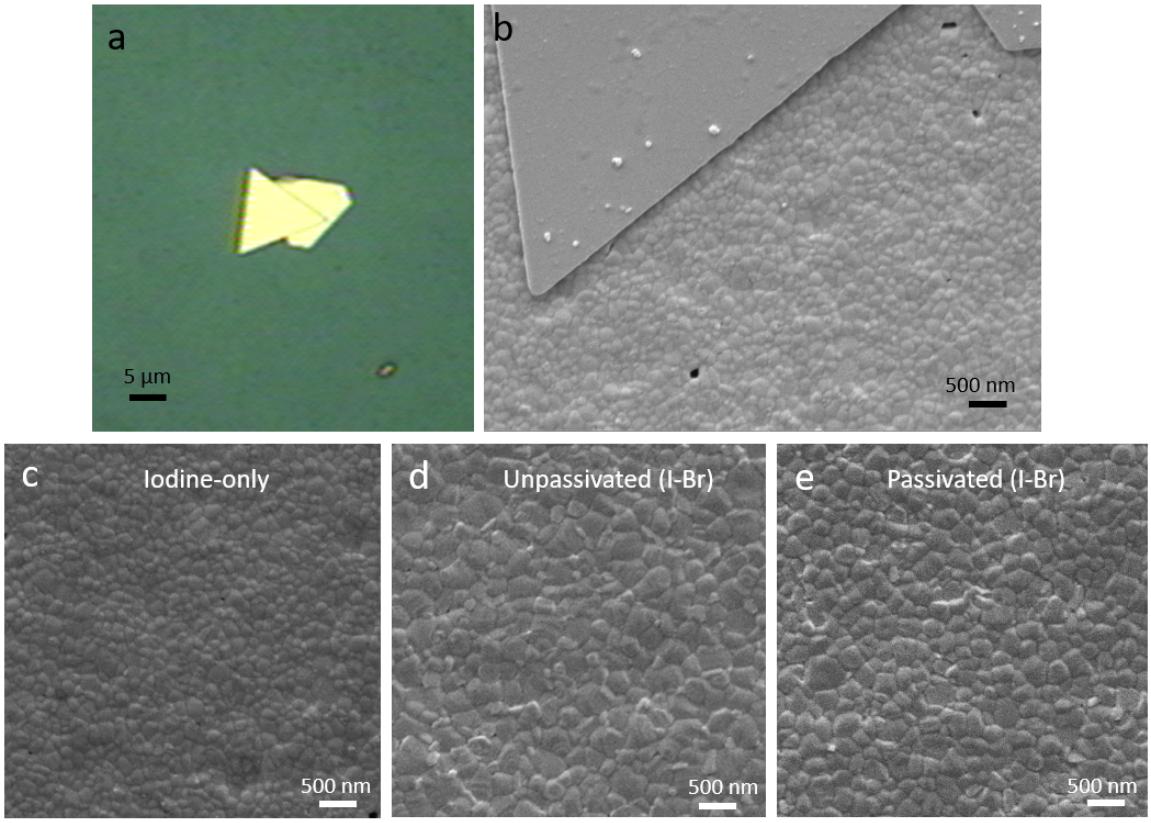

Figure 1.4: Morphology of the triple cation perovskite samples for this study. a) optical image of an I-only sample, showing a gold position marker. b) SEM image at 2 kV of the lower part of the same marker, where the grain structure is visible. c, d, e) SEM images at 2 kV, cropped to a 5 μm square for the I-only, I-Br, and K-pass samples.

insight into some of these issues.

Chapter 2

Time resolved photoemission electron microscopy

In this chapter, the focus will be to build the basis of operating principles and ideas behind time-resolved photoemission microscopy (TR-PEEM). Towards this goal, I will first introduce the standard photoemission process and principles behind photoemission electron microscopy (PEEM) in section 2.1. Then, I will make the extension to time-resolved measurements in section 2.2. I will then discuss in section 2.3 some of the challenges, limitations, and considerations for performing TR-PEEM measurements.

2.1 Photoemission electron microscopy

The basic operating principle behind PEEM is to image low energy electrons emitted by a material. There are several ways of producing such low energy electrons. Specifically for PEEM, as inferred from the name, the photoemission process is the main source of electrons for imaging. Thus, I will first give some introduction to photoemission before talking specifically about how it is used in PEEM imaging.

2.1.1 General photoemission process

The general process of photoemission is a very well known one, which is an application of the photoelectric effect originally observed, accurately described, and proved in the late 19th century and early 20th century by Hertz, Einstein, and Millikan. The effect states that photons with a large enough energy $h\nu$, where h is the Planck constant, impinging upon a material cause emission of electrons, termed photoelectrons, as shown in figure 2.1 a. The resulting photoelectrons escape the material with a kinetic energy KE which depends on the photon energy $h\nu$, material work function ϕ, and the bound state E_B of the electron before it left the material as:

$$KE = h\nu - E_B - \phi \tag{2.1}$$

For many materials ϕ is of the order 3-6 electronvolts (eV), and this represents the energy required to remove an electron from the system. This means that for photoemission to occur, the photon energy $h\nu$ should be at least as large as the work

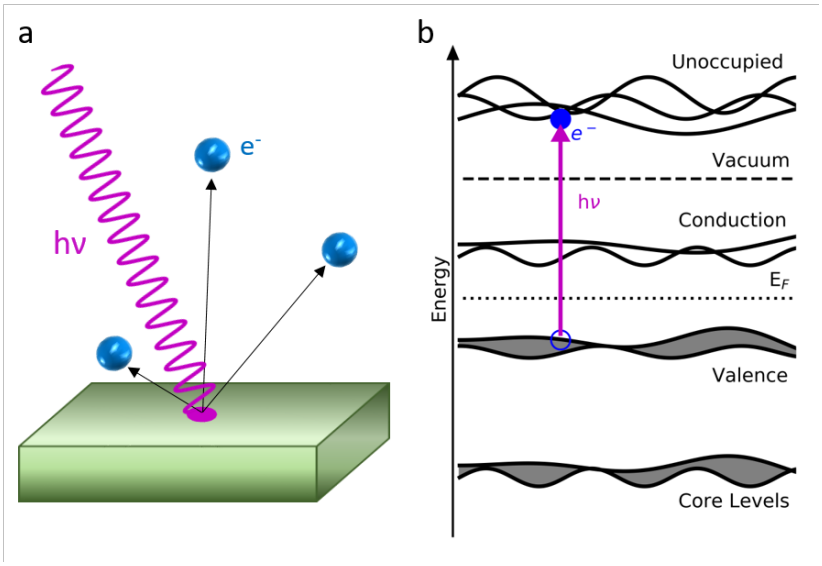

Figure 2.1: General schematic of the photoemission process in a solid. a) UV light (violet wave) with sufficient photon energy ($h\nu$) can remove electrons (blue spheres) from a material through the photoelectric effect. b) Energy diagram corresponding to the photoemission process in a semiconductor material. UV light (violet line) is absorbed by a material, creating an electron and hole pair (filled and hollow blue circles) in discrete states in the conduction, valence, or core levels. Electrons excited into states above the vacuum level (into the "unoccupied" states) can have sufficient kinetic energy to escape the material, as depicted in (a).

function. The photoemission process in solids is commonly described by a three step model, though quantum mechanical treatments (one step model) exist for dealing with strong correlation effects [35]. For this discussion, the three step model is sufficient, and is summarized as follows. First, an electron-hole pair is created through absorption of a photon within the energy levels of a material, as shown schematically in figure 2.1 b. Second, the excited electron travels through the material until it reaches a surface. Third, the excited electron is emitted from the surface, provided it can overcome the material work function.

These three steps include several important practical considerations. In the first step, absorption of a (discrete!) photon must occur. Therefore, the absorption process must both conserve energy and momentum within the material in order to be allowed. This means that the likelihood of absorption of a given photon energy $h\nu$ depends very strongly on the material energy bands, crystal direction, and polarization of light, often referred to by the Fermi Golden Rule. In the second step, events such as electron scattering can change the kinetic energy and momentum of electrons as they travel in the material, leading to the creation of what are known as secondary electrons. This also limits the effective distance which can be traversed before loosing too much energy to overcome the work function, known as the electron inelastic mean free path [36, 37]. This varies with kinetic energy, and can range from less than a nanometer to several tens of nanometers, implying that photoemission is (in many cases) a surface sensitive probe. In the last step, as mentioned before, the electron can only be emitted if it possesses more kinetic energy than the material work function. As schematically shown in figure 2.1 b, this means that it should occupy a state above the vacuum level (which represents the work function) before exiting the material. Thus, and as outlined in equation 2.1, there are constraints based on the photon energy and work function that determine which bound electron states can emit photoelectrons.

After photoemission, the emitted electron's kinetic energy (and angle) can be measured using various schemes. The resulting energy distributions form the basis for many spectroscopic techniques such as ultraviolet photoelectron spectroscopy (UPS), X-ray photoelectron spectroscopy (XPS) and angle-resolved photoemission spectroscopy (ARPES), which are commonly used to characterize the energy states and elemental composition of materials. As a microscopy technique, the goal of PEEM is to then form a real space image of a surface using such photoelectrons.

2.1.2 Photoemission microscopy

In order to image photoelectrons with high spatial resolution, it is necessary to use a system which can effectively collect and magnify them. Modern PEEM instruments achieve this through high numerical aperture immersion objective lenses and electromagnetic lens systems [38–40], similar to those used in other electron-based imaging techniques like scanning electron microscopy (SEM) and transmission electron microscopy (TEM). From here, I will describe PEEM in regards to the SPELEEM system developed and commercially available from Elmitec GmbH, which is the instrument used for this thesis work.

As photoemission is a surface sensitive technique, the sample chamber and imaging column are kept under ultra high vacuum (UHV) for cleanliness of the sample surface

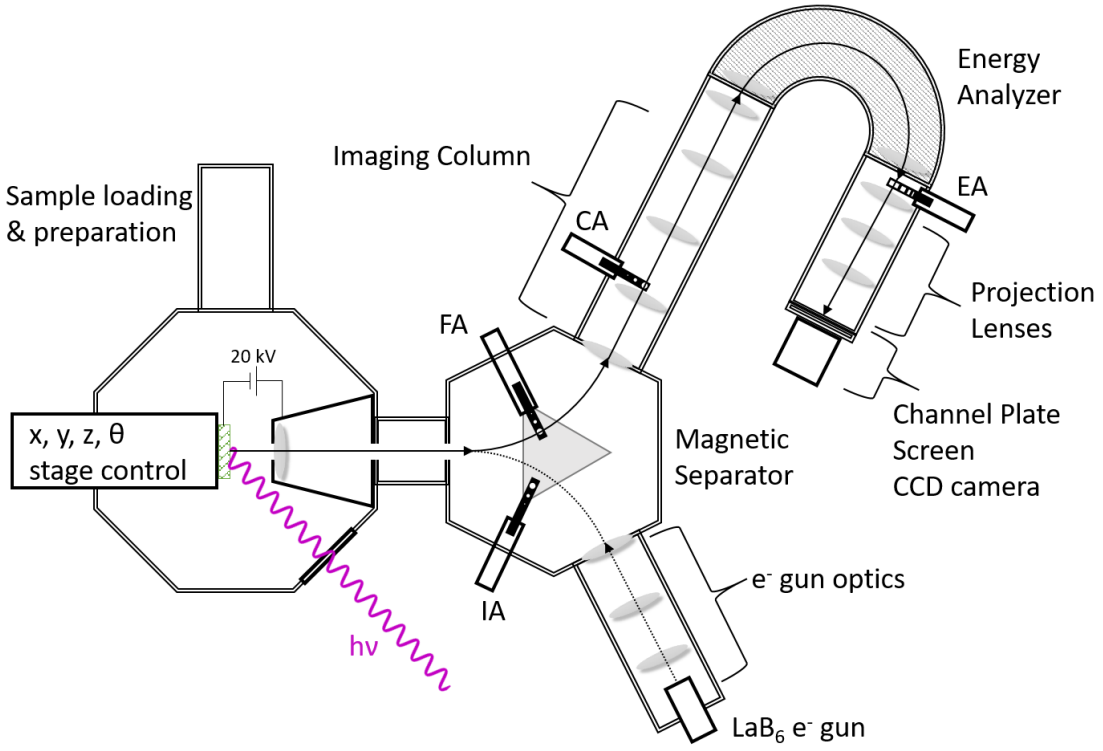

Figure 2.2: General diagram of the major components of the PEEM instrument used (SPELEEM, Elmitec GmbH). Gray ovals represent electromagnetic or electrostatic lens for the electrons emitted by the sample (green hashed rectangle) in the main chamber. The electrons travel along the directions indicated by black arrows. The gray triangle is a magnetic prism, which is needed for separating incoming and outgoing electron beams when using the electron gun for illumination in LEEM mode. IA, FA, CA, EA represent the illumination, field, contrast, and energy apertures which are used for restricting the electron beam in different ways (see discussion in text).

from adsorbed gasses. In addition, high vacuum prevents scattering of the photoelectrons before detection. Typical pressures for the UHV chamber are of the other 10^{-10} Torr or better. Samples are introduced into the measurement chamber through a UHV preparation chamber, as shown in figure 2.2, which can be used for sample heating and sputtering to prepare surfaces, if necessary.

As shown in the left part of figure 2.2, the sample of interest (green hashed rectangle) sits on a xyzθ stage for movement and adjustment of the sample position inside the measurement chamber. Light can be introduced from external sources through view ports on the chamber, impinging the sample at a grazing angle of about 17 degrees. Generated photoelectrons are then collected and accelerated by the immersion objective (tapered cone) which is kept at a potential difference of 20 kV (specifically, the sample is at -20 kV and objective is at ground) several millimeters away. The objective forms the first image of the sample, which is then transferred through the magnetic separator into the imaging column. The magnetic separator is used to separate incoming and outgoing electron beams, which is needed for imaging samples directly with a LaB_6 electron gun when using the instrument as a low energy electron microscope (LEEM). LEEM was not utilized for the results in this thesis, so I will not discuss this operation mode in detail here and instead direct interested readers to Bauer's book on the subject [40].

The image is further magnified in the imaging column by a series of lenses, before being passed to the imaging energy analyzer. The energy analyzer is similar in design to other hemispherical energy analyzers, which disperses the kinetic energy along one axis in order to allow spatial filtering of the signal. The passed electrons are then resolved with an energy resolution related to the geometrical design of the analyzer and the width of the energy slit [41], and are selected by adding a small controlled offset voltage (Start Voltage) to the initial 20 kV accelerating potential. After passing through the analyzer, the image is then projected onto a channel plate stack for signal amplification. The amplified electrons then strike a fluorescent screen which is imaged by a charge coupled device (CCD) camera.

Along the trajectory of the electrons (black lines and arrows in figure 2.2), various apertures are placed at different parts of the beam path, which serve several purposes. The illumination aperture (IA) is used for restricting the beam from the electron gun in LEEM mode, for example to perform micro diffraction measurements. After the objective, the field aperture (FA) is placed in an image plane of the electron beam, which allows for spatial selection of the transmitted image with projected sizes on the final image of about 9, 4, and 1.5 μm in diameter. This aperture is used mainly for doing selected area spectroscopy where the projection lenses image the exit of the energy analyzer, allowing it to act as a multichannel energy detector for rapid acquisition. The next aperture in the imaging column is placed in the back focal plane (diffraction plane) of the field lens (inside the imaging column) and is known as the contrast aperture (CA). This aperture plays an important role in high resolution imaging, as its primary use is to reduce the angular distribution of the transmitted electron beam which in turn reduces the effects of lens aberrations [38, 40]. The projected aperture sizes (in the diffraction plane) are approximately 0.18, 0.57, and 1.84 $Å^{-1}$ in diameter. Lastly, at the exit of the hemispherical energy analyzer is the energy analyzer slit (EA),

as mentioned in the previous paragraph, which acts as a narrow band pass filter for transmitting electrons with a particular kinetic energy. There are five positions on the aperture with different energy windows, from 12 eV (open position, pass energy of the analyzer) to 1.0, 0.5, 0.25, and 0.125 eV in width.

Together, the electron optics and available apertures give the following instrumental resolutions. For ideal imaging conditions (in LEEM with a narrow back scattered beam divergence) and an optimized contrast aperture, the resolution limit is approximately 8 nanometers [39, 41]. For PEEM, the ultimate resolution is usually worse (due to the larger divergence of the photoelectron beam) and is typically found experimentally to be in the range of 10-50 nm. In both cases, the ultimate resolution will depend strongly on the surface morphology (i.e. the roughness) and the energy of the emitted electrons (higher kinetic energies can achieve better resolution). For spectroscopic measurements, in an ideal case where the smallest energy slit can be used and with a low rate of photoelectrons (to minimize space charge effects, discussed more in section 2.3), an energy resolution close to 100 meV could be achieved, though in most practical experiments the resolution will be closer to 150-200 meV [41]. In most cases the overal energy resolution of the instrument will then not be limited by the bandwidth of the photon source, though it should be considered when using broadband sources such as ultrashort light pulses.

With the stated instrument resolutions above, the last point to consider are some of the mechanisms which give contrast to images in PEEM [39, 41, 42]. Following the simple relation introduced in equation 2.1, there are different scenarios which can occur. First, and most commonly used with low photon energy sources, is contrast due to work function differences. For a given photon energy, two materials with a different work function will have an effective difference in the number of generated photoelectrons. Assuming no other changes in the density of bound states, a material with a smaller work function would appear brighter in PEEM, due to the larger range of bound states which could be photoemitted from. This can also be observed through spectroscopic measurements, where the secondary electron cutoff (at low kinetic energies), referenced correctly to the Fermi level (zero binding energy), will be shifted to deeper (shallower) binding energy for smaller (larger) work function materials. Another main contrast mechanism is due to differences in the bound states of the electrons. In this case, it is more useful to consider energy-resolved measurements, where the density of states within a particular energy range can be measured, for example at the valence band (VB) edge or an elemental core level. Either shifts in binding energy or differences in the density of states would then lead to contrast differences while imaging. Other contrast mechanisms include magnetic dichroism to polarized light, differences in momentum distributions, and local field enhancement effects, however the two simple process described above are sufficient for interpreting the data presented later in chapter 3.

Together, these capabilities have made PEEM instruments a powerful tool to study microscale or smaller variations in chemical composition and phase changes [41–43]. In particular, many PEEM instruments are located at synchrotron light sources, where they can make ready use of the bright, tunable, and monochromatic UV and X-ray photons generated. On the other hand, the development of high power laboratory based light sources, for example using pulsed lasers, has also seen significant development in

the last few decades. These sources offer new opportunities for novel measurements, in particular for time resolved measurements, which I will introduce in the next section.

2.2 Time-resolved photoemission electron microscopy

Following the description of PEEM imaging, there are several interesting characteristics which lead towards the extension into time-resolved PEEM (TR-PEEM). First, PEEM images directly the density of occupied electron states in a surface. Second, there is a very flexible choice in external light sources which can be used, with the only real condition being that in the end, a sufficient number of useful photoelectrons must be emitted. Third, is that the imaging is "full-field", or rather, not scanning based. This means that relatively rapid image acquisition can occur, provided the photoelectron yield is high. With these ideas in mind, the concept behind a TR-PEEM approach is to first transiently populate a higher energy state, then measure the occupation of that state and its relaxation in time. PEEM provides a way to image the occupied states, while excitation can be achieved through, for example, a pulsed optical laser. A common way to achieve time resolution in this case is to use a two pulse method, often called pump-probe in traditional optics, where one pulse is used to excite the material (pump) and a second, weaker time delayed pulse (probe) is used to observe a transient change. The same idea can be applied to PEEM (and photoemission in general), as illustrated in figure 2.3, where a higher energy state, such as the conduction band (CB), is transiently populated by a pump pulse. Subsequent probe pulses with a controlled time delay (dt) are then used to photoemit electrons from this transient state, before they relax. The relaxation of carriers from the transient population can then be visualized by changing the time delay between the pulses and recording the changes in photoemission intensity for each time delay.

For studying electronic relaxation processes, the relevant time scales are from femtoseconds (fs) to picoseconds (ps) or nanoseconds (ns) [44]. Modern commercial ultrafast lasers can readily deliver pulses with durations down to a few tens of fs. The more pressing issue for photoemission, as described before, is the need for photon energies of the order 3-6 eV or larger to overcome the material work function. Common ultrafast lasers such as titanium sapphire based lasers emit at about 800 nm (1.55 eV), which is too low of photon energy in most cases (though for very high pulse energies or due to local field enhancement, nonlinear multiphoton processes can occur [45–47]). There are, however, solutions to this through utilizing nonlinear optics. One straightforward way is to generate harmonics of the laser fundamental through nonlinear processes in crystals such as beta barium borate (BBO). Due to the phase matching conditions and UV absorption in such crystals [48], wavelengths much shorter than about 200 nm (6.2 eV) become difficult to generate this way, however this energy is already sufficient for performing photoemission from states near the Fermi level, such as the conduction band and valence band edge near the Brillouin zone center. In addition, there are schemes to efficiently generate the third (266 nm, 4.65 eV) and fourth (200 nm, 6.2 eV) harmonics from titanium sapphire based (800 nm, 1.55 eV) lasers, even for oscillator lasers with lower pulse energy and high repetition rate [49], the importance of which in PEEM imaging will be discussed more in section 2.3.

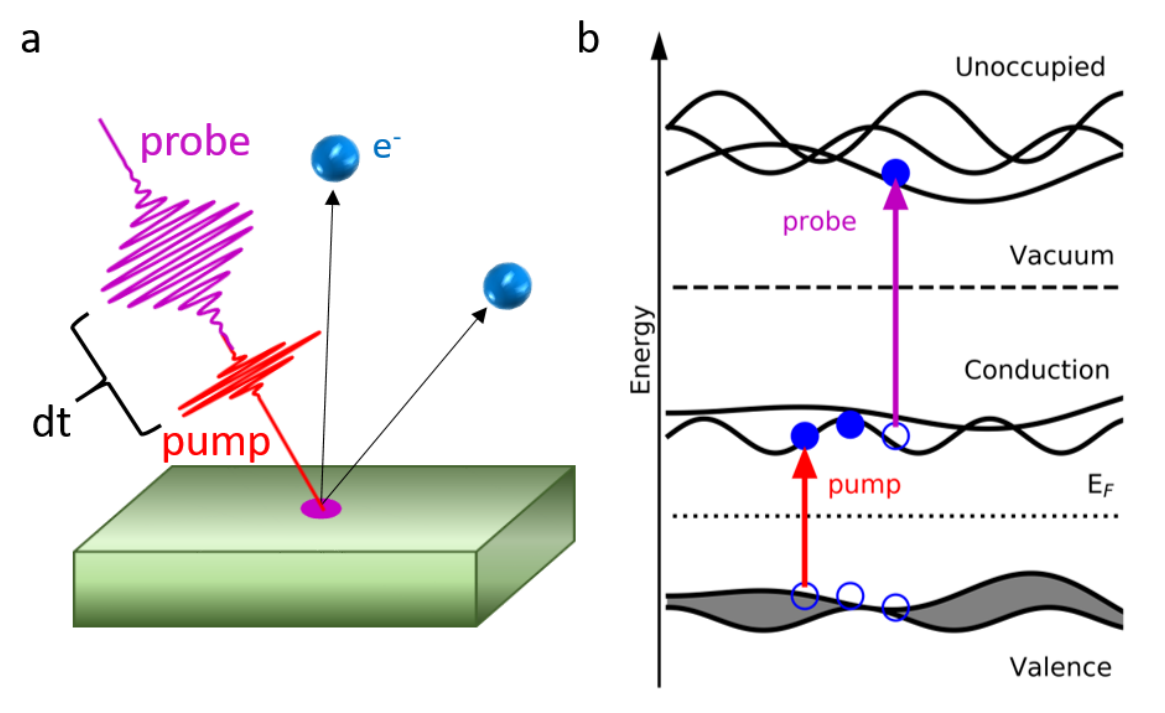

Figure 2.3: Schematic of time-resolved photoemission from a solid. a) Pump (red) and probe (violet) pulses strike a sample with a controlled time delay (dt). The pump excites the sample, while the probe photoemits transiently excited electrons (blue spheres). b) energy diagram of the process in (a), where a pump pulse (red arrow) excites electrons and holes (filled and hollow blue circles) into the conduction and valence bands. The subsequent probe pulse then photoemits electrons which are transiently in the conduction band.

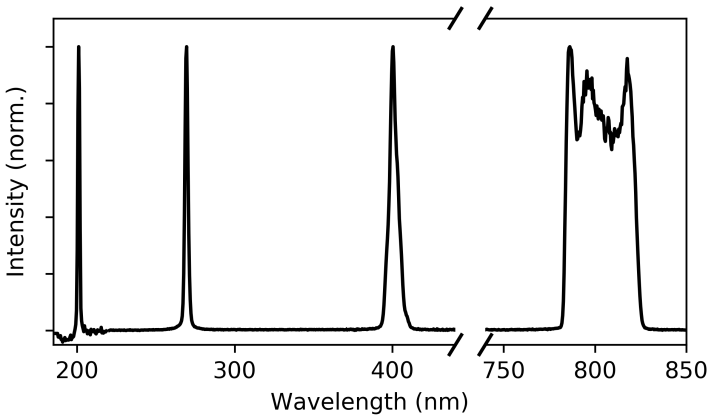

Figure 2.4: Spectrum of the laser fundamental centered at 800 nm, as well as the generated second (400 nm), third (266 nm), and fourth (200 nm) harmonics.

While I will not go into the full details of the setup used here for generating the third and fourth harmonics of our laser (see [49] for the general design reference), I will outline some of the main characteristics it provides. The starting laser is a long cavity oscillator system (Femtolasers XL650) delivering 45 fs pulses with a 4 MHz repetition rate, centered at 800 nm and with a pulse energy of 650 nJ. The generation setup, using an input intensity of about 500 mW (135 nJ) can produce simultaneously the third (266 nm, 4.65 eV) and fourth (200 nm, 6.2 eV) harmonics with typical intensities of about 5 mW and 500 μW, respectively. The spectrum of the harmonics, including the second harmonic and the laser fundamental, are shown in figure 2.4. In terms of photons, these intensities correspond to the order of around 10^8 photons/pulse (or 10^{14} photons/s at 4 MHz) for the UV probe pulses. There are some limitations with utilizing this high photon flux in photoemission, however, which I will discuss further in section 2.3. Nevertheless, this provides us with a bright laboratory source of UV photons for use in PEEM and TR-PEEM measurements.

To actually perform a time resolved measurement with fs resolution, as introduced above, a two-pulse scheme is usually needed. Here, I will describe the experimental setup used to achieve this with our system, as shown schematically in figure 2.5. From the laser output, the pulses are first sent to a pulse compressor, where the dispersion of the ultrafast pulses is compensated for in order to maintain a short pulse duration inside the harmonic generation setup. After the compressor, the beam is split into two paths. One path (probe) is sent to the harmonic generation setup to produce the third and fourth harmonics, which are then directed into the PEEM measurement chamber. The window on the chamber is made of fused silica in order to prevent absorption of the UV pulses. The other path (pump) is sent to a mechanical delay stage, before entering the measurement chamber, which is used to control the relative arrival time of the pump and probe pulses at the sample with micrometer precision. While figure 2.5 is not to scale, the two path lengths in the experiment must be precisely set in order to achieve overlap of the pulses in time. For reference, in 1 ns light travels a distance of 300 mm (in air), meaning that the two paths must be set to a precision better than 30 μm

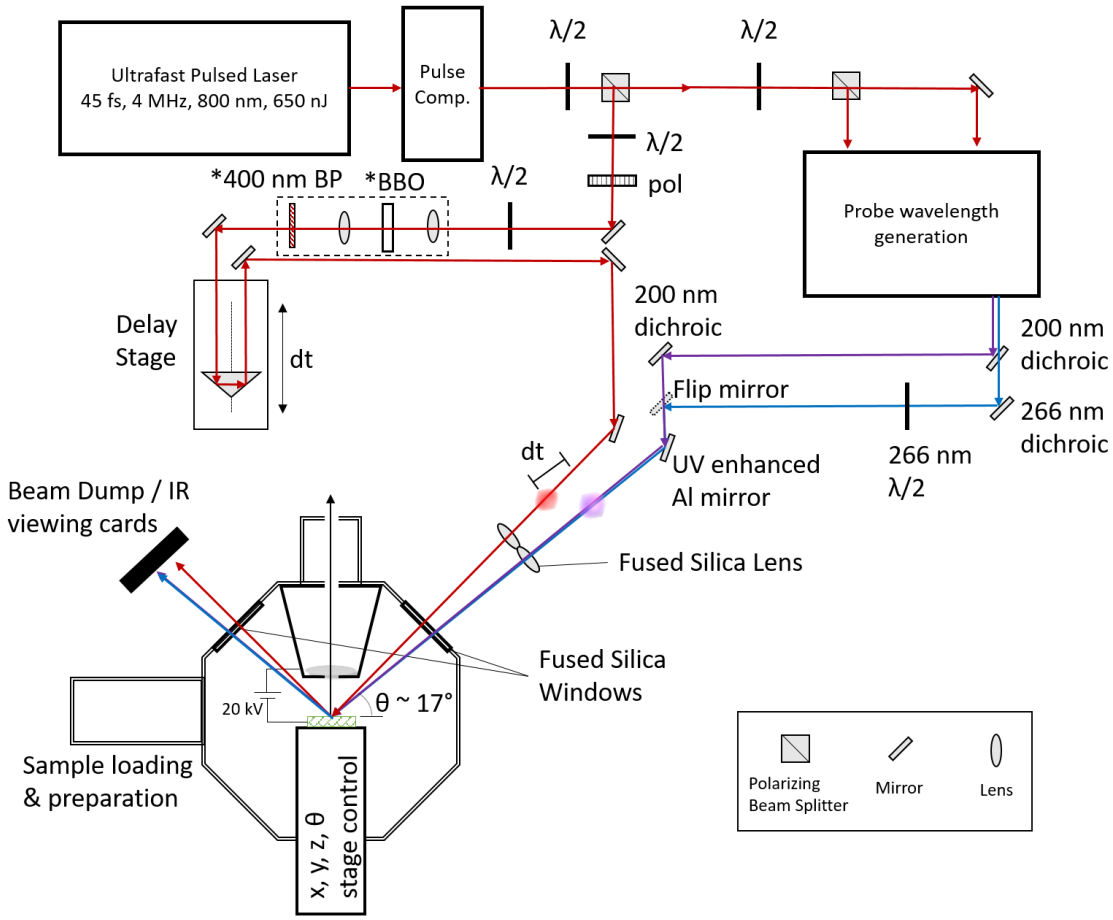

Figure 2.5: Schematic of the TR-PEEM optical setup used (not to scale). The output of a long cavity titanium sapphire oscillator (Femtolasers XL650) is sent to an external pulse compressor (Swamp Optics BOA-8), before being split into pump and probe paths at a polarized beam splitter, where half wave plates ($\lambda/2$) are used to change the ratio of power sent to each path through the beam splitter. The pump is sent (*through an optional BBO and band pass (BP) filter for second harmonic generation, dashed box) to a mechanical delay stage before being sent into the PEEM measurement chamber. The probe path goes to a home-built third and fourth harmonic generation stage. The desired harmonic is selected with dichroic mirrors for specific wavelengths and movable flipping mirrors before being sent into the PEEM chamber. The measurement chamber has a thin fused silica window in order to prevent absorption of the UV probes. The pump and probe beams hit the sample at a grazing angle of about 17 degrees, and a second window on the opposite side of the chamber allows for viewing any reflected laser light on appropriate IR or UV viewing cards.

with the delay stage in order to overlap two 100 fs pulses. For specific measurements, the pump photon energy can also be doubled to 3.1 eV (400 nm) through addition of a BBO crystal and band pass filter into the pump path, allowing for excitation of wider band gap materials. Based on the incident angle and distance between the chamber window and sample, the smallest beam size typically achieved (using 1 inch diameter optics with a 250 mm focal length lens) is about 70 μm by 235 μm full width half max (FWHM) of the short and long axis of the elliptical spot, respectively. For these experiments, we use this size for the pump beam, which with the available laser power, allows for excitation fluences ranging from a few 10s of nJ/cm^2 to around 1 mJ/cm^2 per pulse. For the probe, the beam size is sometimes increased to provide more uniform imaging over large areas, however there are also benefits to using a more focused beam for high magnification imaging, which can help to reduce space charge, as discussed in section 2.3.1. The overall temporal resolution of our setup, limited by the temporal width of the pump and probe pulses, is around 300 fs at the sample, likely due to dispersion which broadens the probe pulse in the generation setup.

Historically, following the necessary development of modern ultrafast laser sources and PEEM technology, TR-PEEM as a field has only emerged within roughly the last two decades. Some of the earliest successes with the technique were in studying metallic nanostructures and coupling with surface plasmon polaritons, work which still continues today [46, 47, 50–59]. A key feature of the success in this area is to use the local field enhancement due to the metallic structures to greatly enhance the probability of multiphoton absorption processes. This in turn allows TR-PEEM to map out the local electric field and how light couples to the surface plasmon modes in such structures, making TR-PEEM a powerful tool to study the nanoscale response of plasmonic nanostructures.

Only more recently, however, has TR-PEEM been applied to study semiconducting materials. Fukumoto, et al. have used TR-PEEM to study the free carrier response in gallium arsenide (GaAs) and demonstrated the ability to observe drift of carriers in an applied field [60, 61]. They have also shown that recombination kinetics at nanoscale defect sites in GaAs can be studied and quantified with this technique [62]. More recently, they have studied the photocarrier lifetimes in twisted multilayer graphene heterostructures [63]. Another group, at Nanyang Technological University Singapore, has also recently applied TR-PEEM to study the heterogeneous carrier dynamics in monolayer WSe_2 flakes [64]. Previous work done in our group, led by M. K. L. Man, used TR-PEEM to study the transfer of charges in an indium selenide (InSe) heterostructure with GaAs, where we observed different rates of transfer into different thicknesses (with different band gaps) of InSe [65]. Recently, work in our group led by E. L. Wong studied the effects of bulk to surface carrier transport in doped GaAs due to the surface band bending, and further demonstrated how the resulting vertical and lateral currents can be optically controlled [66]. These few works studying semiconductors with TR-PEEM represent the pioneering work and current state of the art for the technique.

2.3 Considerations for TR-PEEM

In this section, as alluded to previously in section 2.2, there are some limitations and considerations which need to be discussed for performing time resolved photoemission experiments. Here, I will focus on three main challenges. First, I will discuss the issue of space charge in PEEM. Second, I will discuss about the noise in our laser setup. Lastly, I will talk about some of the ideas and challenges with TR-PEEM signal interpretation.

2.3.1 Space Charge

One of the most significant challenges to overcome is the effect of space charge in the PEEM system. Space charge results when multiple photoemitted electrons are closely grouped, such that they interact, effectively randomizing their trajectories and kinetic energies [67]. For photoemission measurements and microscopy, this can result in a severe loss of both spatial information and kinetic energy information, thus it is of utmost importance to minimize its effect. For time resolved measurements specifically, this represents a major issue in terms of selecting a suitable photon source. The issue comes from the fact that for a time resolved measurement, using short pulses of light, the photoelectrons emitted by a sample by a single pulse will be grouped very closely in time. This can lead to very severe space charge effects, especially for measurements using high pulse energy [68]. The way to overcome this problem is to reduce the energy per pulse down to a level where on average, less than one photoelectron per pulse is generated. At this limit, assuming a (relatively low) cross section of photoemission of about 10^{-6} e^-/photon, this gives a rough limit of 10^6 photons/pulse [69, 70]. Compared to the available 10^8 photons/pulse our laser system can deliver for the fourth harmonic, it is immediately evident that we cannot expect to use anything more than a small fraction of the generated power for staying below the space charge limit. Indeed, in both imaging (figure 2.6) and spectroscopic (figure 2.7) measurements with the third and fourth harmonic probes, respectively, we can easily reach the regime where space charge deteriorates the information quality.

This limit on the pulse energy then places a limit on the number of photoelectrons which can be generated over a given time frame. Therefore, to increase the total number of measured events, a laser with a higher repetition rate must be used. This of course brings in further considerations. First and foremost, is that the lifetime of the excited carriers should be shorter compared to the pulse separation time. If the lifetime is longer, there is a possibility of artifacts in the measured signal, such as an offset or altered dynamics, due to the background of excited carriers in the system. Therefore, ideally, the pulse separation should be longer than the carrier lifetime, meaning that the laser will have a lower repetition rate. For example, a 1 MHz pulsed laser has a pulse separation of 1 μs, while a 1 kHz laser has a 1 ms pulse separation. This works to contradict the need for a higher rate of counting statistics; therefore, the signal intensity achievable without space charge must be balanced against the carrier lifetime in order to optimize measurements. Unfortunately, titanium sapphire based lasers often do not have much (if any) tunability in repetition rate, though new fiber amplifier lasers which have emerged on the market in the last few years may soon make this less of an

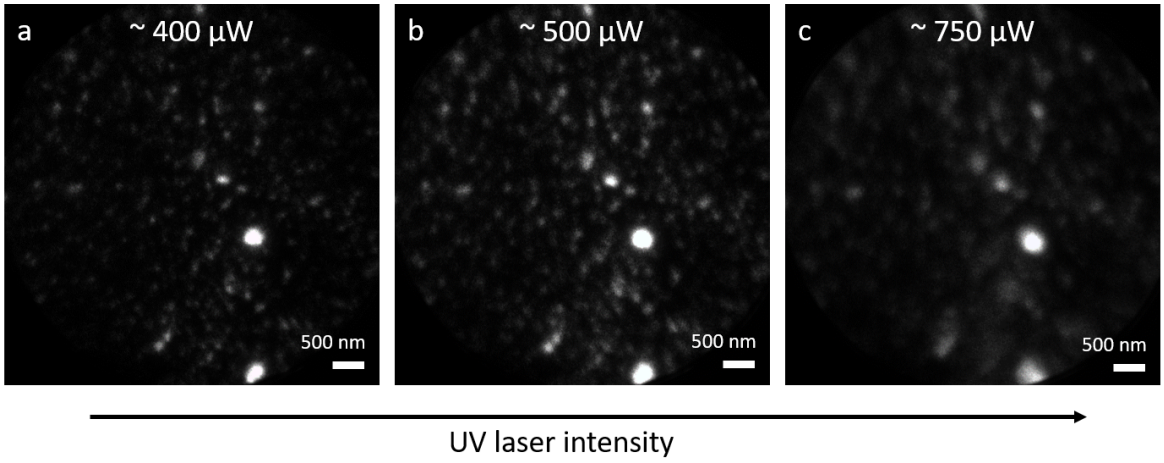

Figure 2.6: PEEM images of a perovskite sample using the third harmonic probe (4.65 eV, 266 nm). At higher probe intensity, space charge effects cause image features to blur and broaden.

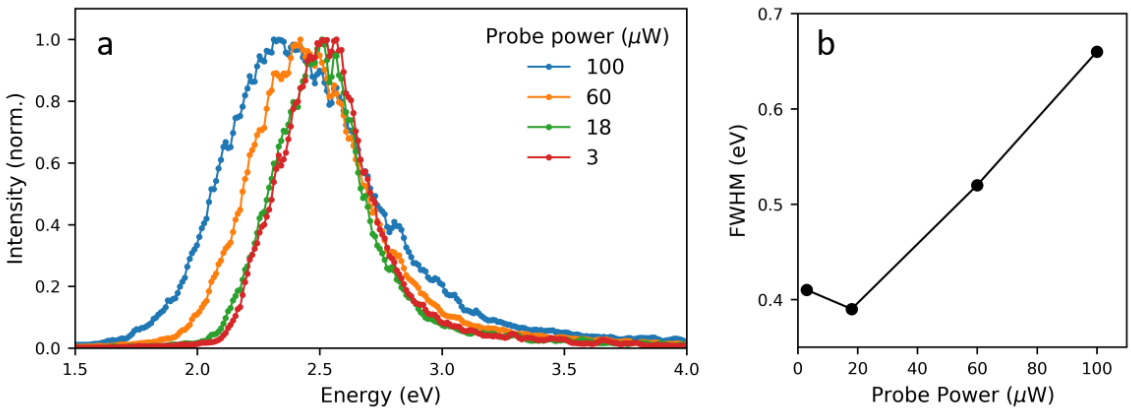

Figure 2.7: Photoemission spectra of a perovskite sample at different fourth harmonic (6.2 eV, 200 nm) probe intensities. a) normalized photoemission spectrum, where broadening in energy due to space charge can be observed at higher powers. b) The corresponding full width at half max (FWHM) of the spectra in (a).

issue. For our experiments, we have chosen to use a laser with a 4 MHz repetition rate, as described in section 2.2, which results in a pulse separation of 250 ns. For many semiconductors, this is reasonable to not cause problems with the carrier lifetime, and still allows for imaging at a fairly quick rate. As a rough estimate, we find that given the condition of about one electron produced per pulse, at high magnification (close to instrument resolution limit) we can often image with exposure times on the order of a few seconds (without any imaging apertures). This also matches with the order of the pixel size of the camera (roughly 1 megapixel), meaning that we have at least about one event per pixel in order to fill the image intensity.

A second limitation resulting from space charge, as a more general discussion, is that a lower pulse energy (from a high repetition rate laser) will limit the accessible optical nonlinearities, specifically the nonlinear processes used to generate either the UV probe or the pump pulses. While oscillator lasers can have sufficient pulse energies for producing the 3rd and 4th harmonics of the fundamental [49], as mentioned previously, these lasers do not normally allow for the use of optical parametric amplifiers, which are used to continuously tune the photon wavelength in the visible and near-infrared range in high pulse energy, low repetition rate systems. This limits oscillator lasers to excitation with either the fundamental wavelength or a harmonic of it, meaning that resonant pumping of carriers can only be achieved through design and choice of the sample. Hence for the studies here, as mentioned before, we can only excite materials with either the 1.55 eV fundamental or the 3.1 eV second harmonic. Considering again the probe, I would just like to mention that for systems with high pulse energies, other nonlinear methods for generating UV light are possible. The most widespread method under development is higher harmonic generation in gasses, which can produce photon energies of several tens of eV, and potentially into the soft X-ray regime [71]. I mention this as a future outlook for TR-PEEM, as with the recent advent of high repetition rate, high pulse energy fiber amplifier lasers, the ability to use such nonlinear processes for both pump and probe generation in practical imaging experiments should become much more realistic in the near future, if not already possible.

2.3.2 Laser Noise

Another important consideration for TR-PEEM measurements is the stability and noise level of the laser system. This is crucial information for designing any experimental plan. Here, I show some basic characterization of the laser setup described earlier in section 2.2. I will first discuss the intensity stability of the laser and the generated fourth harmonic, shortly after aligning the setup, over a period of several hours as shown in figure 2.8 a and b, respectively. While there is a slow variation in the fundamental intensity, there are sharper changes in the fourth harmonic. This is due to the nonlinear dependence on the intensity and pulse duration, which amplifies the small variations in the fundamental. Looking at a time range where the system has stabilized more, (figure 2.8 c, d), I find that the standard deviation of the fundamental intensity is about 0.07%, which agrees with the laser specification. As expected, the variation is larger in the fourth harmonic intensity, with a standard deviation around 0.73%. Based on this, I expect that TR-PEEM measurements with this system could achieve a sensitivity (percent change in the signal) of around 1% or a little better (particularly for the third

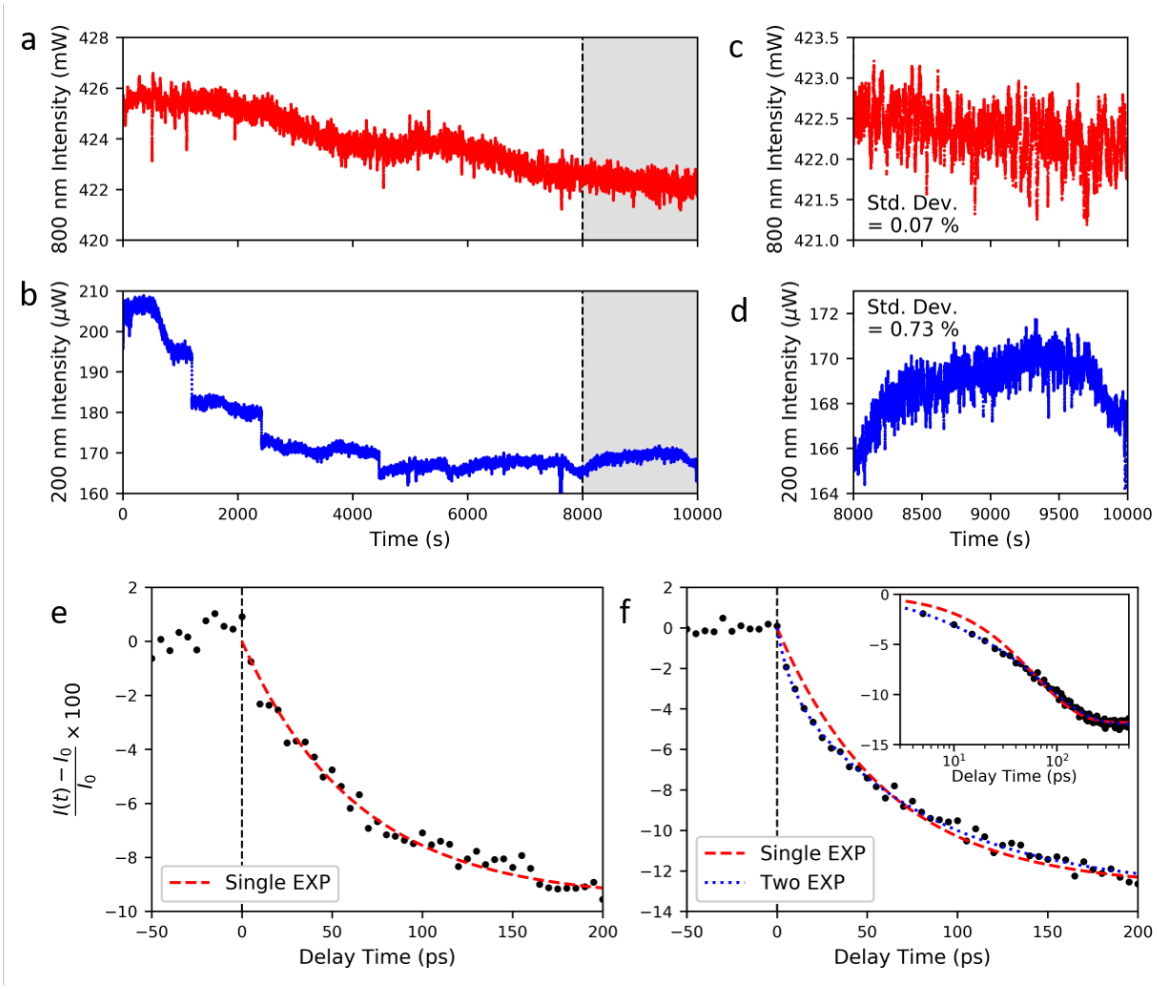

Figure 2.8: Evaluation of laser stability and noise over time. a) Intensity variation of part of the laser fundamental over several hours. b) Intensity of the generated fourth harmonic over the same time frame as (a). c, d) Zoom-ins of the shaded regions in (a) and (b), with the corresponding standard deviations for this time section of 0.07% and 0.73% for the fundamental and fourth harmonic (200 nm, 6.2 eV), respectively. e) Representative TR-PEEM signal for a perovskite sample, plotted as the percent change of the signal $I(t)$, relative to the signal without photoexcitation I_0 at negative time delay, and fit with a single exponential decay (red dashed curve). f) the same data as in (e), but with noise correction by normalization to a reference signal in the PEEM image. In this case, a biexponential fit (blue dotted curve) represents the data better than a single exponential (red curve). The inset shows the data on a log scale in delay time, to better emphasize the fitting differences at short time delays.

harmonic probe). From my measurements on perovskite materials, I find this estimate agrees fairly well. For the representative TR-PEEM curve shown in figure 2.8 e (the measurement details to be discussed in chapter 5), I find that the standard deviation of the background signal (at negative time delay) is about 0.50% for the third harmonic probe.

While multiple scans and longer averaging are the usual ways to push to better signal to noise, the wide field imaging achieved in PEEM offers a clever method to reduce the laser noise for TR-PEEM measurements. As mentioned previously in section 1.3, on our perovskite samples we used gold markers as position references (as seen in figure 1.4). Under our experimental conditions, these markers do not show a transient TR-PEEM signal, which allows us to use the photoemission intensity of the marker as an internal reference of the probe intensity (versus externally measuring the power throughout the experiment, for example). Therefore, we can normalize the signal from the sample of interest by the intensity of the gold marker located in the same image in order to reduce intensity fluctuations due to the probe. This is shown in figure 2.8 f, which is the same data set shown in figure 2.8 e, but normalized to the intensity of the gold marker in the image. This reduces the standard deviation of the background signal to around 0.28%, almost a factor of two better. The importance of improved signal to noise also becomes apparent from this measurement. In the uncorrected case a single exponential fit can reproduce the measured decay, whereas after noise correction it no longer provides as satisfactory of a fit, particularly at short time delays. Therefore, unless stated otherwise, all the TR-PEEM intensity traces presented for perovskite samples in the rest of this thesis will use this correction to further improve the signal to noise. Thus, in order to achieve very high signal to noise in TR-PEEM measurements, care should be taken to account for the intensity fluctuations of the laser, which will be amplified greatly by the non-linear processes used for UV probe generation.

2.3.3 Signal Interpretation

As a final consideration for TR-PEEM, it is useful to discuss a relatively simple example of how the changes in photoemission intensity can be understood in a measurement. For this example, I show TR-PEEM measurements of a p-type GaAs wafer which was cleaved in-situ to expose a fresh (110) surface. Here, we excite the sample with a fluence of about 40 μJ/cm^2/pulse of 1.55 eV photons, and measure the resulting percent change in photoemission intensity with the third (blue circles) and fourth (violet triangles) harmonic probes, as shown in figure 2.9 a. For the third harmonic probe (4.65 eV), there is a sharp increase in the photoemission intensity at zero time delay, followed by a slow recovery on a ns time scale. For the fourth harmonic probe (6.2 eV), we instead see a sharp decrease in the photoemission intensity, with a similar overall time scale.

This difference in signal is due primarily to the different states that the probes couple to, as outlined in figure 2.9 b. For the third harmonic, the photoemission intensity without the pump is very low, due to the GaAs work function being larger than the photon energy. Upon photoexcitation, a large number of electrons are promoted to the conduction band, from where the probe now has sufficient energy to excite them above the vacuum level and cause photoemission. Hence, there is a very large transient increase in the measured population. For the fourth harmonic, the probe possesses

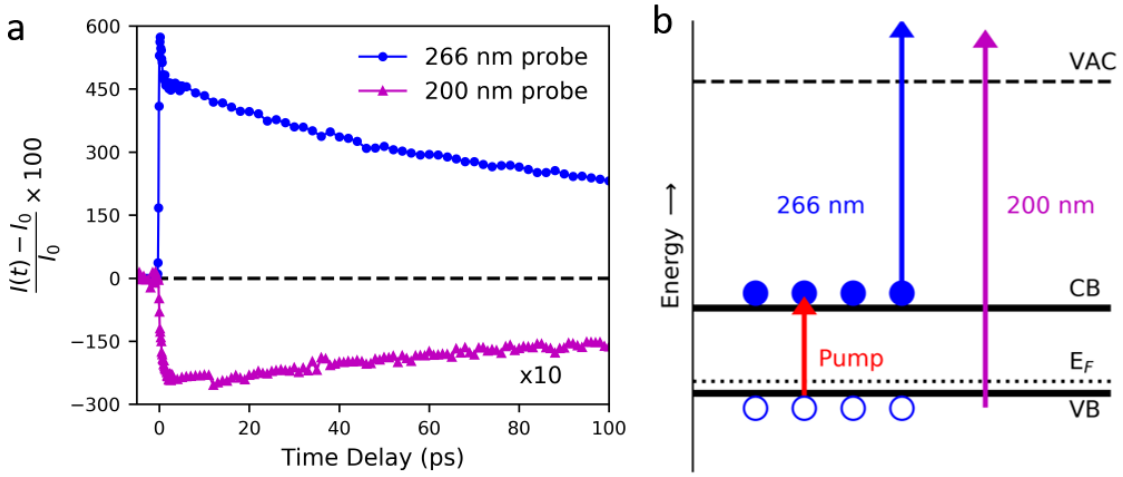

Figure 2.9: Representative TR-PEEM signal of a GaAs test sample. a) TR-PEEM signals measured from a cleaved p-type GaAs wafer after excitation with 1.55 eV pulses with a fluence of about 40 μJ/cm^2/pulse, using the third (4.65 eV, blue dots) and fourth (6.2 eV, violet triangles) harmonic probes. The signals ($I(t)$) are plotted as a percent change, relative to the signal at negative time delay (I_0). The signal for the 6.2 eV probe is multiplied by a factor of 10 for better visual comparison. b) Schematic of the dynamics measured in (a). The pump (red arrow) excites free electrons and holes (filled and hollow blue circles) into the conduction (CB) and valence (VB) bands, respectively. The 266 nm (4.65 eV) probe has less energy than the work function (difference between vacuum (VAC) and Fermi level (E_F)), and thus only photoemits electrons which are transiently excited into the conduction band. The 200 nm (6.2 eV) probe instead has sufficient energy to directly photoemit electrons from the valence band.

enough energy to photoemit electrons directly from the valence band. Hence, upon excitation, there is a sudden decrease (increase) in the number of electrons (holes) at the valence band edge, leading to a decrease in the measured photoemission intensity. In this case, the 6.2 eV photons either do not couple as strongly between the conduction band and states above the vacuum level, or the number of excited electrons is far too small to resolve against the large density of states in the valence band. As a comparison, time resolved ARPES measurements under similar experimental conditions observed that the population of conduction band electrons is of the order 10^{-5} smaller than the valence band electrons [72], which is below our estimated sensitivity limit. Therefore, the excited electrons in the conduction band do not contribute much to the total integrated signal of the fourth harmonic in this case. Note that because of the difference in photoemission background (i.e. without pump), the third harmonic probe fluence can be more than 100x higher before having space charge issues for this measurement, which further amplifies the differences in signal observed. Therefore, when interpreting a TR-PEEM signal, it is always necessary to consider and understand what states are more strongly probed in the measurement.

2.4 PEEM Discussion

Thus, in this chapter I have explained in detail the ideas behind using PEEM and TR-PEEM to study materials. PEEM provides a powerful tool for imaging the electronic structure of surfaces with nanometer scale resolution. Due to the flexibility of light sources which can be used for PEEM, it follows as a rather natural extension to develop time-resolved techniques using ultrafast pulsed lasers. The relatively new method of TR-PEEM provides a novel way to image the dynamics of photoexcited carriers in materials, while simultaneously achieving spatial resolution below the optical diffraction limit. While there are challenges with using this technique, our group has worked to develop it and apply it for studying semiconductor materials. Following this introduction, I will next start to discuss in chapters 3 and 4 the first results obtained on HOIP materials through using PEEM to image the steady-state properties of traps, while later in chapter 5 I will delve into the results of TR-PEEM experiments. Chapters 6 and 7 will then focus on other interesting studies which can be realized through PEEM imaging on HOIP materials.

Chapter 3

Photoemission microscopy and spectroscopy of HOIP

In this chapter, I will present the first main results of my study of HOIP thin films using PEEM. Here, I discuss the heterogeneous surface features observed in PEEM in section 3.1, then discuss their identification as trap sites through photoemission spectroscopy (PES) in section 3.2. In section 3.3 I will discuss the results from the first two sections in relation to previous work in the literature, and discuss possible origins of the traps.

3.1 PEEM imaging of heterogeneity

As first introduced in section 1.2, a major goal of this research was to try and identify the nanoscale origins behind the observed non-radiative carrier losses in perovskite thin films. Thus, I first begin here by using PEEM imaging to study the surface heterogeneity in the three different triple cation samples studied: the iodine-only (I-only), bromine and iodine mixed halide (I-Br), and potassium passivated mixed halide (K-pass). In this section, I focus on information obtained with the third harmonic probe photons (4.65 eV). Incident probe pulses were of fluences on the order of 100 nJ/cm^2/pulse, where the fluence is set by balancing space charge effects to the image intensity, as discussed in section 2.3.1. Image exposure times were typically one to a few seconds, with several tens of averages to smooth out image noise. Irregularities in the channel plate amplification, phosphorescent screen, and CCD camera are corrected for by normalizing images with a flat field procedure.

Looking at a representative I-Br sample in PEEM, at lower magnifications the deposited gold position markers are generally easy to identify, as seen by the hexagons and triangles in figure 3.1 a. Upon going to higher magnifications, as shown in figures 3.1 b and c, the small features on the perovskite sample become resolvable. In particular, for fields of view (FOV) of about 10 μm or smaller (figure 3.1 c), we can identify a distribution of small bright spots with PEEM. This observation is not limited to this sample alone; similar distributions are observed on all three sample types investigated.

A representative high magnification PEEM image is shown for I-only, I-Br, and K-pass samples in figure 3.1 d, e, and f respectively. Here, for comparison, the images are normalized by laser power and camera exposure time, then displayed on a normalized

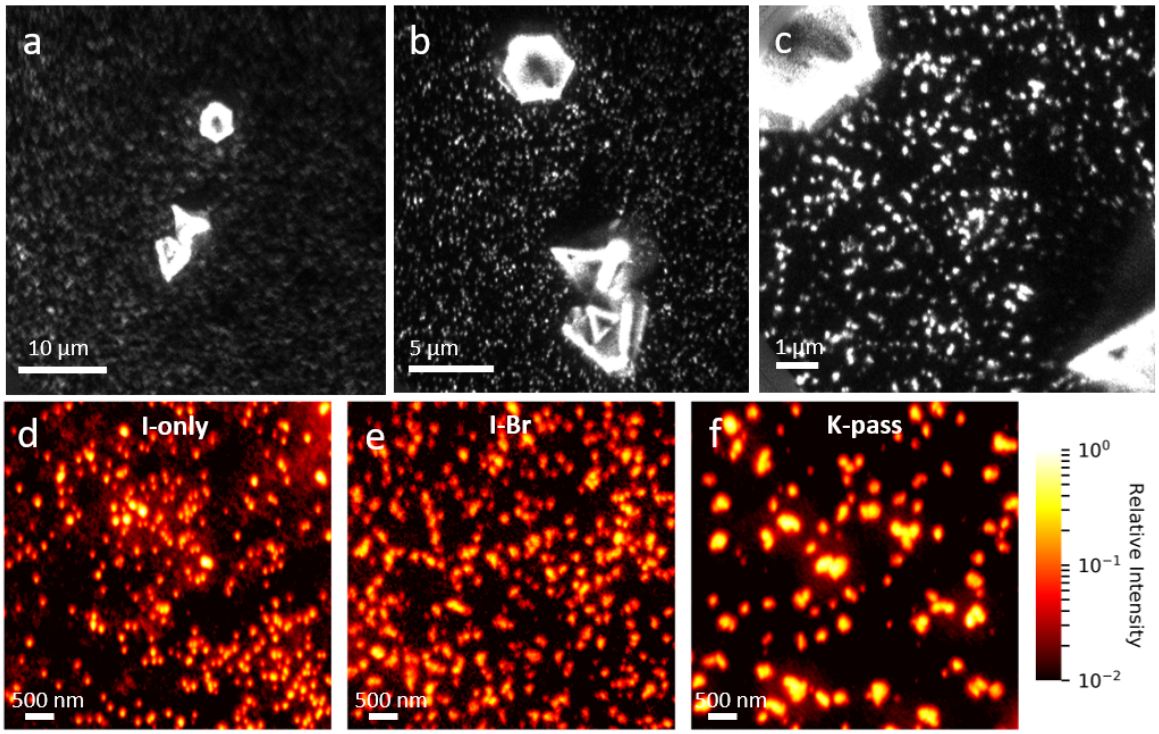

Figure 3.1: PEEM images using the third harmonic (4.65 eV) probe of HOIP samples. a-c) Images of an I-Br sample at different magnifications. The bright triangular and hexagonal shapes are deposited gold markers which are used for position references. d, e, f) Images of an Iodine-only, I-Br, and K-passivated sample, respectively. The images are scaled by laser power and camera exposure time, then normalized for comparison of intensity. Note that the image intensity for d, e, f is on a logarithmic scale.

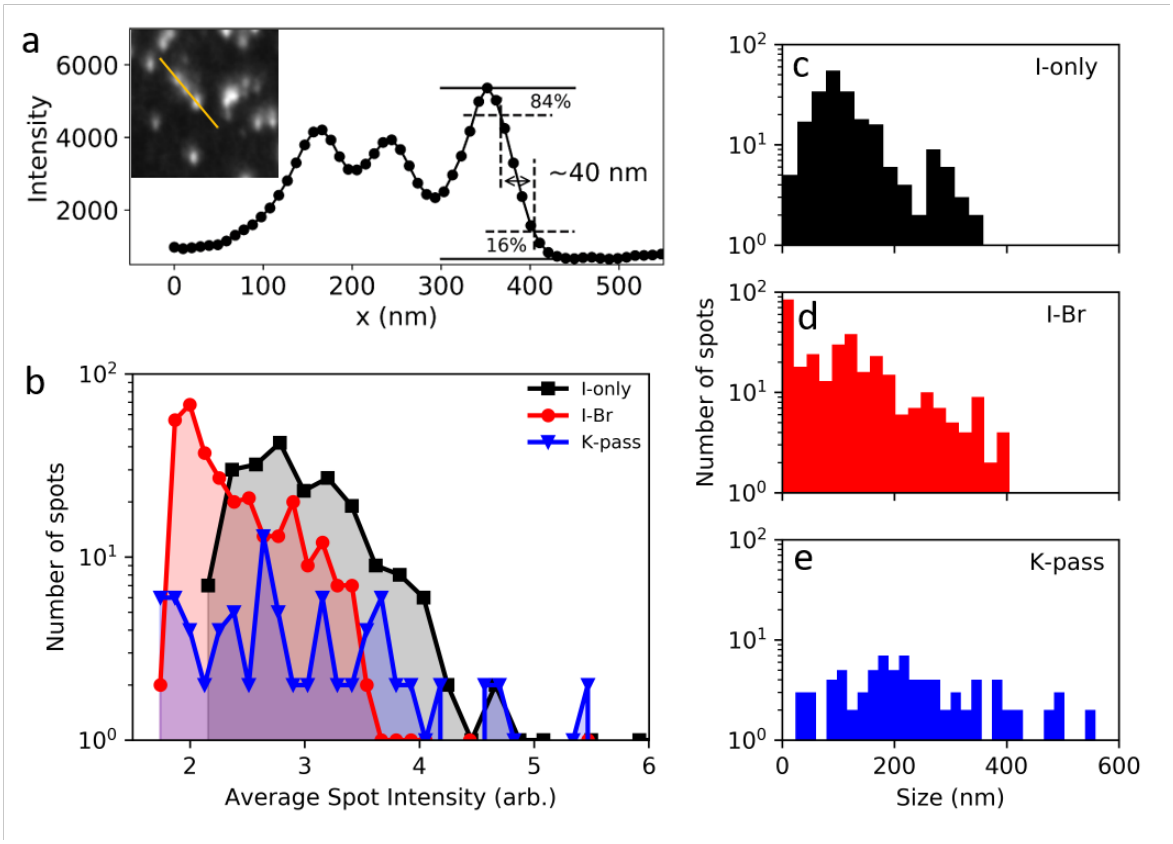

Figure 3.2: Size and intensity statistics of spots observed in PEEM with the 4.65 eV probe. a) Intensity line profile for an I-only sample (inset), which is used to estimate the image resolution of 40 nm from a 84-16% criterion. b) Intensity histogram of the bright spots shown in figure 3.1 d-f. c, d, e) Size histograms of the same PEEM spots.

logarithmic color scale. All three samples show small spots in PEEM, however the first obvious difference between them is the number and distribution of spots. In the K-pass sample (figure 3.1 f), there are fewer spots, with many of the remaining ones present in small clusters. Since the passivation treatment is known to reduce the non-radiative carrier losses [34], this change in spatial distribution already suggests that these spots are related to the carrier traps in the film. A second point to note is that the normalized intensities of the spots are quite similar between the three films. This indicates that there is likely a similar work function and/or energetic state of these spots. I will clarify these points and provide further evidence in section 3.2.

Following these observations, I will next show a more statistical analysis of these two points before delving into the deeper understanding of these PEEM spots. First, as a side point, it is useful to estimate what the spatial resolution of the PEEM is for the imaging conditions on these samples. I show a line profile of a small cluster of spots from an I-only sample in figure 3.2, from which a rough estimate, based on an 84-16% edge step intensity criteria, shows that the resolution is no worse than about 40 nm. Note that this is without the use of a small contrast aperture, which if inserted could allow for slightly better resolution, but at a cost of longer image acquisition times; this point will be revisited in chapter 7. With this lower bound, I next show some statistics

of the images displayed in figure 3.1 d, e, and f. First, I show a histogram of the PEEM spot intensity in figure 3.2 b, where the spots are identified with an image threshold and connectivity algorithm. This again emphasizes that the K-passivated sample has a significantly reduced number of spots, while the intensity of individual spots is fairly similar between the samples. This is also seen from the size distributions of the spots shown in figures 3.2 c, d, and e for the three samples. Here, there is a slight increase in the spot size, between the I-only (figure 3.2 c) and I-Br (figure 3.2 d) samples, which may be correlated to the increased grain size observed in SEM (figures 1.4 c and d). The K-passivated sample also appears to show a slightly larger size of spots (figure 3.2), however this may be due more to the apparent clustering of spots, which the algorithm for identifying the spots cannot distinguish. In addition, the SEM grain sizes for the mixed halide samples, regardless of K-passivation, seems to be similar (figure 1.4 e). These points show that there are heterogeneous features on the sample surface which are comparable or even smaller than the grain size, however they may not be directly related to the grain morphology itself.

With these basic observations about the film heterogeneity from PEEM, I will now turn to spectroscopic measurements in the next section in order to provide a deeper understanding of what these spots are.

3.2 Photoemission spectroscopy of trap states

Following the PEEM observations in section 3.1, I now seek to develop a deeper understanding of the nanoscale spots distributed across the HOIP films. Here, I make use of the spectroscopic imaging capabilities of our PEEM instrument, as outlined in section 2.1. For this section, I primarily use now the fourth harmonic photon energy (6.2 eV), unless stated otherwise. Again, the pulse fluence is reduced to minimize space charge effects, and is typically of the order 10 nJ/cm^2/pulse due to the increased photoemission yield compared to the third harmonic. For all measurements shown here, the energy analyzer of the PEEM is set with an exit slit width of about 250 meV, which was chosen instead of the smaller slit (125 meV) in order to obtain a higher signal intensity at the cost of energy resolution. With the analyzer slit in, image exposure times were typically several tens of seconds, with a few averages per image. Images are again corrected with flat field normalization, and the background noise of the camera is subtracted using images with no photoemission intensity as references. The energy step size used was 100 meV, and the energy scale is referenced to the high kinetic energy edge of the gold position marker within each image.

With these conditions, I first show energy resolved images at several binding energies for an Iodine-only sample in figures 3.3 a, b, and c. At deeper binding energies (lower kinetic energy), a relatively more uniform image is observed (figure 3.3 a), compared to the third harmonic PEEM images shown in figure 3.1. The finer features in figure 3.3 a are related to the film morphology, and is discussed in chapter 7 in more detail. At images closer in energy to the Fermi level, a similar distribution of isolated nanoscale bright spots becomes visible (figure 3.3 b, c). The intensity at particular locations, as indicated by the blue and red circles in figures 3.3 a-c, can then be extracted from the image stack at different energies, from which we can obtain spatially resolved

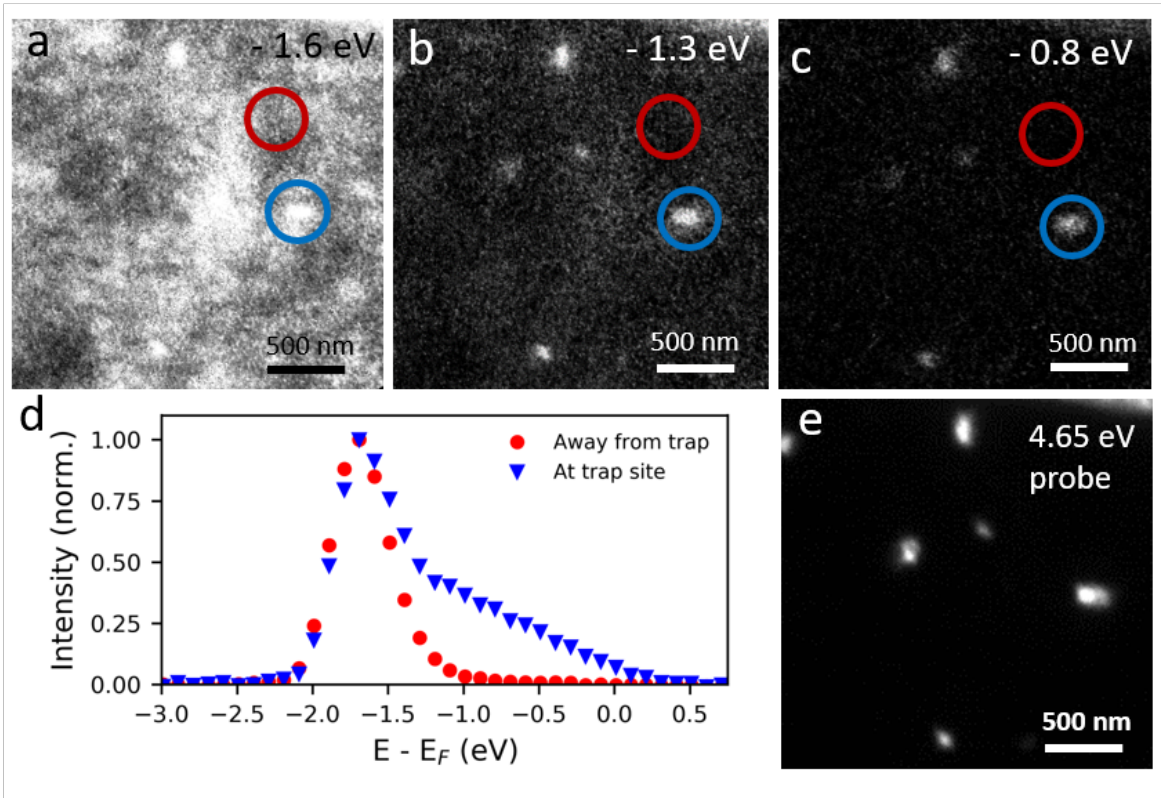

Figure 3.3: Photoemission spectroscopy of traps in HOIP. a, b, c) Energy resolved images, using the 6.2 eV probe, of an I-only sample at E-E$_F$ = -1.6, -1.3, and -0.8 eV, respectively. Note that the images are plotted on the same linear intensity scale. d) Photoemission spectra extracted from the spatial locations shown in a-c for a representative trap site (blue triangles) and away from any trap (red circles). e) PEEM image taken with the 4.65 eV probe at the same location as a-c.

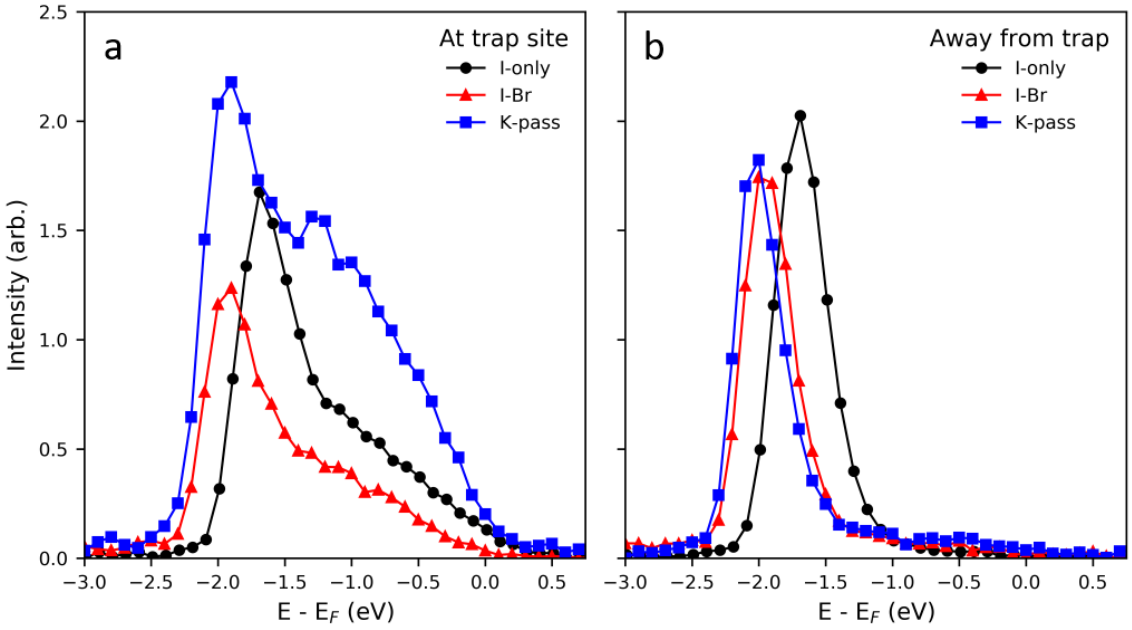

Figure 3.4: Comparison of photoemission spectrum from the different samples, taken with the 6.2 eV probe. Photoemission spectrum extracted from a) representative trap sites and b) trap-free areas. Note that the spectrum here are scaled by laser power and exposure time.

photoemission spectra. For the two regions selected, we observe several key features in the photoemission spectrum shown in figure 3.3 d. First, the main difference is the occupied density of states extending from roughly -1.3 eV down to the Fermi level (0 eV) for the bright PEEM spot (blue triangles, figure 3.3 d). For the other location with no bright spot, we only observe a peak centered around -1.7 eV (red circles, figure 3.3 d). This peak is most likely the edge of a valence band state, therefore the density of states extending to the Fermi level represent occupied states within the band gap. Hence, we associate these mid gap states as nanoscale trap sites, which we would expect to act as hole traps, and use this denotation as traps for the remainder of the discussion. Further, we note that we are observing *surface* trap states, due to the probing depth (estimated $<$10 nm) of our UV pulses and the short mean free electron path of the photoelectrons.

These occupied traps are then responsible for the image contrast at shallower binding energies. For comparison, using the third harmonic probe with lower photon energy, a PEEM image of the same location (figure 3.3 e) shows a very similar distribution as the energy resolved images in figure 3.3 b and c. Therefore, the image contrast seen with the third harmonic probe is due to the presence of these states, and not a difference in the material work function, for example. This is also apparent from the photoemission spectrum in figure 3.3 d, where the deep binding energy edge (low kinetic energy cutoff) at about -2.1 eV is the same for the two locations. This edge gives the same work function of about 4.1 eV, within the 250 meV energy resolution of the analyzer.

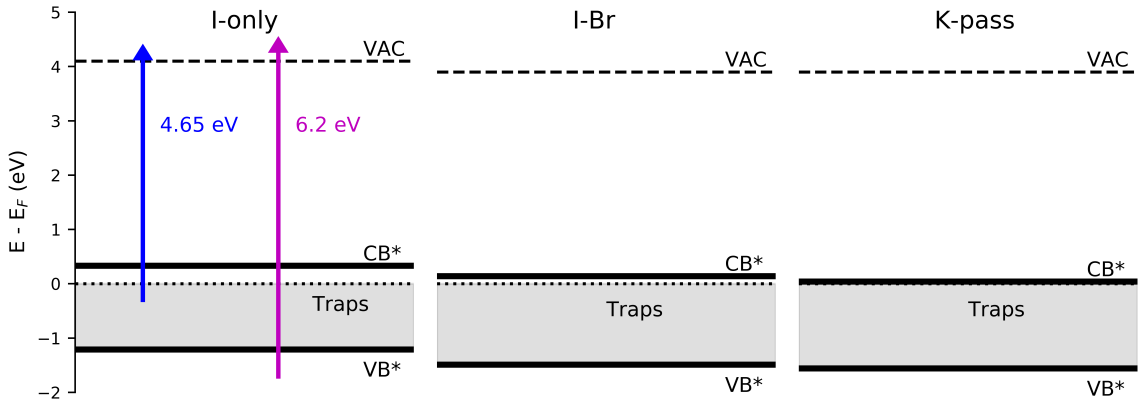

Figure 3.5: Energy diagrams derived for the iodine-only, I-Br, and K-passivated samples. The band gaps are estimated using the optical data in figure 1.3. The stars next to CB and VB represent that these are most likely not the actual valence and conduction band edges, due to the band structure predicted for the cubic crystal structure (see text). The states probed by the two different photon energies are also represented by the blue (4.65 eV) and violet (6.2 eV) arrows.

Following the observation of traps in the iodine-only film, I also compare the photoemission spectra of the two mixed halide films. In general, as seen in figure 3.4 a and b, the same features are seen in the photoemission spectrum from individual trap sites and trap-free locations, respectively. Note that here the photoemission spectrum are scaled by exposure time and laser intensity, and are not normalized, therefore differences in intensity may also arise from spatial variations. For all three samples, the nanoscale PEEM spots all show an occupied density of states in the mid gap, and are assigned as trap states (figure 3.4 a). For the trap free regions (figure 3.4 b), there is an apparent shift in the valence band feature of about 0.4 eV to deeper binding energy for the mixed halide samples. This would correspond to a deeper valence band, as expected for the wider band gap with bromine incorporation, but would also mean that the work function is smaller. However, due to the uncertainty from the energy resolution in determining the exact position of the Fermi level, these shifts are difficult to interpret at this time. A more detailed experiment with higher energy resolution and a better energy reference would be needed to clarify these sample differences. In any case, the main point here is that the three samples show a similar defect signature in photoemission spectroscopy, including the sample treated with potassium passivation. This suggests that there is a common or related microscopic origin to the trap sites.

To summarize the results of the photoemission spectroscopy measurements on these samples, energy diagrams of the estimated band gaps are presented in figure 3.5. Here, the valence band position and work function are estimated from the spectrum of the trap-free areas (as from figure 3.4 b), while the conduction band is placed based on the optical absorption and emission measured (from figure 1.3). The different states accessed by the two UV probes available is also shown by the blue and violet arrows. Note that it is very likely that the valence band measured here is not the true highest valence band edge, and as such is denoted as VB* (with corresponding CB* for uncer-

tainty in the conduction band). This arises from the fact that at room temperature, the $FAPbI_3$ structure is in the cubic phase, with the band gap transition at the high momentum R-point in the Brillouin zone [73]. While the picture for a mixed cation sample is more complicated, there are reports of mixed compositions of Cs with FA [74] and FA with MA [75] which show the room temperature cubic phase. Therefore, it is likely that the valence band maximum is at the high momentum R-point, which is not accessible with the low photon energy used for our measurements due to momentum conservation requirements in the photoemission process. Thus, we do not expect to directly probe the valence band at the optical band gap, and so the results here are likely shifted to lower energy by a few hundred meV for the VB and CB [73] for the valence bands near the Brillouin zone center.

3.3 Discussion of trap origins and implications

While our results here show for the first time the nanoscale distribution of surface traps, it is not the first spectroscopic photoemission measurement to observe such states. Similar mid gap states have been seen in various HOIP samples, notably on vapor deposited $MAPbI_3$ thin films [76], two-step solution process $MAPbI_3$ thin films [77], and even on cleaved single crystal $MAPbBr_3$ [78]. Wu et al. first considered films made with different precursors (PbI_2 and $PbCl_2$), and find that although both samples show similar mid-gap states in photoemission spectroscopy, the films with higher photovoltaic performance ($PbCl_2$) show different optical absorption dynamics and features [76]. An important observation by Kong et al., found that an iodine-rich growth environment shows an increased intensity of trap states [77]. Interestingly, even for a single crystal cleaved under UHV condition, similar mid-gap states were observed by Kollár et al. [78]. These observations on such differently prepared samples suggests that the origin of these traps is perhaps intrinsic, though possibly controllable through growth conditions.

One interesting point about our observations, as well as other UHV photoemission studies, is the prediction of hole traps. This is in contrast to several other works which have suggested that electron traps are the dominant type [79–82]. Since linear photoemission does not give information about the unoccupied states, it cannot rule out the possibility of electron traps being present. However, there is another possible explanation for the differences in such measurements. Recently, it was shown that the work function of HOIP can quite dramatically change based on environmental exposure, in particular to even residual levels of oxygen and water [83]. This suggests that the occupied states we observe under UHV could be changed into unoccupied states under ambient conditions, due to a several hundred meV increase of the work function. I will address this point again in chapter 5, where I will show with time-resolved measurements that these traps do indeed capture holes, as well as in chapter 6 where I will show results after oxygen treatments.

From previous studies in the literature, there are several possible types of defects which could occur at the surface of a HOIP material. For the prototypical HOIP $MAPbI_3$, several atomic vacancies (V_X) and interstitials (X_i) can lead to additional states within the band gap [2, 30, 84–87]. These include iodine (V_I), Pb (V_{Pb}), and

MA (V_{MA}) vacancies, and iodine (I_i) and lead (Pb_i) interstitials. Based on formation energies and calculated energy levels, I_i are predicted to be the defect most involved with deep-level carrier trapping. In particular, it has been predicted that I_i should rapidly trap holes [86–88]. These theoretical predictions suggest that the origin of the nanoscale traps we observe is most likely due to the iodine interstitial I_i. However, the defect nature in multiple cation systems has not yet been studied in such detail, so it is possible that there is a different defect structure. On the other hand, since these defects are more related to the lead-halide inorganic crystal framework, it is plausible that the mixed cation samples could show a similar defect nature to their single cation analogs.

To understand this important point, part of our ongoing collaboration with Cambridge has been to attempt to identify if there are local chemical and structural differences related to the observed traps. To this end, we have utilized a multi-technique approach combining PEEM imaging with nano x-ray diffraction (XRD) and x-ray fluorescence (XRF), as well as scanning electron diffraction (SED) measurements to build a more comprehensive view of the nanoscale properties around a trap cluster. The XRD, XRF, and SED measurements were led by Tiarnan Doherty at Cambridge, whom I share co-first-authorship with in our publication of the work [89]. Here, I will just summarize and discuss the main findings from the Cambridge-led side of the project, and how it relates to the PEEM results I have discussed so far. The first important finding from spatially-correlated measurements is that there are local variations in the halide distributions (iodine and bromine) occurring in the vicinity of the trap clusters. They find that there are particular film grains which have a lower bromine content, but however posses an excess of iodine, leading to an overall excess of total halide. This provides very strong evidence to the hypothesis that the deep traps we and others observe using PEEM and PES are associated with iodine interstitial (I_i) defects, following predictions from literature. The second important finding is that the grains with lower bromine content are also structurally distorted, compared to the grains with a stoichiometric composition. It is likely that the crystal distortion leads to the accumulation of excess iodine, resulting in trap formation, possibly because of strain at the grain boundary. However, further work will be needed to clarify this point, as well as why only some particular grains become distorted and form trap clusters.

In summary, here I have used PEEM imaging with low energy photon sources in order to detect and characterize the nanoscale defect distribution in mixed cation HOIP films. I find that there is a distribution of spots with sizes on the order of 100 nm or smaller which are due to occupied mid gap states in equilibrium. These states are present across the three sample compositions studied, including samples treated with potassium passivation. K-passivation instead reduces the number of nanoscale sites, though the remaining sites are comparable to those in unpassivated samples. I also discussed the likely origin of the observed traps, due to iodine interstitial defects, which is collaborated by the observation of local excess halide content. Future studies will still be needed to explain why the traps form in such a heterogeneous distribution, however our combined results already pinpoint several fundamental film differences and properties of the local trap clusters. The main importance of my work, so far, has then been to identify the nanometer length scale of such trap states in the film. Combined with the targeted chemical and structural measurements from our collaborators, we

are thus able to provide an insightful and direct view of the nanoscale properties of traps in HOIP films.

Chapter 4

Steady-state recombination losses

Having examined the microscopic nature of the mid-gap traps in chapter 3 using PEEM imaging, I seek to now show the relationship between these trap sites and the non-radiative loss of carriers in a steady-state regime. For this, I will rely on photoluminescence microscopy, which provides a measure of the radiative carrier recombination. I will combine PL microscopy with PEEM imaging to visualize how these losses are related to the trap distributions in section 4.1. Following the qualitative observations, I will then discuss the effect of such traps on reducing the radiative recombination yield in section 4.2.

4.1 PL microscopy

As first introduced in section 1.2, balancing the effect of non-radiative carrier losses is a key part of optimizing a material for use in optoelectronic applications. This implies maximizing the radiative carrier recombination for a material, which is readily measured through photoluminesence emission. Therefore, while indirect, PL can be used to understand changes in non-radiative losses within a material. Here, I will utilize this in order to study spatially how the PL is varying across our HOIP samples, which as introduced before, was one of the hints from literature about the presence of discrete, nanoscale traps.

As an initial characterization, I first show PL microscopy and spectroscopy for an iodine-only sample in figure 4.1. Similar to previous literature studies [25–29], I observe that there is a very heterogeneous distribution of the relative PL intensity emitted by the sample (figure 4.1 a). This particular measurement was done on a system (Nanofinder30, Tokyo Instruments) that can also measure the emission wavelength (energy). I find, however, that there is very little heterogeneity in the peak emission energy (figure 4.1 b). This suggests that local elemental segregation is not very significant for these triple cation samples, unlike in single cation mixed halide $MAPb(I_{1-x}Br_x)_3$ films [90, 91]. These two points are also visible from spectra taken from representative regions of the sample. For regions of good and poor emission, the difference in intensity is around factor of 4 to 10 (figure 4.1 c), while differences in the emission shape and energy are negligible (figure 4.1 d). Therefore, the emission characteristic between the good and poor PL yield areas is unchanged in these samples. What changes, then, is

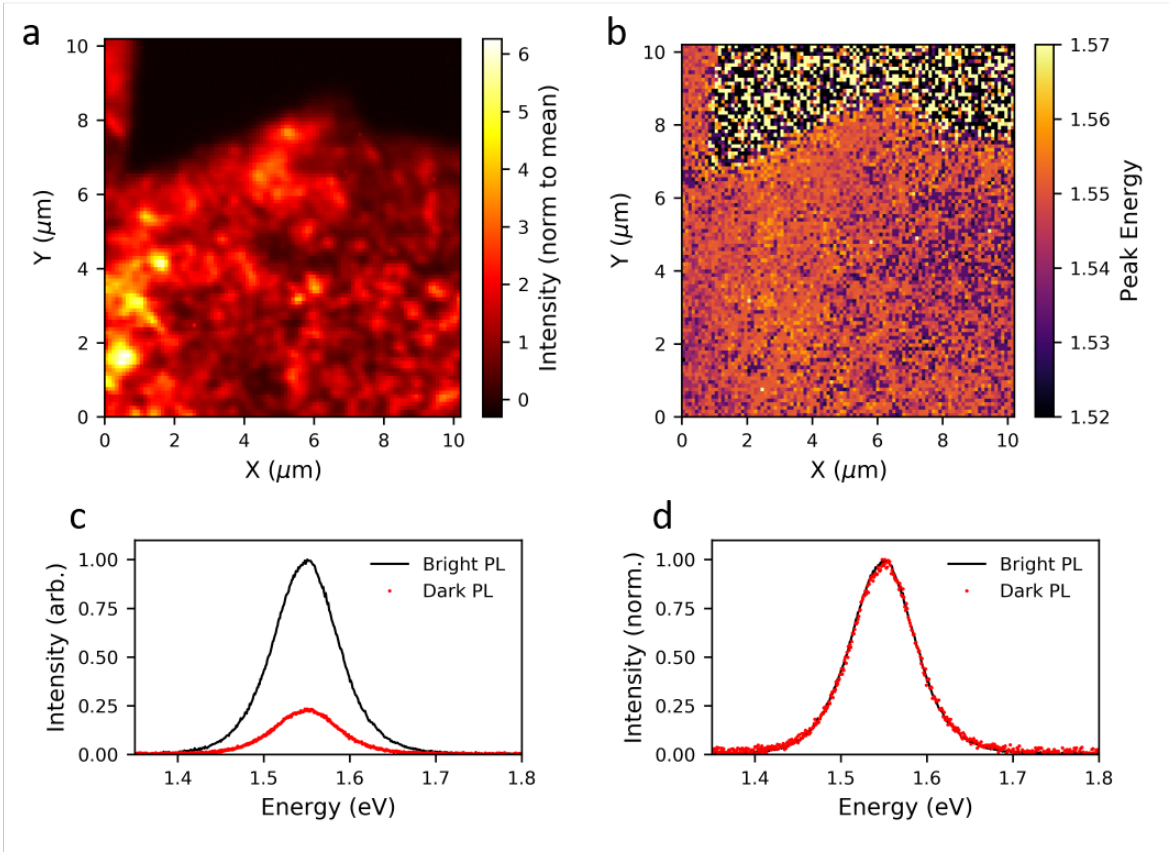

Figure 4.1: Hyperspectral PL mapping of an iodine-only sample. PL taken with 532 nm excitation and 50 nW of power through a 100x objective and scanned with a galvano mirror (Tokyo Instruments Nanofinder30 confocal microscope). a) PL intensity map. The dark region at the top of the image is the gold position marker. b) Map of the emission peak energy. c) representative PL spectra from bright and dark PL regions. d) same as (c), but curves are normalized to their maximum to compare the shape of the curves.

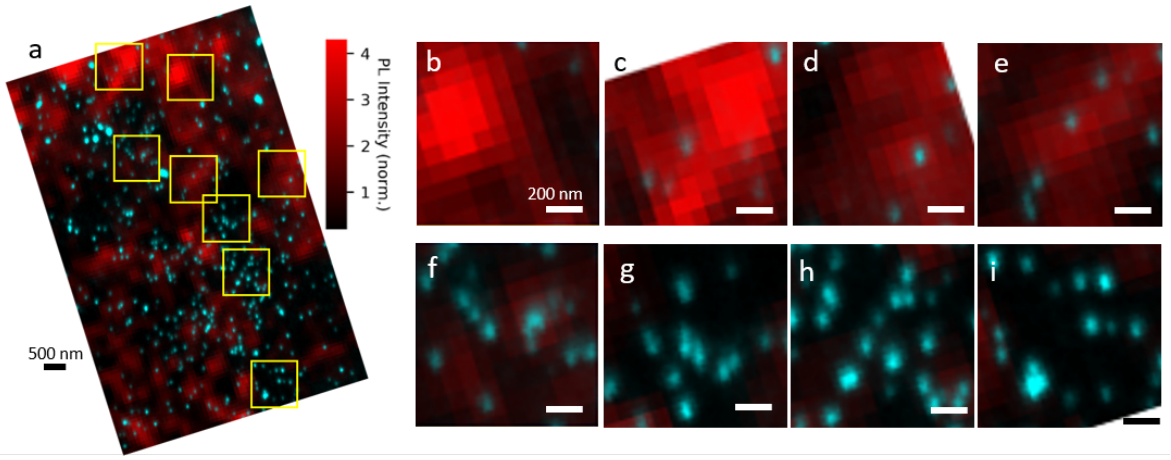

Figure 4.2: Overlay of an iodine-only PL map with a 4.65 eV probe PEEM image at the same location. a) wide-area overlay of the PL (same map as figure 4.1 a) and PEEM images. b, c, d, e) representative areas from (a) with higher PL intensity. f, g, h, i) representative areas from (a) with low PL intensity.

the efficiency of the process, which implies that the low PL yield areas possess more carrier traps.

To test this prediction, I now compare PL intensity maps and PEEM images of the trap sites, which were taken at the same locations. PEEM images were taken with the third harmonic (4.65 eV) probe, as discussed in chapter 3. The PL and PEEM images are then manually overlapped by referencing to nearby gold markers. I first consider the case for the I-only sample (same PL map as figure 4.1). Figure 4.2 a shows the large-scale overlap of the two images (with the au marker cropped out). For comparison purposes, several regions are marked by yellow boxes. In figures 4.2 b-e, locations with higher PL yield are selected, while figures 4.2 f-i show areas with low PL yield. It is apparent that the areas of good PL yield tend to show very few and less-intense trap sites, while the areas of low PL yield show an abundance of traps.

A similar case happens for the mixed halide and K-passivated samples. For these samples, we chose to use a different PL microscopy setup that sacrifices spectral resolution for rapid, high spatial resolution imaging (Leica TCS SP8 STED3X). Looking at the spatial distribution of the PL for I-Br (figure 4.3 a) and K-pass (figure 4.3 b) samples, the same qualitative trends can be observed. Regions of low PL yield (corresponding to darker purple/black colors) are often coincident with nanoscale trap sites in the PEEM image.

For all three samples, there are of course areas which do not strictly follow this trend. This is expected, however, due to several reasons. For one, differences in spatial resolution (about 300 nm in PL versus 40 nm in PEEM) as well as aberrations in the PEEM image which may distort it slightly will both blur the spatial correlation. Additionally, I again note that PEEM is a surface sensitive technique, and will be unable to probe bulk traps in the film which PL will be more sensitive to. Therefore, variations in bulk traps would also lead to a reduced correlation between the PL and PEEM images. A final point is that in the steady state, we must also consider the effect of carrier diffusion in the PL measurement. Due to the long carrier diffusion lengths

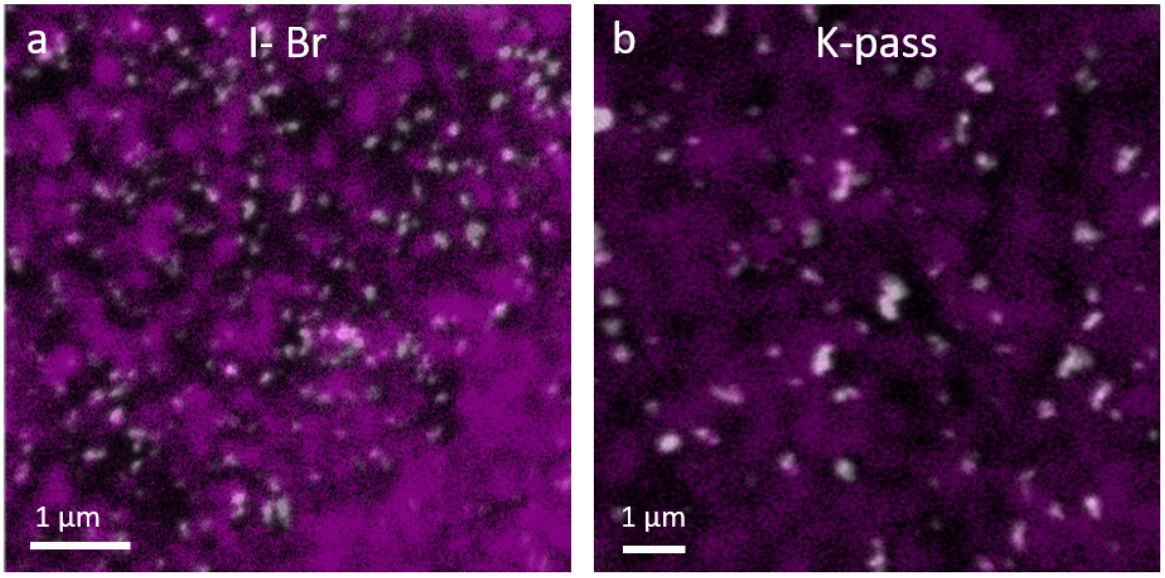

Figure 4.3: PL (purple color) and 4.65 eV probe PEEM (gray scale) overlays for mixed halide a) I-Br and b) K-passivated samples. Note that these PL maps are taken with a different instrument which is optimized for PL imaging but is spectrally integrated (Leica TCS SP8 STED3X confocal microscope). Excitation conditions were 442 nm with 2 μW and 633 nm with 1 μW for a and b, respectively.

(micrometer or more [14, 15]) and random connectivity of grains [27–29], it is possible that a single nanoscale trap could lead to reduced radiative emission over a much larger area of the film. Nevertheless, these measurements show that the surface traps states identified with PEEM are responsible for a significant part of the non-radiative carrier losses in these films on sub-micrometer length scales.

Following these initial observations, in section 4.2 I will next explore the correlation more closely between the nanoscale trap sites and relative PL yield.

4.2 Correlations between PL and trap sites

With the initial observations discussed in section 4.1, I now want to show more quantitatively how this nanoscale trap distribution is impacting the PL efficiency. We first look at pixel-by-pixel intensity correlations of the images from figures 4.2 a and 4.3, as shown in figure 4.4. For the I-only, I-Br, and K-pass (figures 4.4 a-c, respectively), there is a visible anti-correlation between the relative PL and PEEM intensities. This, in effect, reproduces the spatial correlation discussed in section 4.1, where regions of high PL yield have low PEEM intensity, while regions of high PEEM intensity show low PL yield.

Based on the SRH formalism first introduced in section 1.2 and the general equation for quantum yield (equation 1.1), I can make a qualitative prediction on how the local trap density should impact the PL yield. Starting from equation 1.1, I first note the non-radiative SRH coefficient A represents the time constant τ_T of recombination via a trap as $A = 1/\tau_T$. The time constant can then be represented as $\tau_T = 1/N_T R_{pop}$, where

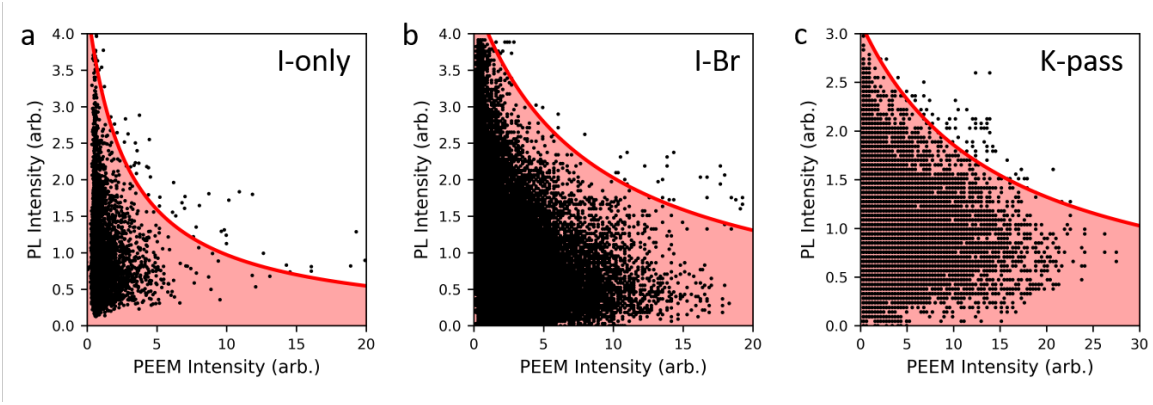

Figure 4.4: Intensity correlation plots between PL maps and PEEM images for a) I-only sample (image in figure 4.2 a), b) I-Br sample (image in figure 4.3 a), and c) K-passivated sample (image in figure 4.3 b). The axes for all three plots are normalized to their mean, and do not account for different experimental conditions. The red line and shaded region represents the inequality in equation 4.2.

N_T is the trap density and R_{pop} is the population rate constant of the trap [24, 92]. Since the photoemission intensity I_{PEEM} should be a linear measure of the mid gap trap intensity, the trap density is then related by a scaling factor s as $N_T = sI_{PEEM}$. Since the scaling factor s is unknown here and is not straightforward to obtain, I instead merge it with the R_{pop} constant to make a more general scaling factor. The PL quantum yield QE_{PL} can then be written as:

$$QE_{PL} = \frac{Bn^2}{snI_{PEEM} + Bn^2 + Cn^3} \tag{4.1}$$

Where B and C are the rate coefficients for bimolecular radiative and non-radiative Auger recombination, respectively, and n is the excited carrier density. For the carrier density used in PL measurements (estimated to be about 10^{16} to 10^{18} cm^{-3}), the Auger contribution can be neglected. In addition, as discussed in section 4.1, we expect there is a contribution of bulk traps, which we cannot probe with PEEM. Therefore, we consider only a relative PL intensity and simplify equation 4.1 as:

$$I_{PL} \leq \frac{I_0 Bn}{sI_{PEEM} + Bn} \tag{4.2}$$

Where the relative PL yield is given as I_{PL}/I_0 and the inequality represents losses due to unknown bulk defects. Using literature value for B of 2×10^{-11} cm^3/s [31], equation 4.2 is plotted (red line) for each correlation plot in figure 4.4, where I_0 is given by the maximum PL yield and the scale factor s is set by hand to represent the data. The shaded region under the curve represents the inequality due to an unknown bulk trap contribution. For the estimated excitation densities of 9×10^{15} cm^{-3}, 3×10^{18} cm^{-3}, and 2×10^{18} cm^{-3}, I obtain scaling factors of 6×10^4, 8×10^6, and 2×10^6 for the I-only, I-Br, and K-pass samples, respectively. Because the experimental condition between the I-only sample is very different from the mixed halide samples, it cannot be directly compared without an absolute measurement of the PL quantum efficiency.

Ultimately, however, the main result of this analysis was to show that the expected $1/N_T$ behavior of the PL yield is reproduced in the data. This shows that in a steady state condition, the non-radiative recombination at these trap sites is largely responsible for the reduced PL emission. Beyond this simple model, however, we must stress that in order to obtain an accurate quantitative result, one should also account for the diffusion of carriers in the PL measurement. This inclusion is not trivial, as it will likely require a numerical simulation of the various recombination processes. This will be partially addressed and discussed in sections 5.2.3 and 5.3, where numerical simulations to explain the measured trapping dynamics will be introduced. With some slight modification and extension of the model discussed in section 5.2.3, it should be feasible to also simulate the spatial distribution of PL emission, including the local nature of traps and accounting for carrier diffusion.

Beyond looking at the local intensity correlations, it is also useful to consider how the trap distribution over a larger area influences the PL yield between the different samples. As an initial comparison, I first look at the total number of nanoscale traps within a 6 μm by 6 μm area for several locations on mixed halide unpassivated (I-Br) and passivated (K-pass) samples, and compare it to the relative PL intensity over the same areas. As seen in figure 4.5 a, the data groups into two distributions, suggesting a correlation.

As discussed previously, the diffusion of carriers in the PL measurement may be important to consider. Therefore, instead of considering the number of traps in an area, I calculate the distribution of distances between traps, and focus on the nearest neighbor distances. As an example, the distributions for I-only, I-Br, and K-pass samples are shown in figures 4.5 b-d, respectively, where the effect of K-passivation on increasing the mean distance (green dashed lines) between traps is evident. Representing the PL yield in this way, as shown in figure 4.5 e, then suggests that the improved PL yield in passivated samples is due to the increased distance between traps. In essence, this means that with a larger distance between traps, an injected carrier will have a much smaller probability of reaching a trap as it diffuses through the film. As a further comparison, I also consider the relative PL yield of all three samples (figure 4.5 f) compared to the mean distance between neighboring traps, averaged over several locations. I again find that the PL yield differences are correlated with the trap distances, as shown in figure 4.5 g.

4.3 Non-radiative loss discussion

The observations above imply several important points. First, the nanoscale distribution of traps is an important control parameter, particularly from the view of passivation techniques. Interestingly, our observations show that either the K-passivation method is not uniform (e.g. spatial segregation) or that it is not able to change the synthesis environment enough to completely suppress trap formation. In the previous study by Abdi-Jalebi, et al., the 10% ratio of potassium iodide (KI) incorporated was chosen as the best balance between quantum efficiency and carrier mobility, in order to optimize the overall device performance [34]. They note that higher ratios of KI can further improve the quantum efficiency, to a point, however higher amounts eventually

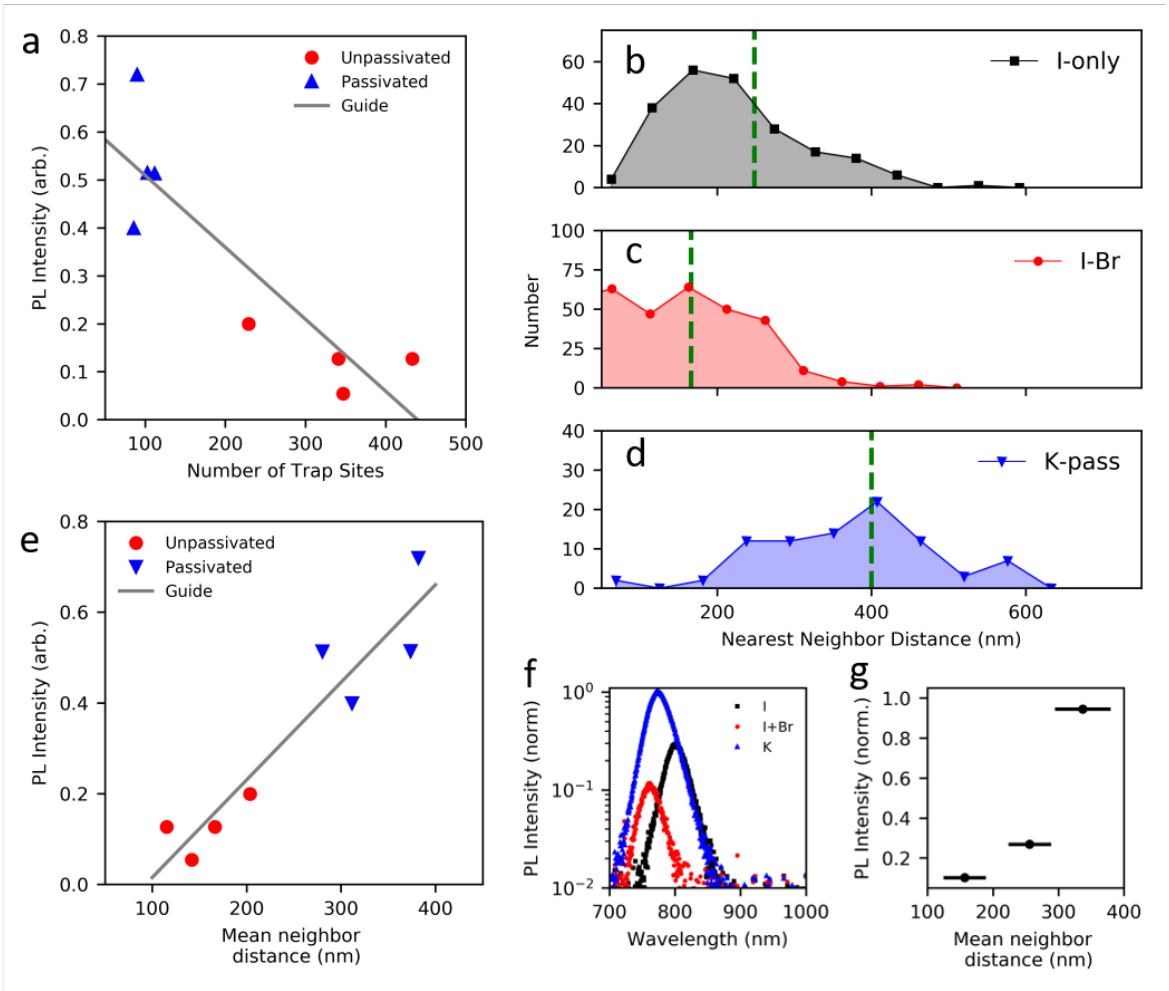

Figure 4.5: Correlations between statistics measured in PEEM to PL yield. a) comparison of relative PL yield to number of trap sites observed in PEEM in a several micrometer area for several unpassivated (I-Br) and passivated (K-pass) samples (Leica TCS SP8 STED3X confocal, same conditions as maps in figure 4.3, with PL intensity normalized by excitation power and camera gain). The gray line is a linear guide to the data. b, c, d) distributions of the distance between nearest trap sites measured in PEEM (4.65 eV probe) for an I-only, I-Br, and K-pass sample, respectively. The dashed green lines represent the means of the distributions. e) comparison of the relative PL yield to the mean nearest neighbor distance for several unpassivated (I-Br) and passivated (K-pass) samples. The gray line is a linear guide to the data. f) relative PL yield over several micrometer areas for 532 nm, 5 nW excitation (Nanofinder 30 confocal) for the three sample types. g) Comparison of the PL yields in (f) with mean trap distances for the different samples. The error bars represent the standard deviations of mean trap distances over several locations (3-4 areas).

lead to reduced performance due to the formation of K precipitates. Our results confirm that the 10% ratio is still not sufficient to remove all the trap sites in the film and eliminate the heterogeneous PL efficiency. Therefore, further work on optimizing the incorporation of KI into the synthesis, or in choosing a different passivation chemistry would still be fruitful for maximizing the overall device performance.

Another point is that manipulating the spatial arrangement, such as the distance between traps, can lead to improvements in PL efficiency, even if local trap densities are still relatively high. This suggests that carrier diffusion is very important to consider for minimizing trap losses. Normally, sample thicknesses are optimized for the device operation, such as matching the carrier diffusion length to the electrode spacing, or for optimal absorption of light. Our observations suggest that the distribution of traps in HOIP samples should also be considered in a similar way. For example, in a vertical device structure, if the distance between local trap sites is made to be comparable to or larger than the carrier diffusion length, then one would expect that there would be a reduced probability of a carrier being trapped as it travels to an electrode for collection. This also suggests that for a lateral device structure (e.g. the rear contact geometry used in many other solar cells), the K-passivated samples may show a significant improvement due to the much lower spatial density of local trap sites, leading to a reduced chance of carriers encountering a trap as they travel between grains. This point can also help explain why HOIP are so often quoted as "defect tolerant" materials [87, 88, 93] from a device perspective. The localized nature of the traps, in combination with barriers to carrier diffusion between grains [27, 29], work to reduce their contribution to non-radiative losses. Therefore, despite a high density of traps, HOIP films can still achieve relatively good performance in PV applications.

Thus, in this section of my work, I have shown the relationship between nanoscale trap sites identified in PEEM and the non-radiative losses in HOIP films. I found that the mid-gap states identified in chapter 3 are spatially correlated with areas of low PL yield, indicating that they are responsible for non-radiative carrier losses. Further, I have shown that due to the local nature of the trap sites, changing the spatial arrangement or spacing of traps, for example through K-passivation, can be used to control the macroscopic PL efficiency. Up to now, the work I have done considers only the time-averaged steady state of the traps. In chapter 5, I will next seek to understand and explain the dynamic trapping process happening at short time scales.

Chapter 5

Time-resolved microscopy of trapping dynamics

In the previous chapters 3 and 4 I have shown the results of steady-state photoemission microscopy and spectroscopy, which have revealed the presence of local nanoscale carrier trapping centers in our perovskite thin films. In this chapter, I will now investigate the kinetic processes of carrier trapping on short (sub nanosecond) timescales by using TR-PEEM. As outlined previously in section 2.2, the main strength of the TR-PEEM technique is the ability to observe changes in the electron population after carrier excitation with simultaneously high spatial (10s of nanometers) and temporal (few hundred femtoseconds) resolutions. Here, I have used this strength to measure the trapping kinetics at the local trap sites in section 5.1, while in section 5.2 I discuss in detail two potential mechanisms to explain the observed dynamics.

5.1 Time Resolved Imaging

As discussed in depth in chapter 3, I have shown that the spatial distribution of trap states in our perovskite films can be readily observed using the 4.65 eV (third harmonic) UV probe light. The photoemission intensity from these traps corresponds to the occupied mid gap states; hence, measuring the change in population of these states after excitation of carriers will provide a very direct way to observe carrier trapping processes. Therefore, all the time resolved measurements presented here will utilize a 4.65 eV probe, with a pulse fluence of around 100 nJ/cm^2, similar to the steady-state imaging conditions in chapter 3. In this section, I will discuss results following excitation with 1.55 eV pump pulses (experiments also using 3.1 eV excitation will be discussed in section 5.2), and then measure the resulting changes in photoemission intensity of the UV probe with a pump-probe style measurement, as described in section 2.2. All TR-PEEM data is first corrected by normalization to a reference, as described in section 2.3.2, and is then averaged over several (3-10) repeated measurements to allow for corrections of sample position drift and any slow intensity changes over time.

Now, I will first discuss the spatial dynamics seen in the three film compositions after excitation. Considering first the iodine-only sample, I focus on a location with a large number of local trap sites (corresponding to an area with low PL yield) as

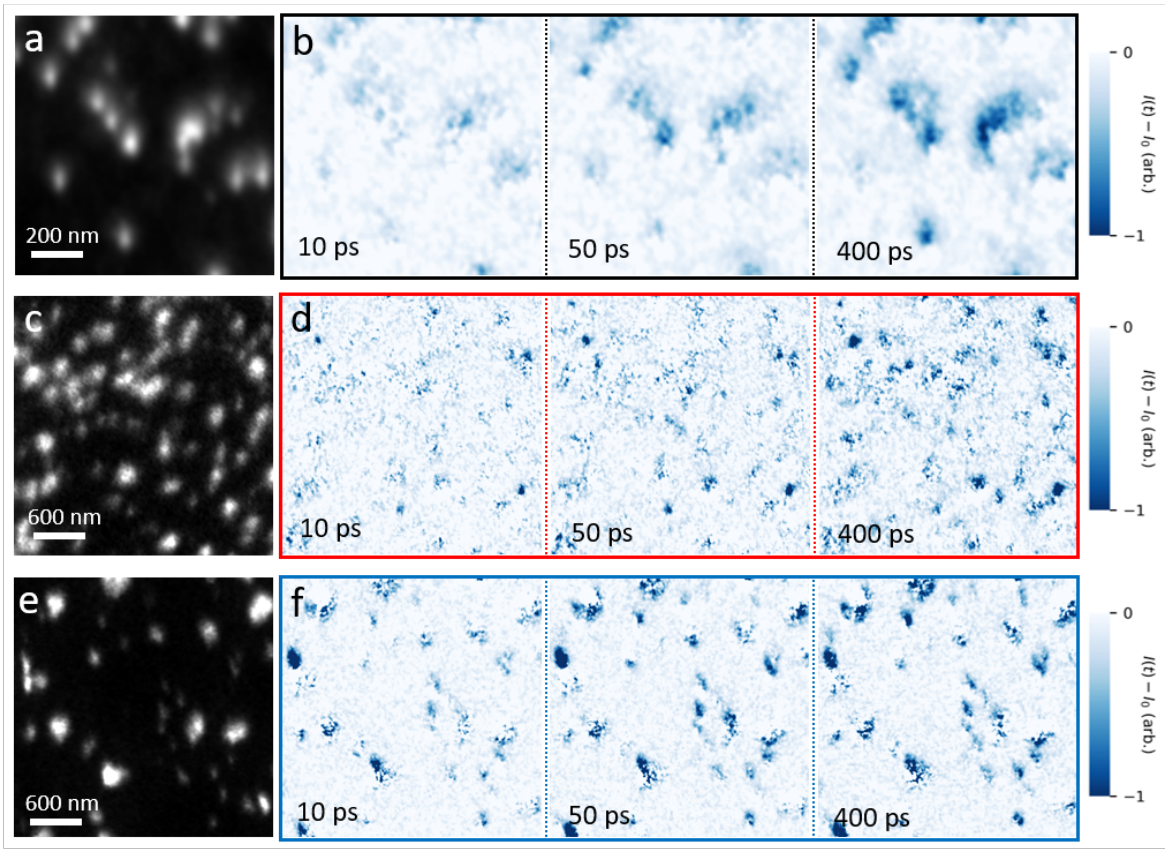

Figure 5.1: TR-PEEM images of trapping dynamics with 4.65 eV probe and 1.55 eV pump. a) PEEM image and b) TR-PEEM difference images of an I-only sample at different time delays with 20 μJ/cm^2 of pump fluence. c) PEEM image and d) TR-PEEM difference images of an I-Br sample after excitation with 100 μJ/cm^2 of pump fluence. Note that the absorption of the I-Br sample is low at the pump photon energy. e) PEEM image and f) TR-PEEM images of a K-pass sample with 20 μJ/cm^2 pump fluence. Note the images for each sample are cropped to different spatial sizes.

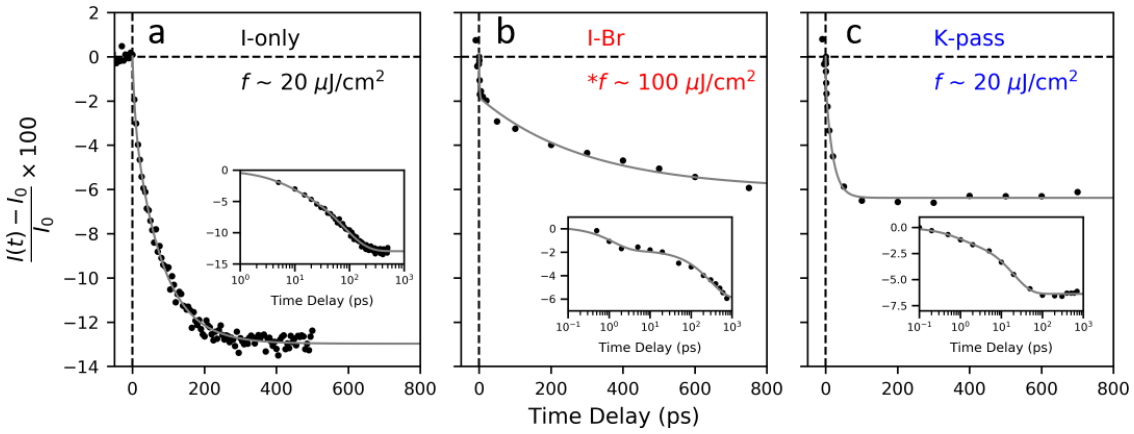

Figure 5.2: Extracted intensity curves of TR-PEEM dynamics, taken with 4.65 eV probe and 1.55 eV pump. The percent change in intensity is integrated over all trap sites within the 10 μm FOV for a) an I-only, b) I-Br, and c) K-pass samples. The gray curves are fits with a double exponential (equation 5.1). The pump fluence is given in each respective panel. The insets show the data and fit line plotted on a semi-log scale.

shown in figure 5.1 a. To view the pump-induced change in the signal, I then subtract the images at negative time delay (i.e. when the probe pulse arrives before the pump excitation) from the images at positive time delay (pump excites the sample before the probe pulse arrives). The resulting TR-PEEM images of the difference-signal are shown on a normalized scale (to roughly the maximum signal), and are shown for a few different pump-probe delays in figure 5.1 b. Looking at the images, there is clearly a decrease in the photoemission intensity localized at the trap sites, which happens of a several 10s of picoseconds (ps) timescale. For the mixed halide (I-Br, figure 5.1 c and d) and K-passivated (figure 5.1 e and f) samples, I observe a similar decrease in the photoemission intensity, albeit with a lower signal to noise. This decrease in the photoemission intensity indicates that electrons are being removed from the mid gap trap states, or equivalently, that holes are being trapped at these locations.

To view this dynamic more clearly, I extract the percent change in the photoemission intensity, integrated over all the trap sites within the PEEM field of view of roughly 10 μm. The percent change is $\frac{I(t)-I_0}{I_0} \times 100$, where $I(t)$ is the photoemission intensity at each time step, and I_0 is the average of the photoemission intensity at negative time delay (i.e. without photoexcitation of the pump). Plotting this quantity allows for more direct comparisons between different samples and measurement conditions, such as different probe fluences or camera exposure times. The resulting kinetic traces for the I-only, I-Br, and K-pass samples are shown in figures 5.2 a, b, and c, respectively. Here, the decrease in photoemission intensity of the trap sites can be seen on a 10s of picoseconds timescale. A double exponential fit to the data, as given by equation 5.1:

$$I(t) = A_1(e^{-t/\tau_1} - 1) + A_2(e^{-t/\tau_2} - 1) \tag{5.1}$$

yields short time constants (τ_1) on the order of a few picoseconds, while the slower time constant (τ_2) is on the order of a few tens to few hundreds of picoseconds. The fit results

are summarized in table 5.1, however this is only for a more qualitative comparison. This is because the band edge absorption around 800 nm (1.55 eV) changes rather dramatically, as can be seen from the absorption data shown previously in figure 1.3. Therefore, this data is not at comparable excited carrier densities; this point will be addressed more carefully in section 5.2.

Table 5.1: Double exponential fit results at fixed 1.55 eV pump fluences

Sample	Fluence (μJ/cm^2)	A_1	A_2	τ_1 (ps)	τ_2 (ps)
I-only	20	2.4 ± 0.4	10.5 ± 0.3	6.8 ± 2	79 ± 3
I-Br	100	2.0 ± 0.3	4.2 ± 0.4	1.3 ± 0.5	300 ± 80
K-pass	20	1.2 ± 0.2	5.2 ± 0.2	0.8 ± 0.4	20 ± 2

Nevertheless, these parameters still allow for some important qualitative observations. First, is that the initial signal dynamics are not pulse width limited. Our estimated time resolution, which is the convolution of the pump and probe pulse durations, is roughly 300 fs from measurements on GaAs. However, the initial dynamic I measure here is roughly a picosecond at the shortest. This means that there is no significant direct excitation of carriers from the occupied trap states, which would show as a pulse width limited transient signal exactly at zero time delay. This observation is not unusual considering our HOIP films, however, where we do not see significant sub band gap absorption or emission (figure 1.3) [34]. A second observation here is that the signal develops over a relatively slow time scale of 10s of picoseconds or longer, and the process does not follow a simple single exponential decay. This is most clear for the I-Br sample (figure 5.2 b), where there are two very distinct time scales visible in the data. This suggests that there may be multiple processes influencing the trapping kinetics. However, this rough time scale already agrees fairly well with time-domain calculations of the expected hole trapping time at mid gap defect states [87]. The third point is that the signal is of decreasing PEEM intensity. From the discussion in section 2.3.3 on GaAs, we might have expected to see a signal corresponding to the excitation of free electrons above the Fermi level. However, I have observed no such signal in measurements so far on these HOIP samples, even for spectroscopic time-resolved measurements. This agrees with the discussion in section 3.3, where due to the crystal symmetry and band gap position for this phase of perovskite, we do not expect to be able to probe the highest valence or lowest conduction band edges with the photon energies available. Further supporting this, I also mention here that attempts at measuring a signal with the 6.2 eV (fourth harmonic) probe were also unsuccessful, showing that we are indeed not probing the states at the optical band gap.

With these basic observations in mind, I now seek to begin discussing and explaining the possible origins for the kinetics observed here. The first obvious process to consider is the monomolecular, Shockley-Read-Hall (SRH) type trapping [21]. An important point of this model is that the rate of carrier trapping will depend on the density of trap states. It was shown recently using TR-PEEM that this description is valid even for nanoscale trap sites in GaAs [62]. Therefore, we would then like to compare the signal from trap sites of different local density in our samples. As an example, the

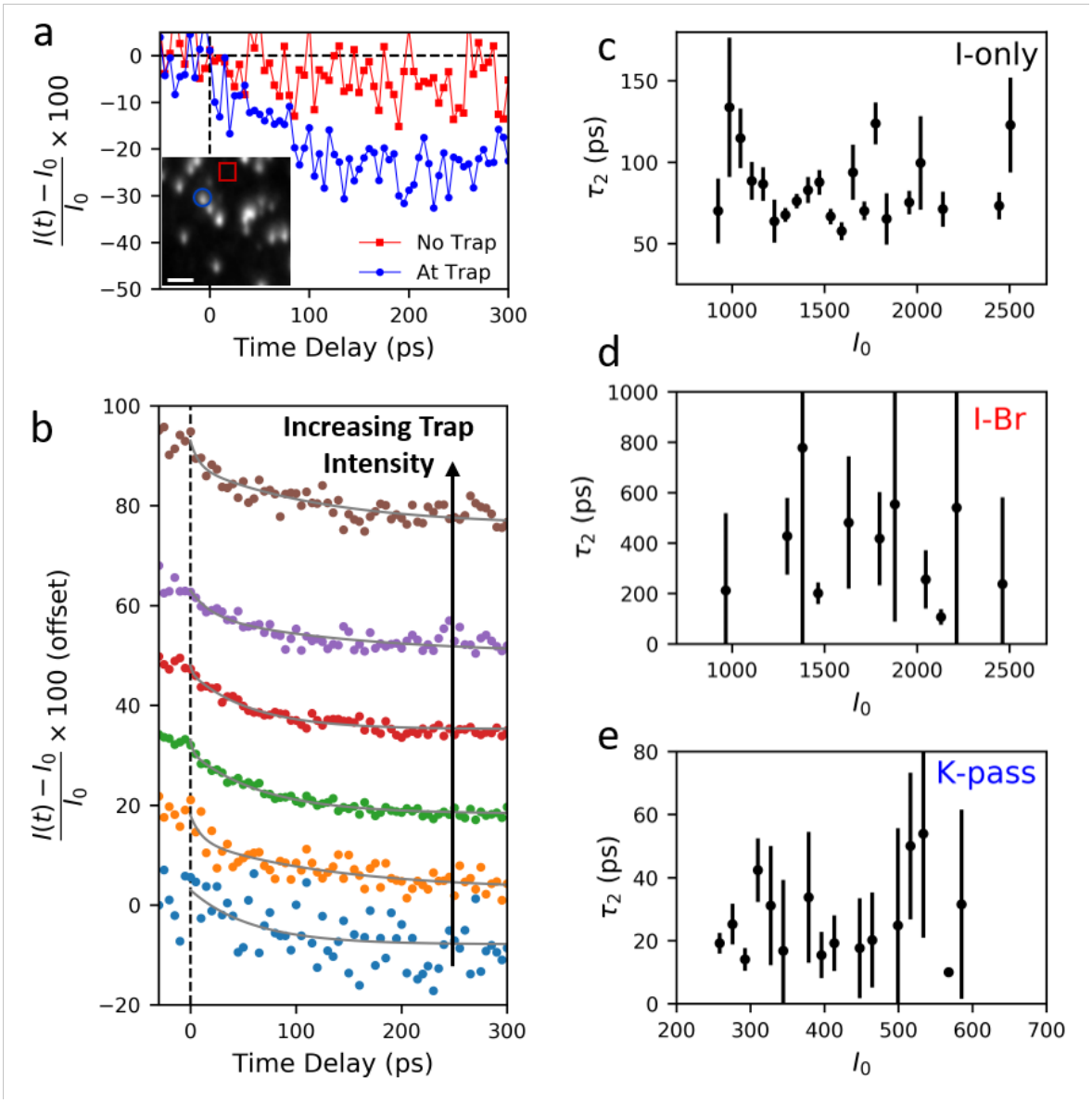

Figure 5.3: Bin analysis for comparing fitted time constants with the trap intensity. a) Spatially extracted TR-PEEM signal from a single trap site (blue circle in inset) and from an area with no trap density (red square). b) 6 binned and fitted TR-PEEM curves, where each color and fit line represents a single binned trap intensity level for an I-only sample. The extracted slow time constant for the data in figure 5.2 as a function of the trap intensity for the c) I-only, d) I-Br, and e) K-pass samples.

TR-PEEM signals from a single trap site and a trap-free area are shown in figure 5.3 a for the iodine-only sample. While the hole trapping signal is resolved, the low signal for a single trap site makes extracting reliable time constants difficult. To overcome this, I make use of the large number of trap sites within the image, and bin the TR-PEEM signals for traps of similar intensity. Several TR-PEEM curves extracted from different intensity bins for the iodine-only sample are shown in figure 5.3 b. From this, the dependence of the major intensity time constant (τ_2) as a function of the trap intensity (I_0) can be obtained. However, I find that there is no obvious dependence of the time constant, for either the iodine-only, I-Br, or K-pass samples (figure 5.3 c, d, and e, respectively). This contradicts the usual SRH behavior, where the trapping time should become faster for higher trap density.

These initial results and observations about the hole trapping character for the iodine-only and I-Br samples is part of the work published in *Nature* [89]. However, it is clear that the kinetics of the trapping process observed here are not so trivial, and require a more comprehensive analysis. Therefore, I next turn to more systematic measurements, along with modeling and simulation of the trapping kinetics, in section 5.2.

5.2 Trapping Kinetics

As introduced in section 5.1, the local trap states in our HOIP samples show complex trapping kinetics. In order to understand the details of the trapping process, I introduce a systematic study of the dynamics in this section. First, I will discuss experiments done under different excitation wavelengths (1.55 eV and 3.1 eV) and across a range of pump fluences. For the sake of comparison, I only focus on measurements from the mixed halide samples (I-Br and K-pass), which are closer in composition. Following the experimental results, I will then discuss in some detail two possible mechanisms to explain the observed trapping dynamics, namely a trap-assisted Auger processes and diffusion limited trapping.

5.2.1 Fluence Dependence

One of the key parameters for unveiling differences in recombination kinetics is to vary the density of generated carriers. As illustrated previously in equation 1.1 and figure 1.2 for the steady-state case, the three prototypical types of recombination (SRH, radiative, and Auger) have different dependencies on the carrier density. Similarly, for the out of equilibrium case in a time resolved measurement, they will show different recombination kinetics. Thus, varying the initial carrier density can allow for examining the different recombination processes. Therefore, to understand the trapping kinetics in our HOIP samples, I have performed TR-PEEM measurements at different pump fluences on the mixed halide (I-Br and K-pass) samples. In addition, I have done this at two different pump wavelengths (energies) of 800 nm (1.55 eV) and 400 nm (3.1 eV). The experimental conditions were otherwise kept the same as in section 5.1.

Similar to the case of 800 nm excitation shown in section 5.1, 400 nm excitation also shows a decreasing photoemission intensity on a picosecond timescale. For both the

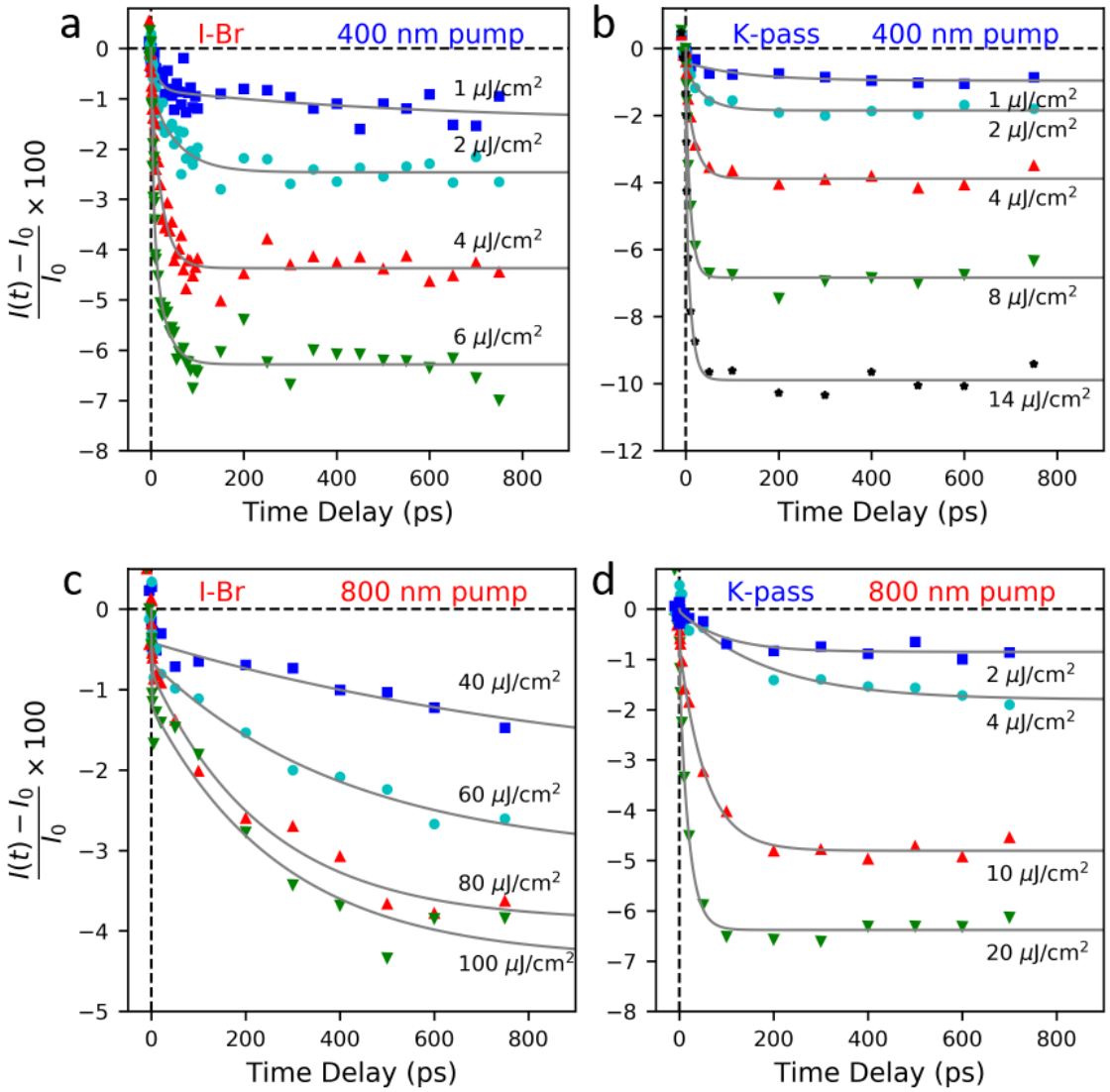

Figure 5.4: TR-PEEM intensity curves extracted over all traps in the 10 μm FOV as imaged with the 4.65 eV probe for different excitation conditions. a) I-Br sample with 400 nm (3.1 eV) excitation. b) K-pass sample with 3.1 eV excitation. c) I-Br sample with 800 nm (1.55 eV) excitation. d) K-pass sample with 1.55 eV excitation. The gray lines are fits with a double exponential function (equation 5.1).

I-Br and K-pass samples (figure 5.4 a and b), there is a similar intensity and timescale for an equivalent pump fluence. However, the overall dynamics are visibly faster with 400 nm excitation compared to 800 nm excitation (figure 5.4 c and d). In addition, the dynamics with 800 nm excitation appear different between the I-Br and K-pass samples (figure 5.4 c and d), where the dynamics are slower for the I-Br sample. The reduced intensity (and subsequently, higher pump fluence needed) for the I-Br sample with 800 nm excitation is due to the larger band gap for this composition (figure 1.3 b), making the absorption process unfavorable. To compare the data more directly, I again use a double exponential fit (equation 5.1) to extract amplitudes and time constants from the data (gray lines in figure 5.4). Additionally, the differences in the band gap and excitation wavelength are accounted for by converting the pump fluences to an estimated carrier density n using the equation:

$$n = f\alpha(1-R)(1-e^{-\alpha d})/E_{ph} \tag{5.2}$$

where f is the pump fluence, α is the absorption coefficient, R is the reflection coefficient, d is the sample thickness, and E_{ph} is the energy per photon, given by $E_{ph} = ch/\lambda$, where c is the speed of light, h is the Planck constant, and λ is the wavelength. R was measured to be roughly 0.2 in these experiments and d is approximately 500 nm. α was estimated to be 0.1 and 1 μm^{-1} for 800 nm excitation in the I-Br and K-pass samples, respectively, and roughly 10 μm^{-1} for 400 nm excitation for both samples, following the available optical data [12, 34]. Note that the absorption coefficients may be rather inaccurate, since there is not as detailed optical data for the mixed cation compositions, and as such the coefficients are primarily estimated from data on $MAPbI_3$, though the order of magnitude should be similar.

The results of the double exponential fits as a function of carrier density are shown in figure 5.5. There are several important observations to note about the extracted constants. First, the amplitudes (A_1 and A_2) for all four combinations of sample and pump wavelength are (nearly) linear with excitation density (figure 5.5 a and b). This indicates that even at this moderately high carrier density, the absorption process is still linear, suggesting that there are no multi-photon absorption processes, and further, that there is no saturation of the TR-PEEM signal. In some cases, the amplitude starts to appear sub-linear at even higher carrier densities, however this is difficult to interpret because at very high carrier densities the samples begin to degrade. To avoid complications with interpretation, these very high carrier density experiments are excluded from this analysis, and the measurements shown here are taken before sample deterioration becomes visible.

The second point of interest is that the fast τ_1 time constant is independent of the excitation density and wavelength (figure 5.5 c). Its average value is 2±2 ps (± standard deviation), which is slower than our temporal resolution of about 300 fs (dashed black line in figure 5.5 c). The third point, in contrast to the τ_1 behavior, is that the slower time constant τ_2 shows a very clear excitation density dependence (figure 5.5 d). At high density, τ_2 becomes as fast as 10 ps, while at lower density (particularly for 800 nm excitation cases) it becomes several hundred picoseconds and starts to exceed the time delay measurable by our TR-PEEM setup. Additionally, scaling the fluences to carrier density also partially reconciles the differences between excitation wavelength

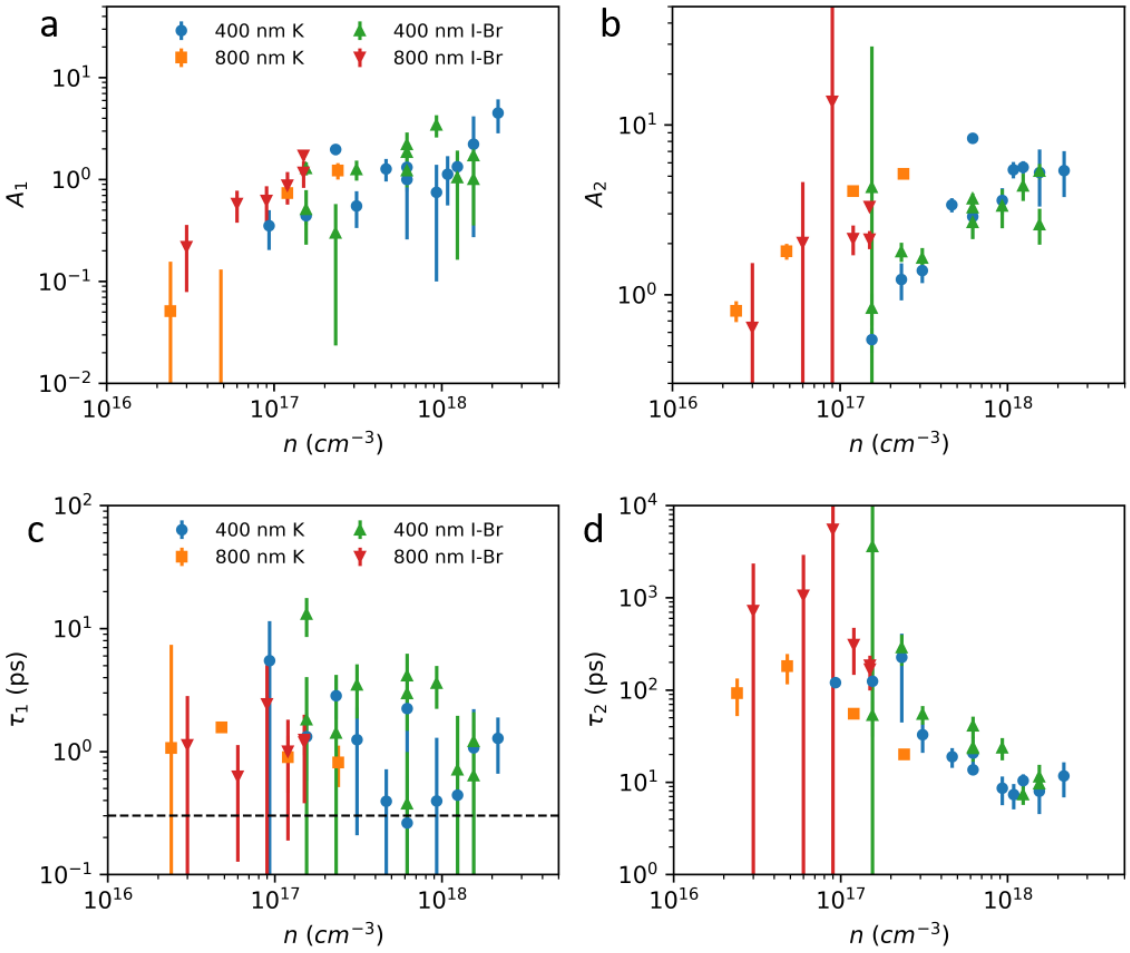

Figure 5.5: Fit parameters, using a double exponential function, for TR-PEEM data under different excitation conditions and for different samples. a, b) A_1 and A_2 amplitude constants. c, d) τ_1 and τ_2 time constants. Error bars are the standard error from fitting. The dashed line in (c) represents the estimated temporal resolution of the TR-PEEM setup.

for the τ_2 time constant, though there is still a significant difference between 800 nm excitation for the I-Br and K-pass samples (red triangles and orange squares in figure 5.5 d, respectively). This discrepancy may be due to inaccuracies in estimating the absorption coefficients at 800 nm.

From these observations, several conclusions can be drawn about the kinetic processes happening here. The first point is that since there is no saturation of the signal amplitude with increasing carrier density, it seems that the trapping process does not completely fill the trap, at least on these time scales. This would suggests that either the local trap density is very large (10^{19} cm^{-3} or higher) or that there are competing processes which detrap the holes (i.e. recapture electrons from the valence band). The first scenario seems less plausible at a glance, considering that the reported ranges of trap density observed in most HOIP films is typically $10^{15} - 10^{18}$ cm^{-3} [23, 24, 92, 94]. However, given the energetic position of the traps of roughly a few hundred meV from the conduction band edge (as a rough estimate from our photoemission spectroscopy data), the calculations by Kirchartz [93] would in fact suggest such a large density of traps, on the order of $10^{19} - 10^{20}$ cm^{-3}. Such a high trap density in that case is required due to the need for absorption or emission of many low energy longitudinal optical phonons involved in the trapping process in order to reach an effective carrier lifetime comparable to experimental results [93]. The second scenario of de-trapping is also important to consider. Molecular dynamics calculations of the hole trapping process at mid gap trap states have predicted that the trapped holes can release back into the valence band on a time scale of about 400 ps, while the capture of an electron from the conduction band (relaxation of the hole to the ground state) would happen on a much longer scale of hundreds of nanoseconds [87]. Considering the time scales we observe here, this calculation suggests that the reason we do not fill the trap states completely is due to release of holes back into the valence band, such that at several hundreds of picoseconds we reach a steady-state of hole trapping and release, leading to a flat signal at longer time delays.

This in turn coincides with the point regarding the fast time constant τ_1. The independence of the time constant with carrier density is a reasonable indicator for SRH trapping, which has a time constant that is independent of the excited carrier density. Therefore the smaller amplitude, few picosecond dynamic we see could correspond to the initial carrier trapping process, which is roughly on the time scale calculated in molecular dynamics simulations of around 5-30 ps [87]. However, this then leaves open the question of what process determines the slower time constant τ_2, in particular how to explain the observed dependence on the carrier density. The dependence indicates that multi-body processes are likely involved and need to be considered. I will explore this last point in more detail shortly in section 5.2.2.

5.2.2 Trap Assisted Auger

In order to determine what kinds of multi-body processes may be involved, we look more closely at the observed τ_2 dependence on carrier density. The data can be fit well with a power law $\tau \propto n^{-1}$, as shown in figure 5.6 a. This kind of dependence is characteristic of a *two body* process, with the most common example being bimolecular radiative recombination. However, as we are probing the occupation of a trap state,

we must consider processes which affect the population of trapped carriers. Thus, we consider instead a higher order Auger process. Normally, Auger is assumed to be a three body process, involving a combination of holes and electrons which recombine and transfer their energy to another carrier. However, if we take one of the three participants as the occupied trap (electron), then the process becomes effectively two body, in terms of the excited carrier density [95]. As outlined in figure 5.6 b, there are several different scenarios where Auger recombination can result in hole trapping. In scenario (I), a hole is trapped and excess energy is given to a free electron in the conduction band. In scenario (II), a free electron recombines with a free hole and transfers its energy to a trapped electron, causing it to detrap. In scenario (III), a hole is trapped (electron from trap recombines with a free hole) and transfers the energy to another free hole. These scenarios are essentially equivalent, as discussed by Staub [95], however the detailed kinetics must include both the electron and hole Auger processes to satisfy the total recombination.

Taking the limit of high carrier injection (where the excited carrier density is higher than the doping density), we can write the trap assisted Auger rate equation for a deep level trap following [95] as:

$$\frac{dp}{dt} = -cn_T p^2 \tag{5.3}$$

where c is the Auger coefficient, n_T is the trap density, and p is the excited hole density. This is inherently different from band-to-band Auger recombination, where the rate equation is proportional to p^3 (for $n = p$). The solution to equation 5.3 is straightforward and is given as:

$$p(t) = \frac{p_0}{p_0 c n_T t + 1} \tag{5.4}$$

where p_0 is the initial density of excited holes. This can be further rearranged to give the population of electrons in the trap $n_T(t)$, as opposed to the number of trapped holes $p(t)$ as:

$$n_T(t) = A\left(\frac{1}{Bt+1} - 1\right) \tag{5.5}$$

where $A = p_0$ and $B = cn_T p_0$ for simplification. Equation 5.5 then represents the reduced electron occupation of the trap due to hole capture. Comparing to the TR-PEEM data measured with 400 nm excitation, equation 5.5 accurately fits the data for both samples and for different excited carrier densities (figure 5.6 c). This model also fits the 800 nm excitation data for the K-pass sample, however for the I-Br sample, it starts to deviate significantly (figure 5.6 d).

By fitting the TR-PEEM data with equation 5.5, the product cn_T can then be extracted from the ratio B/A. The resulting product is plotted for the different samples, excitation wavelengths, and carrier densities in figure 5.7 a. The data for 400 nm excitation give similar results for both sample types across the carrier densities used here, while the grouping for the 800 nm excitation is wider, likely due to the deviations from the fit. The product cn_T is however roughly an order of magnitude smaller for 800 nm excitation, which would suggest that the Auger recombination process is sensitive

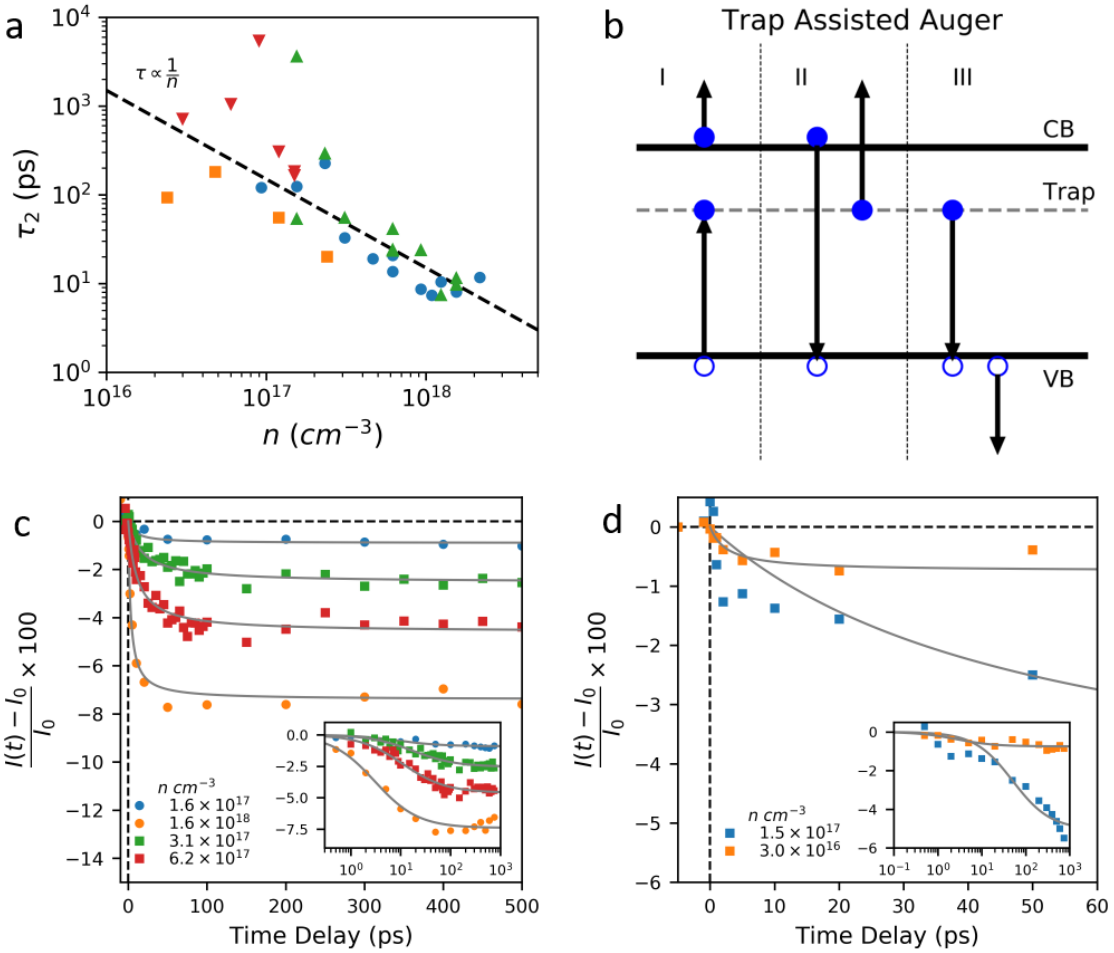

Figure 5.6: Trap assisted Auger analysis. a) Extracted slow time constants (same points as figure 5.5 d). The dashed line represents a fit to the line $1/n$. b) Schematic of various trap assisted Auger process which result in hole trapping. Electrons (solid blue circles) are removed from the trap states through different pathways (black arrows) involving other electrons or holes (open blue circles). c) 400 nm excitation trapping kinetics for a few K-passivated (circles) and unpassivated I-Br (squares) measurements. The grey lines are fits with equation 5.5. The inset shows the data and fits on a semilog scale. d) 800 nm excitation for an I-Br sample at two fluences. The grey lines are fits with equation 5.5; note that there is a significant deviation at shorter time delays. The inset shows the data and fits on a semilog scale.

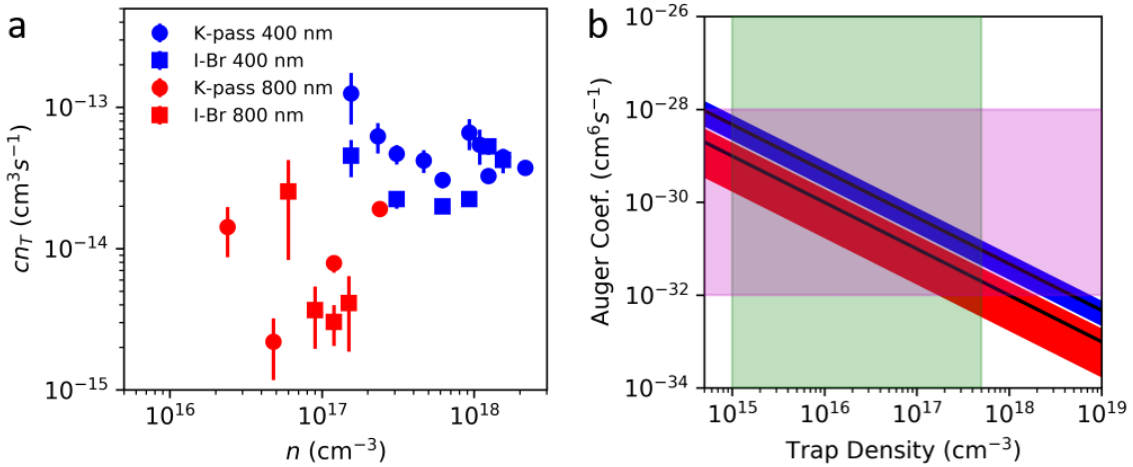

Figure 5.7: Extracted Auger coefficients. a) Product cn_T from the coefficients extracted from equation 5.5 for 400 nm (blue points) and 800 nm (red points) excitation for K-passivated (circle) and I-Br (square) samples as a function of estimated excitation density. Errorbars are the standard error from fitting. b) Calculated Auger coefficient (black lines) as a function of trap density (n_T) using the product cn_T for 800 nm (red shaded area) and 400 nm (blue shaded area) excitation. The width of the red and blue areas represents the width of the standard deviation calculated from the points in (a). The green shaded box represents the typical range of reported trap densities in HOIP films, while the shaded magenta box represents the range of Auger coefficients calculated by Staub et al. [95].

to the excess carrier energy when exciting above the band gap. This is represented more clearly in figure 5.7 b, where the resulting Auger coefficient for the 800 nm and 400 nm excitation (black lines in red and blue shaded areas, respectively) is plotted as a function of the trap density n_T.

At this point, the absolute trap densities in our mixed cation HOIP films are unknown. However, we can still infer several important points based on the data and simulations for $MAPbI_3$ and more recent results on mixed cation films. This is represented by the shaded boxes in figure 5.7 b, where the typical range of reported carrier densities in thin film HOIP is indicated by the shaded green box, while the range of calculated trap assisted Auger coefficients by Staub is shown by the shaded magenta box [95]. If we consider the Auger coefficient and compare it to that calculated by Staub [95], we find that for a trap depth of a few hundred meV (as estimated from our photoemission spectroscopy data, and as predicted from calculations [88] and recent experiments [96]), the calculated Auger coefficient would be approximately 10^{-29} cm^6s^{-1}. This value agrees with measured literature values for the Auger coefficient on similar mixed cation (Cs and FA) mixed halide (20% Br) films [31]. From the Auger coefficient measured here and plotted in figure 5.7 b, this would then suggest a deep level trap density of the order 10^{16} cm^{-3} in our samples. This estimate of the hole trap density is comparable to recent literature reports on similar mixed composition films and also in $MAPbI_3$ films [23, 24, 92, 94, 96].

Therefore, I have found here that the trap assisted Auger recombination process can potentially explain part of the observed hole trapping kinetics on a sub-nanosecond timescale. In particular, this model holds for a moderate to high carrier density regime. At lower carrier densities, however, particularly as mentioned before for the 800 nm excitation in I-Br samples, this process cannot accurately describe the trapping kinetics. In addition, this model does not reconcile the behavior seen in figure 5.3, where the time constants are independent of the local trap density, which goes against the derivation in equation 5.5. Due to these shortcomings, I will discuss an alternate kinetic model in section 5.2.3.

Considering solar cell devices operating under 1-sun conditions, where the carrier density is roughly 10^{15} cm^{-3}, the trap assisted Auger process should then not be so significant. However, for concentrator type solar cells [97] and in light emitting diode (LED) devices [98], where injected carrier densities can be quite high, Auger recombination is a serious concern and is already known to be a limiting factor. The interesting point here is that if the main Auger recombination process is due to trap assisted interactions, then there is a possibility for external control of the trap densities or composition to manage the losses from Auger recombination. This is in contrast to band to band Auger recombination, which has transition rates primarily determined by the electronic band structure, meaning that the material itself must be changed in order to control the Auger recombination rates.

5.2.3 Diffusion Limited Trapping

While the trap assisted Auger process discussion in section 5.2.2 can explain a portion of the TR-PEEM observations, it is still important to consider alternate kinetic processes which can better explain the observed kinetics and to gain new perspectives. Stepping

back, I first consider the kinetics again by starting with the initial observations shown in section 5.1, where we observed the overall trapping timescales ranging from several tens to a few hundred picoseconds. On this timescale, one of the most commonly observed phenomenon in semiconductors (other than radiative recombination) is the diffusion of carriers [44]. If we consider this scenario, we can do a simple order of magnitude calculation for the diffusion length related to the trapping process (L_T):

$$L_T = \sqrt{D\tau_t} \tag{5.6}$$

where D is the diffusion coefficient and τ_t is the trapping time. Using a typical value for the (*intra*-grain) diffusion coefficient of 1 cm^2s^{-1} [29, 34, 94] and a value of τ_t of roughly 80 ps from our measurement (considering the I-only film) gives a trapping diffusion length of about 90 nm. This length scale is reasonably close to the grain radius (figure 1.4 b and c) and is comparable to half the mean distance between neighboring traps that was measured in figure 4.5 b. This suggests that physically, the trapping kinetics we measure could be influenced by diffusion of carriers to the trap sites from within a grain or adjacent grains, and warrants a more detailed investigation.

To develop the kinetic model for the diffusion of carriers, I will consider two possible scenarios. In the first case, I will assume that the slab of perovskite material contains local trapping centers (red boxes in figure 5.8 a) and no boundaries which limit diffusion. Therefore, after exciting carriers (for the moment just considering the case of holes), diffusion will result in additional carriers being funneled towards the traps. In the second case, I will further assume that there are boundaries to carrier diffusion (figure 5.8 b), representing grain boundaries with a reduced diffusion coefficient. The resulting system of differential equation in 1-dimension (1D) can then be written as:

$$\begin{aligned} \frac{dn_T}{dt} &= k_t n_c (N_T - n_T) \\ \frac{dn_c}{dt} &= D\frac{\partial^2 n_c}{\partial x^2} - k_t n_c (N_T - n_T) - k_b n_c^2 \end{aligned} \tag{5.7}$$

where n_T and n_c are the population of trapped and free carriers, respectively, as functions of time and space, N_T is the trap density, k_t is the trapping coefficient, k_b is the bimolecular radiative recombination coefficient, and D is the diffusion coefficient, which is allowed to spatially vary in the case of simulated grain boundaries. Exact solutions of diffusion equations are not always possible, so I turn instead to numerical solutions of this system of equations using a finite difference (forward difference in time and central difference in space (Euler)) scheme [99]. Numerical solutions were calculated for a 1D line 3000 nm long with a 1 nm step and a time step of 1 fs. The local trap is simulated by setting k_t to be 1×10^{-7} cm^3s^{-1} (corresponding to a 1 ps trapping time, $k_t = 1/(N_T\tau)$) in a region of 100 nm in length, centered at $x = 0$, and zero elsewhere. The radiative coefficient k_b was set to 2×10^{-11} cm^3s^{-1} from literature values [31] and from measurements done at Cambridge, however its contribution on a sub nanosecond timescale is generally negligible, except at very high free carrier densities. The trap density N_T was chosen to be 1×10^{19} cm^{-3}, and the initial carrier density N_C is 1×10^{18} cm^{-3} for this first simulation.

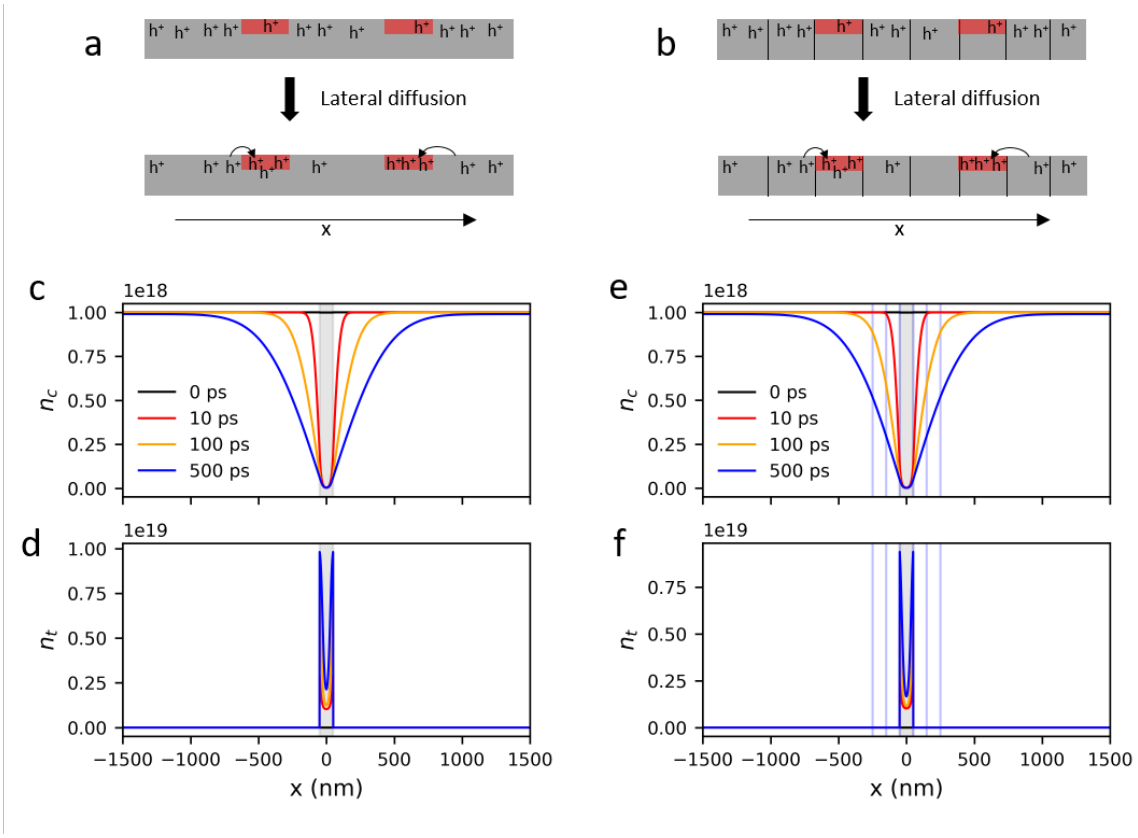

Figure 5.8: Diffusion limited trapping model in 1-dimension. Schematic drawing of the hole (h^+) diffusion process into local trap sites (red shaded boxes) for the cases of a) a uniform slab of material and b) a material broken up into smaller grains. c) the simulated 1D profile of the free carrier population (n_c) at different times in the presence of a local trap (gray shaded box), assuming there are no grain boundaries. d) the corresponding 1D profile of trapped carriers (n_t) for the case in (c). e) 1D profile of free carriers, but with simulated grain boundaries ($D_b = 0.1$ cm^{2}s^{-1}, grey vertical lines). f) corresponding 1D profile of trapped carriers for (e). For the simulations in c-f, the trap density N_T is 1×10^{19} cm^{-3}, the excited carrier density N_C is 1×10^{18} cm^{-3}, the intra-grain diffusion coefficient D_i is 1 cm^{2}s^{-1}, and the trapping coefficient k_t is 1×10^{-7} cm^{3}s^{-1}.

The calculated line profiles for the free carrier population (n_c), assuming a diffusion coefficient D_i of 1 cm^2s^{-1} [29, 34, 94] and no grain boundaries is shown in figure 5.8 c for a few time steps. The spatial position of the trap is given by the gray box, while the corresponding population of trapped carriers (n_t) is shown in figure 5.8 d). The same profiles for the case of simulated grain boundaries, where the diffusion coefficent at a 3 nm boundary strip (D_b) is set to be 0.1 cm^2s^{-1}, is shown in figure 5.8 e and f, with the boundaries for 5 grains shown as the gray vertical lines. These numerical calculations confirm that after the initial population of carriers at the trap are captured, diffusion will result in a reduction in the population of free carriers in adjacent grains. This further supports the observations in chapter 4 that the photoluminescence of grains near a trap site can be substantially quenched over an area of several hundred nanometers or larger (figure 4.2).

Now, I consider more closely the time dynamics. Integrating the population of trapped carriers n_T at each time step, the resulting trapping dynamics can be represented in a similar way to the TR-PEEM data by plotting the change in trap occupation. First, I consider the case for a fixed initial carrier density, but vary the diffusion coefficient of the grain boundary (D_b), as shown in figure 5.9 a. This shows that the diffusion across the grain boundary is the limiting factor at long times, as might be expected. From different measurements reported in the literature, it is known that the carrier mobility of *intra* versus *inter* (or in single crystal versus solution process films) charge transport can differ by almost an order of magnitude [29, 94, 100]. This would suggests that a value of D_b on the order 0.01-0.1 cm^2s^{-1} is realistic, though it likely varies spatially (i.e. grain boundary to grain boundary) very strongly [27, 29].

Therefore, I will again consider two cases, where in one case there is no barrier to carrier diffusion ($D_i = D_b = 1$ cm^2s^{-1}), and a second case where there is reduced diffusion across the grain boundary ($D_b = 0.1$ cm^2s^{-1}). These two cases are plotted in figure 5.9 b and c, respectively, for several different initial carrier densities. In both cases, the population of trapped carriers has an initial fast component, followed by a slow tail. The fast component corresponds to the SRH trapping term in equation 5.7, while the slow tail is the result of carrier diffusion into the trap, which continues until the trap is completely filled. For this value of D_b, the effect of the grain boundary is not so strong, however it does slow down the long time dynamics. Hence, the time to reach a steady-state of trap filling decreases with increasing initial carrier density, which closely resembles the measured TR-PEEM dynamics. As a comparison, the data (with double exponential fits as guides) is shown again for the I-Br sample with 800 nm excitation in figure 5.9 d. Qualitatively, with only the simple model given in equation 5.7, the diffusion model is able to replicate the main trends of the measured data quite well.

Despite the qualitative agreement, there are still some limitations to this model. The most severe limitation is that the model in equation 5.7 only holds for the low carrier density and short time regime, which is roughly $N_C \lesssim 0.1 N_T$ in a one nanosecond window. At higher carrier density and longer times, the trap will become completely filled, resulting in a saturated trapped population. However, from the TR-PEEM measurements, we have not observed such a saturation of the signal intensity with increasing excitation density over a large range (figure 5.4). As discussed previously in section 5.1, there are predictions that the trapped hole can escape back into the va-

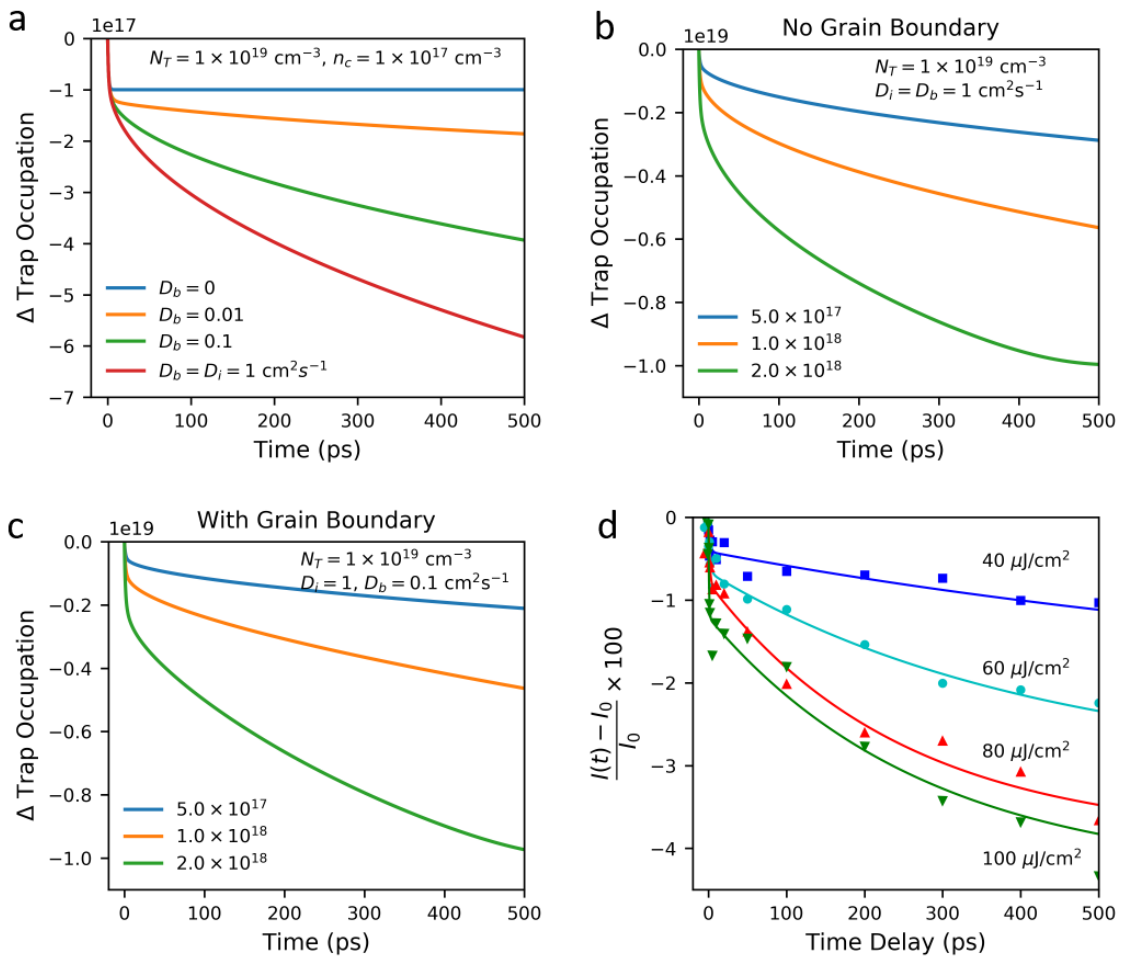

Figure 5.9: Kinetics of diffusion limited trapping. a) Calculated trapping kinetics for different values of the grain boundary diffusion coefficient D_b. b) Calculated trapping kinetics for different initial carrier densities and assuming no grain boundaries. c) same as (b) but including simulated grain boundaries ($D_b = 0.1$ cm^{2}s^{-1}). d) TR-PEEM curves of 800 nm excitation in I-Br HOIP films, for comparison with (b) and (c). Note that the solid lines are the fits with a double exponential function shown previously, as a guide to the eye.

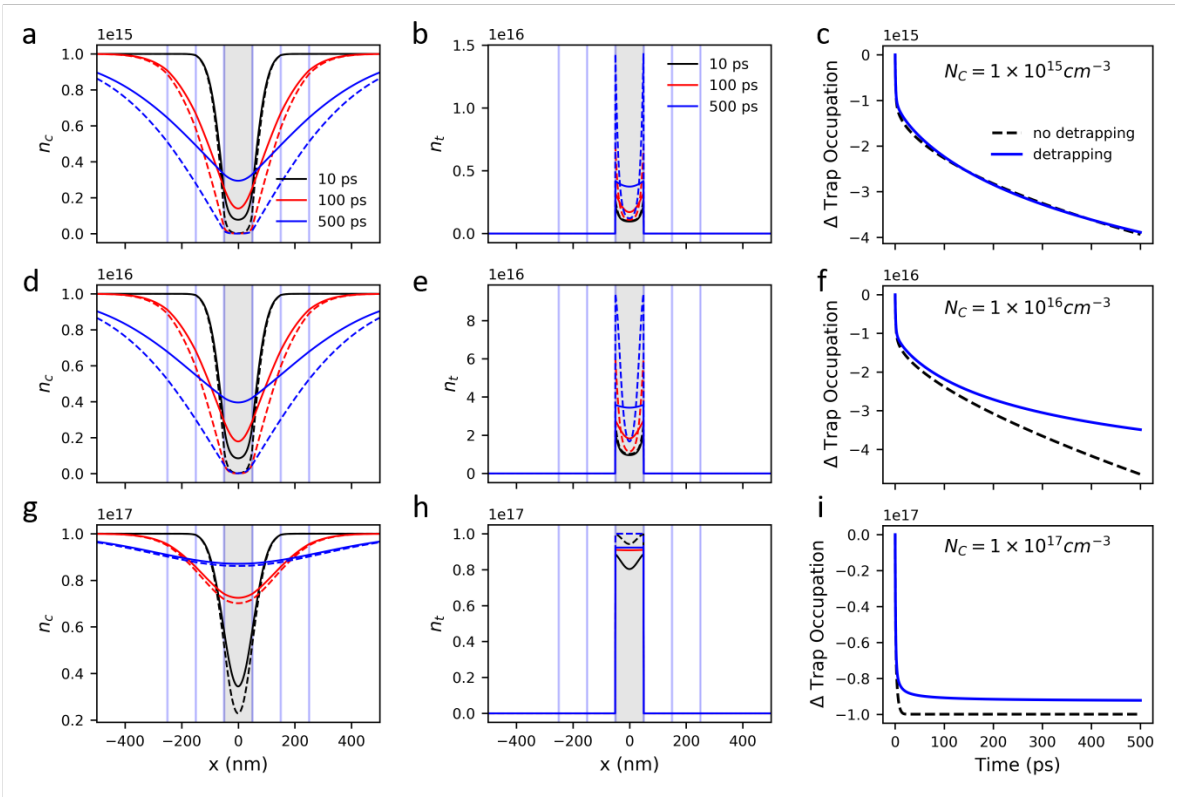

Figure 5.10: 1D simulation of diffusion which includes de-trapping terms. Solid lines are simulations that include de-trapping, while dashed lines are without de-trapping (i.e. $k_{dt} = 0$). The trap density is set to $1 \times 10^{17} cm^{-3}$ for these simulations. a,b) Simulated free carrier density n_c and trapped holes n_T line profiles for initial carrier density $N_C = 1 \times 10^{15} cm^{-3}$. c) Change in trap population against time with and without detrapping term. d,e) Simulations for n_c and n_T with initial carrier density $N_C = 1 \times 10^{16} cm^{-3}$, and f) resulting change in trap population over time. g,h) Simulation of n_c and n_T for $N_C = 1 \times 10^{17} cm^{-3}$ and i) change in trap population over time.

lence band on a hundreds of picosecond timescale [87]. The de-trapping (and eventual recombination with an electron) of the hole is not accounted for in this current model, which will likely create a quasi-steady-state condition where the trap is only partially filled with holes.

To test this, the model in equation 5.7 can be extended by including terms for de-trapping, given by $\pm k_{dt} n_T (N_V - n_c)$, where k_{dt} is the de-trapping rate constant, N_V is the valence band density of states, and the sign is negative for the first line of equation 5.7 and positive in the second line, to represent trapped holes leaving (returning to) the trap (valence) states. The rate constant k_{dt} is defined in a similar way as before for k_t with a time constant of 400 ps, following the calculations by Li [87], while N_V was taken from estimations in the literature [101]. Simulations for three different initial n_c are shown including the de-trapping terms, and comparing to the case where $k_{dt} = 0$ (i.e. no de-trapping) in figure 5.10. At lower initial carrier densities (N_C), the inclusion of de-trapping (solid lines) prevents the free hole population n_c from being

completely trapped at the trap site (figure 5.10 a) compared to the case without de-trapping (dashed lines). Including de-trapping also slightly changes the spatial profile of the trapped holes (figure 5.10 b) and more evenly distributes the trapped holes (solid versus dashed lines), however the total number of trapped holes is almost exactly the same, as seen in the kinetic trace shown in figure 5.10 c. As the initial carrier density is increased, the spatial profiles do not notably change (figure 5.10 d,e) compared to the low carrier density case, however we see that the time dependence and total number of trapped holes begins to slow down at longer time scales (figure 5.10 f). In the high carrier density case, where the trap quickly saturates, we see that de-trapping doesn't affect the population of free carriers so much (figure 5.10 g), however, it does prevent the trap from completely filling (figure 5.10 h, i). Instead, the trap population reaches an equilibrium between trapping and de-trapping.

Another improvement to the diffusion model here would be to consider a larger dimensional space, either a 2-dimensional lattice of traps and grains, or potentially even a 3-dimensional structure. While these models would more accurately represent the real movement of carriers in the films, they would also greatly increase the computational requirements. Still, it is useful to extend the model to at least 2D, which allows for some further qualitative comparisons to the experimental data. In doing so, I will also introduce a more "complete" model, which properly accounts for the populations of free holes *and* electrons, and allows for electron trapping as well (to allow the trap to eventually relax). This then requires writing a system of three coupled differential equations, similar to equations 5.7 above, as:

$$\begin{aligned}
\frac{dn_e}{dt} &= D_e \bigtriangledown^2 n_e - k_{tr} n_e n_T - k_b n_e n_h \\
\frac{dn_h}{dt} &= D_h \bigtriangledown^2 n_h - k_t n_h (N_T - n_T) + k_{dt} n_T (N_V - n_h) - k_b n_e n_h \\
\frac{dn_T}{dt} &= k_t n_h (N_T - n_T) - k_{dt} n_T (N_V - n_h) - k_{tr} n_e n_T
\end{aligned} \tag{5.8}$$

Where n_e, n_h, and n_T are the populations of free electrons, free holes, and trapped holes, respectively, and $\bigtriangledown^2 = \frac{\partial^2}{\partial x^2} + \frac{\partial^2}{\partial y^2}$ is the Laplacian (in 2D, but can be generalized to 3D as well). The rate constants k are as defined before and schematically shown in figure 5.11 a for the different transitions, with the additional term for electron capture by the trap from the conduction band k_{tr}. Differences in carrier mobility can also be accounted for with D_e and D_h for the electron and hole diffusion coefficients, however for simplicity I will assume $D_e = D_h$ in these simulations, which is a reasonable first approximation for HOIP[15, 100]. For these simulations, I will impose Neumann boundary conditions ("insulated boundaries"), as Dirichlet boundary conditions (e.g. free carrier population equal to a constant) could be difficult to use due to computational limitations from needing to make the simulation area larger than the "excitation" spot.

Before giving the simulation parameters and results, I will also briefly discuss how the trap and grain distributions can be randomly generated to more closely resemble the experimental data, compared to periodic traps and boundaries which are easy

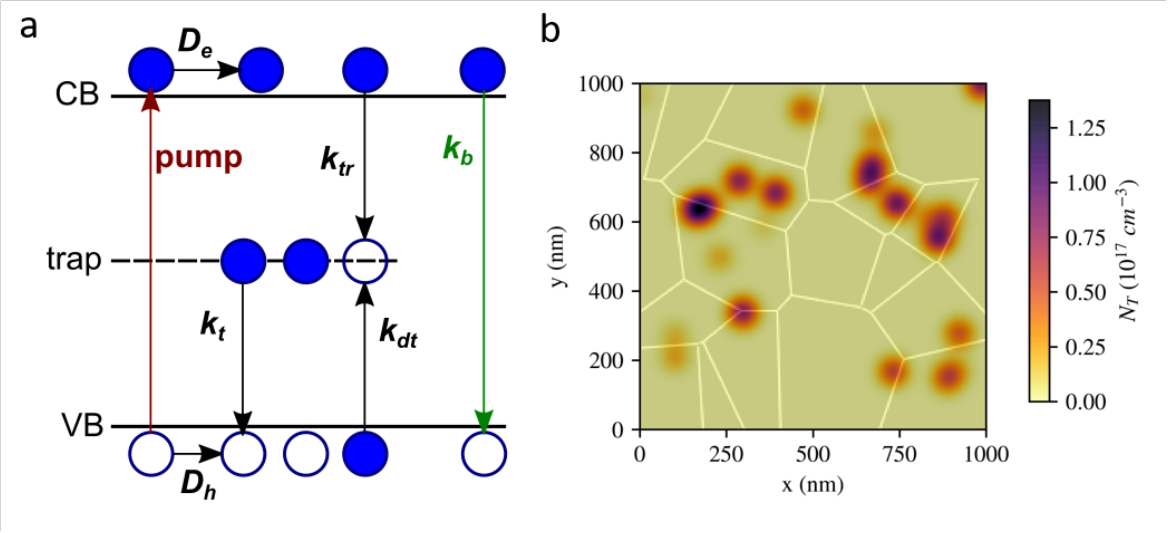

Figure 5.11: Schematic for 2D simulation. a) Kinetic schematic of possible transitions and movements (arrows) between the conduction band (CB), valence band (VB), and the trap states. Electrons are filled blue circles, while holes are hollow. b) Setup for 2D simulation, where the randomly generated trap distribution is overlaid on the random grain distribution made using a Voronoi scheme.

to implement in programming. For the trap distribution, this can be achieved by generating a sparsely populated n-dimensional array, and using those positions as the centers for e.g. a Gaussian trap site, which can then have fixed or variable widths and amplitudes. Making a random grain distribution is slightly more complicated, however it can be readily achieved by constructing a Voronoi diagram (see for example [102]). A Voronoi diagram is seeded in the same way, using a sparsely populated n-dimensional array. A computer algorithm to draw a Voronoi diagram can then be applied, which draws lines perpendicular to the center of a line connecting two seed points. Essentially, it is the same process as drawing a Wigner-Seitz unit cell in condensed matter physics. From a random seed, this results in a random pattern of domains, where as done for the case of the 1-D line simulation, the diffusion coefficient at the boundary of a domain can be reduced to simulate restricted diffusion between grains. Combining these two together, a more realistic random trap-grain structure can be easily generated, as shown for example in figure 5.11 b, where the trap distribution is overlaid on the grain structure. For this image, the size dimensions are 1000 nm in height and width with a step (pixel) size of 5 nm. The trap clusters are 25 randomly seeded Gaussians (which can overlap) of $\sigma = 30$ nm and random amplitudes. The grain distribution is a Voronoi diagram from a seed of 20 random points, where only the resulting domain boundaries (white lines) are shown.

Using the distributions shown in figure 5.11 b, an example simulation in 2D was performed to calculate the free carrier and trapped hole populations using equations 5.8. The remaining parameters for the simulation are as follows: the hole trapping, de-trapping, and electron trapping coefficients (k_t, k_{dt}, and k_{tr}) were set to have time constants of 1 ps, 400 ps, and 300 ns, following the calculations from Li[87] and our

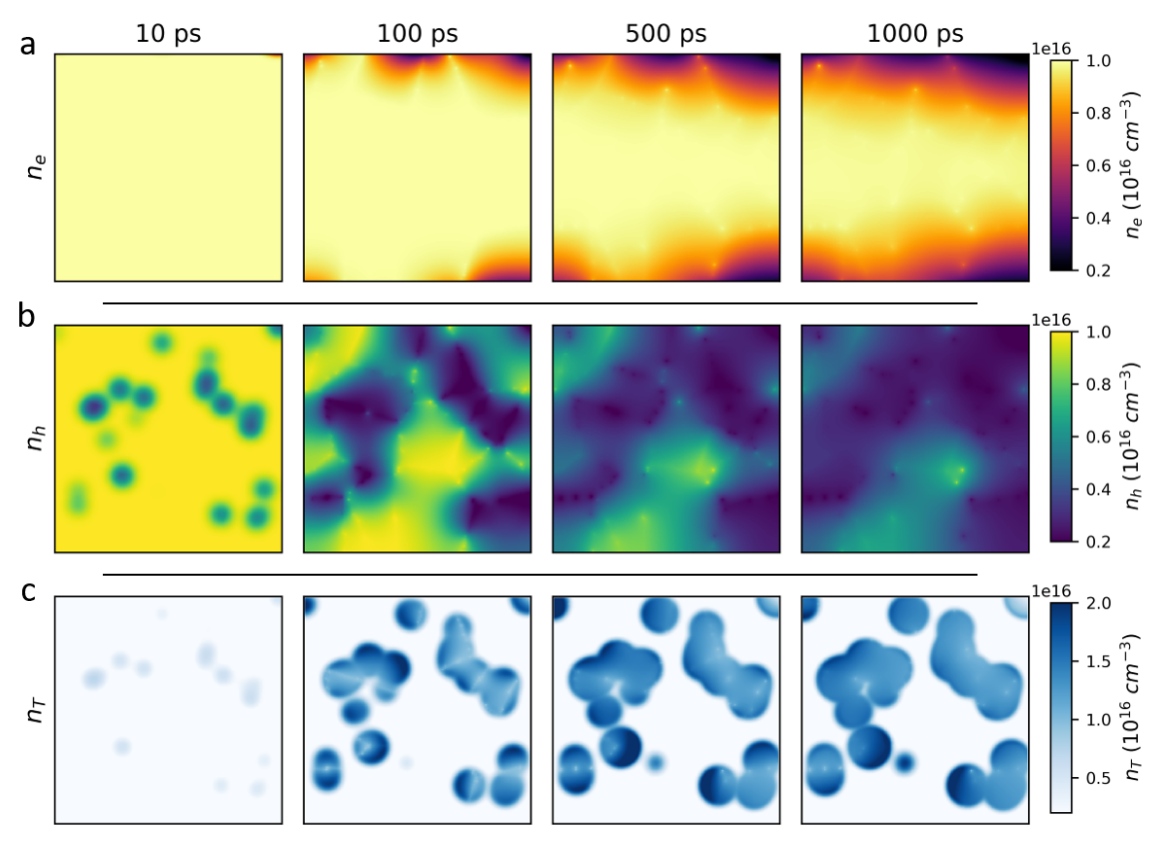

Figure 5.12: Example 2D diffusion simulation using the trap and grain distribution in 5.11 b. a) Free electron population n_e at several time steps. b) Free hole population n_h at several time steps. c) Trapped hole population n_T at several time steps. All images are 1×1 μm in size.

experimental data. The diffusion coefficient within the grains was set to 1 cm^2/s, while the value at the grain boundaries was set to 0.1 cm^2/s. The trap density maximum was set to $N_T = 1 \times 10^{17} cm^{-3}$ (with each trap having a random value; larger values in figure 5.11 b are due to traps overlapping in space). The initial carrier density for both electrons and holes was $N_C = 1 \times 10^{16} cm^{-3}$, and was given a 2D Gaussian profile to resemble the experimental pump laser spot size (roughly, $\sigma_x = 30\mu$m and $\sigma_y = 10\mu$m in simulation), while the traps are initially empty (of holes). The simulation time step was 50 fs, and was run for 20000 steps.

The resulting simulated free electron, free hole, and trapped hole populations in 2D at several time steps are shown in figure 5.12 a, b, and c, respectively. As expected on a sub nanosecond time scale, with the time constant for electron trapping set to 300 ns, there is little change in the free electron population (figure 5.12 a). Note that due to the insulating Neumann boundary condition, there are some artifacts at edges of the simulation near traps; the apparent carrier loss is exaggerated because there is no flow of carriers from outside the simulation area. For the free hole population (figure 5.12 b), we immediately see the effects of carrier diffusion as the time step increases. At longer times, carriers are depleted from whole grains, leading eventually to larger regions of reduced carrier density mediated by grain boundaries. Lastly, for the trapped

holes (figure 5.12 c), we see the number of trapped holes at longer times for each trap cluster is not exactly proportional to its trap density (i.e. comparing to figure 5.11 b), but is also related to the size and position of the grain it sits within, as well as how close other trap clusters are. As a first example, this simulation shows that it should be possible to computationally explore many of the experiments shown in this chapter, as well as potentially from chapter 4. Implications of these simulations, challenges, and some potential research directions will be discussed at the end of the following section.

5.3 Time-resolved discussion

In this chapter, I have discussed in depth experiments and simulations of carrier dynamics in HOIP thin film materials. In section 5.1, I showed the first results of TR-PEEM imaging, where we identified the hole trapping character of the nanoscale trap clusters. Following this, the main portion of this chapter in section 5.2 dealt with discussing possible microscopic recombination mechanisms to explain the observed trapping dynamics, in particular the fluence dependencies described in section 5.2.1. The first mechanism explored was trap-assisted Auger recombination in section 5.2.2, where it was found that this mechanism could potentially explain the trapping kinetics, especially for the higher carrier density regime. However, this model failed to explain the spatial behavior seen in section 5.1, and failed to reproduce the trapping dynamics at lower carrier densities, which is a more important regime for most solar cell devices. Thus, in section 5.2.3, a second mechanism was explored, consisting of a diffusion-limited trapping model. Solutions for this model were computed numerically, allowing for several examples in 1-D to be explored, as well as a first look into a 2-D simulation. I find that the diffusion-limited trapping model can qualitatively reproduce the observed dynamics and observations, making it a potentially more robust or complete model for this system.

Going forward, the diffusion-trapping model proposed in equations 5.8 represent a starting point from which several of our previous experimental observations and conclusions could be tested and explored in more detail, as well as several future research directions. For example, it would be useful to spatially extract the simulated trapping signal from multiple traps to confirm the I_0 vs τ dependence initially observed in section 5.1. Similarly, it could be fruitful to study in some depth how varying the trap distribution (number, size, etc.) affects the trapping kinetics at individual sites, as well as the overall total of carriers which recombine non-radiatively. This would shed deeper insight into how the K-passivation is actually resulting in more efficient HOIP devices. Another interesting point would be to also calculate the total radiative emission (given by the k_b term in equations 5.8) for longer times (i.e. comparable to the carrier "lifetime"), which then provides a simulated 2D PL map. This would solve the issue discussed in section 4.2 when trying to correlate the time-averaged PL map against the nanoscale trap distribution. Lastly, for all of these points, it could be very interesting to use experimental data as a direct input into the model. For example, high-resolution PEEM images of traps and the grain morphology (discussed more in chapter 7) could be used to generate the starting trap grain distributions in the simulations. This should allow for a much more quantitative comparison of the trapping

dynamics, and could provide other useful information such as the ratio of grain to boundary diffusion coefficient and absolute trap densities.

Before jumping to explore these options, there are however a few considerations and limitations with solving equations 5.8 numerically, which I will briefly describe. The main issue comes, in one way or another, down to the time required to run the computation. For the simulations shown in section 5.2.3, the simulation details were picked to keep the total run time on the order of a few minutes (using an ordinary personal computer). To run the same simulation to a final time of, say, a microsecond (for example, to study the PL decay), then the computation time becomes more than 2 days! While the time delta at each step could be increased, there is however a stability limit which must be met, given as $\Delta t \leq \frac{dx^2}{2D}$ (in 1-D) [99], where Δt is the time step of the simulation, dx is the spatial step size, and D is again the diffusion coefficient. For the simulation shown in figure 5.12, with $D = 1$ cm^2/s and $dx = 5$ nm, the stability limit for Δt is 62.5 fs. Therefore, the time step cannot be arbitrarily increased, unless the spatial size or resolution and diffusion coefficients also change. To run larger and/or longer simulations, the computation requirements thus increase dramatically (especially for 2- and 3-D simulations, which can easily contain many more spatial points in the calculations), and either some parameters are sacrificed for optimizing another, or access to high-throughput computing becomes essential. Another route could be to utilize implicit schemes for numerically solving differential equations (as opposed to the explicit scheme used here), which can deal with arbitrary time steps without stability problems. These methods, however, are much more complicated mathematically to utilize, but the payoff could be very useful for doing long-time simulations. Nevertheless, these issues should not prevent future studies using the diffusion-limited trapping model, but do need to be considered seriously when designing each experiment to keep simulations practical while still relevant.

Turning back briefly to the scientific discussion, since the main implications of the effects of carrier diffusion on the recombination losses were already discussed in section 4.3, I will not repeat them in detail here. However, the importance of carrier diffusion in the trapping process highlights that the spatial arrangement of traps is an important factor to consider for modifying recombination losses. For example, by engineering the effect of carrier diffusion across grain boundaries and/or the spatial distribution of traps, it could be possible to limit recombination losses to small (i.e. single grain) portions of the film. For example, additives which prevent carrier diffusion between grains could greatly mitigate the overall number of trapped carriers, which could be beneficial if the traps cannot be completely eliminated during synthesis.

In summary, this work sheds insight into the mechanisms behind the non-radiative recombination losses present in HOIP films, which is not directly accessible by traditional optical time-resolved techniques. In the following chapter 6, I will step back somewhat, and discuss about how PEEM can be used to investigate other interesting phenomenon related to traps in HOIP, namely the effects of light and environmental treatments.

Chapter 6

Light and Environmental Control of Traps

From the identification of nanoscale traps in chapter 3, their relation to radiative carrier losses in chapter 4, and the detailed trapping kinetics discussed in chapter 5, I have provided so far a fairly extensive characterization of the trap properties in mixed cation HOIP films. Following that, in this chapter I want to instead take a slightly different direction, and show how the access to the traps given by TR-PEEM can be used to study other phenomenon in HOIP materials. In particular, there are many reports of environmental and light-induced effects on changing the trap properties in HOIP materials, which I will generally call "light-soaking" effects [26, 83, 85, 90, 91, 103–105]. The ability of our PEEM setup to study the effects of light exposure on traps *in-situ*, as well as after exposures to controlled environments (*ex-situ*), provides us a unique platform to microscopically examine these processes. We recognized this strength after some initial observations during the visit of Stuart Macpherson (Cavendish Laboratory, Cambridge, UK) to our lab in Okinawa, to whom I owe much credit for his ideas and expertise in HOIP materials for this collaborative work. Therefore, I will not focus so much on the underlying physics behind our observations, and instead spend more effort talking about what new information we gain by using PEEM. In section 6.1 I will first discuss the *in-situ* experiments with light exposure under UHV, while in section 6.2 I will discuss observations after controlled exposure to oxygen (O_2) and light.

6.1 In-situ light exposure

Considering the extensive literature on HOIP materials, there have been several reports of light-soaking effects which can modulate the trap densities, leading to either improved or reduced PL emission [26, 85, 103, 105]. However, this is always an inferred effect from the PL efficiency, and is difficult to separate from other effects like halide segregation [90, 91]. Therefore, we use PEEM as a novel probe of the traps in HOIP films and first look at the effects of light-soaking under UHV conditions (10^{-10} torr), where we can rule out environmental factors such as water and oxygen. Following the methodology used in chapter 3, we can monitor both the spatial distribution and photoemission spectra of the traps, while simultaneously light-soaking the film with

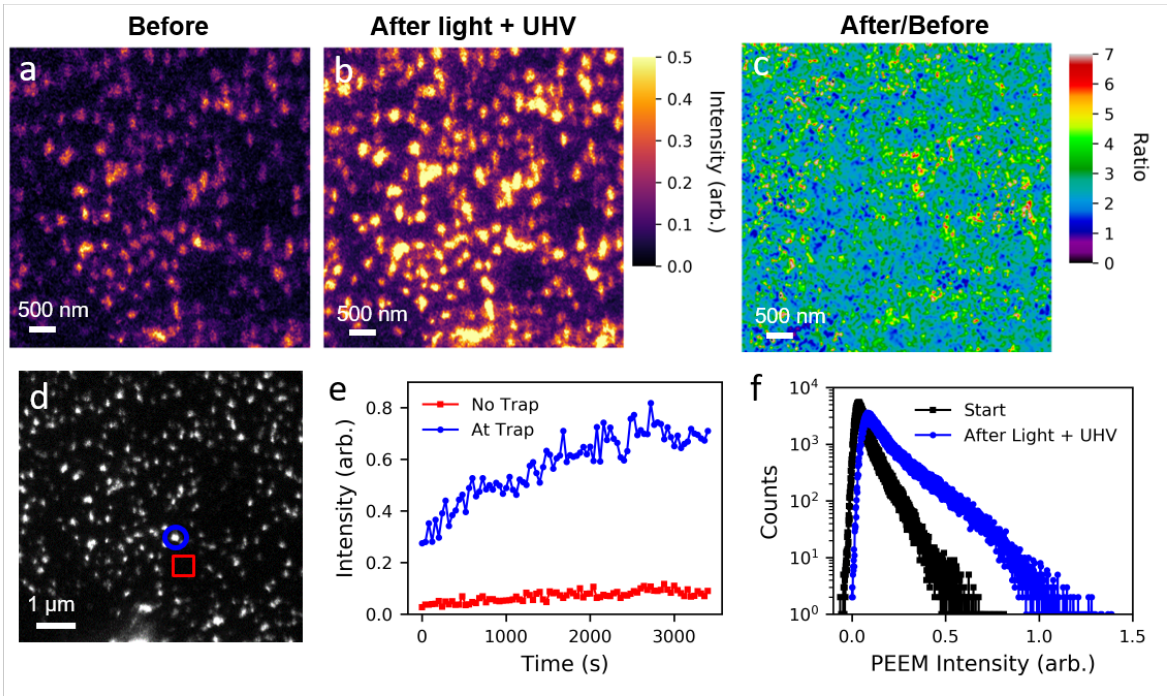

Figure 6.1: PEEM images (energy resolved with 6.2 eV photon energy) of traps in an I-Br sample a) before and b) after light soaking under UHV. The images are scaled to the same intensity range. c) Ratio of image (b) to (a). d) PEEM image of the traps (4.65 eV photon energy). Note that the magnification is different from (a) and (b). e) PEEM intensity over time at the marked locations in (d) during light-soaking. f) Intensity histograms of images (a) and (b).

an external source, e.g. the pump laser used for time resolved experiments (figures 2.2 and 2.5). For this specific experiment, we used 400 nm light from the pump with a moderately high fluence of 10 μJ/cm^2 to light soak, while monitoring the spatial change in photoemission intensity of the traps using the 6.2 eV probe with energy resolved imaging of the trap states. Since the probe fluence is considerably lower (around 10 nJ/cm^2), any probe-induced effects will be negligible. As a technical note, energy resolved imaging during the exposure also makes comparisons of the photoemission spectrum before and after more reproducible, since the analyzer slit does not need to be re-positioned between measurements.

We then monitor the light induced changes in an I-Br sample over the period of about an hour. Correcting for drift of the probe intensity, we can directly compare images at the beginning and end of the exposure (figure 6.1 a and b, respectively). We find that there is a considerable increase in the intensity of the local trap sites, by roughly a factor of two. However, the overall spatial distribution is unchanged; the light soaking does not seem to introduce new local trap sites. We can see this by also looking at the ratio of the two images (figure 6.1 c), where the majority of the image is increased by a factor of two to three, with some local spots of much higher increase, while some regions are relatively unchanged. This can also be tracked for individual regions, such as the single trap and trap free areas marked in figure 6.1 d. From these

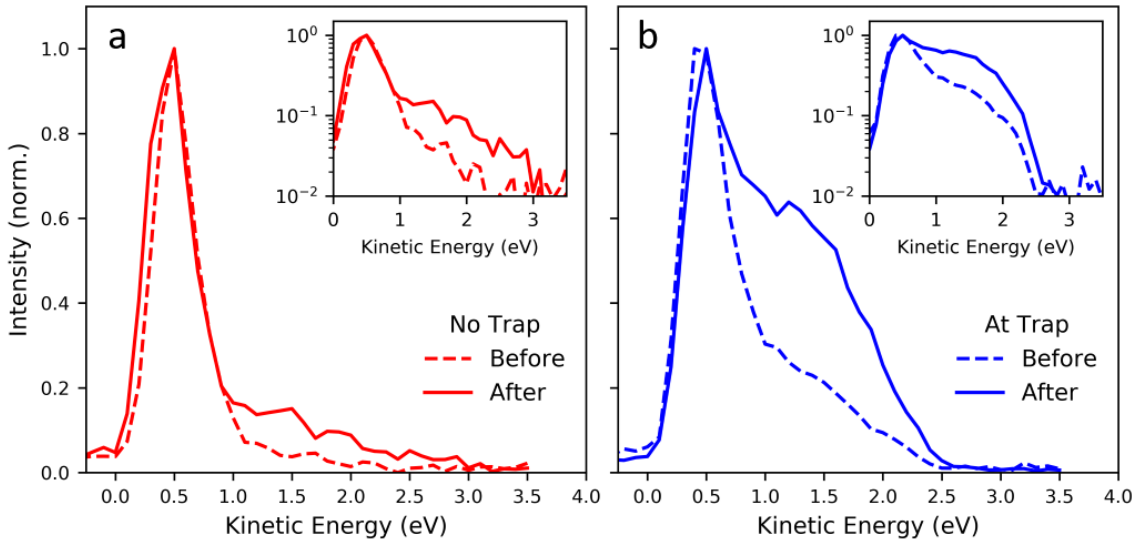

Figure 6.2: Normalized photoemission spectra (6.2 eV photon energy) from a) a trap free area and b) at a local trap, before and after light-soaking in-situ. The insets show the data on a semilog scale.

two spots, we can see that the existing trap has a much larger increase in its total intensity, while the trap free area has only a slight intensity increase (figure 6.1 e). Lastly, we can also consider the total intensity histogram of the two images, which is shifted to higher intensity after light soaking (figure 6.1 f). These first observations reveal that while traps are induced throughout most of the film (figure 6.1 c and f), the effect is strongest at existing trap sites (figure 6.1 e).

We can also see this effect from looking at changes in the photoemission spectrum, taken before and after the light-soaking treatment. Looking at an initially trap free area and a local trap, we can see that in both cases the intensity of mid gap states is increased after light-soaking, relative to the valence band peak (figure 6.2 a and b, respectively). Again, however, we see that the effect, in terms of overall intensity increase, is more significant for the existing trap site (figure 6.2 b). The general features of the spectrum are otherwise mostly unchanged, except for perhaps a small (roughly 100-200 meV) shift in the Fermi level, as evidenced by the slight increase in kinetic energy (figure 6.2 b inset). However, it is difficult to resolve this small change with the imaging conditions used here.

From these observations, we can conclude the following points. First, is that light-soaking under UHV conditions does in fact increase the density of deep level traps, which we would expect to lead to reduced PL efficiency. This directly supports recent studies which observed that under a vacuum environment the PL yield decreases with light soaking [103, 105]. The second point is that the light-soaking does not uniformly increase the trap density; it has a stronger effect at existing trap sites. This suggests that the chemistry behind what forms these trap states favors light-induced reactions, for example such as ion migration or dissociation [26, 90, 91, 104], which are meta-stable for at least several hours under UHV.

While we are still investigating the physics behind the structure and chemistry of these nanoscale traps, as part of the ongoing collaboration between OIST and Cambridge, these initial observations already can provide a new perspective on some of the various light-induced changes often seen in HOIP materials. We further explore this in section 6.2, where we next consider the additional effect of the environment (e.g. oxygen) when light-soaking.

6.2 Ex-situ environmental exposure

As introduced above, several effects of light-soaking on HOIP materials have been observed in the literature. Aside from inducing trap states, there have also been reports where the PL efficiency can *increase* under certain conditions [26, 85, 103], which has interesting consequences for trap management in device fabrication. To test these ideas, we here consider light-soaking in the presence of oxygen gas (O_2), which was recently shown to be a key ingredient for improved PL yield [103, 105]. However, the reported pressures of O_2 needed are relatively high (compared to UHV), and are on the order of at least 10^{-5} torr or higher. Therefore, we are unable to directly study the effects of O_2 gas *in-situ*, where the operating conditions of the microscope demand a pressure of 10^{-7} torr or lower to prevent electrostatic discharge of the sample to the high voltage objective lens, damage to the main channel plate amplification stage, and reduced transmission due to scattering of electrons with gas molecules. Therefore, we chose to do a controlled *ex-situ* exposure to O_2 and light though an external environmental chamber. In this way, we can first measure a sample inside the PEEM, move it to the external environmental chamber for light-soaking in different atmospheres, and then return it to the measurement chamber of the PEEM, all without removing the sample from the PEEM sample holder and without any exposure to the ambient environment. Spatial features such as the deposited gold markers (figure 1.4 a) can then be used to find and measure the same locations before and after the treatments.

Here, we consider the effect of light soaking in the presence of atmospheric pressure O_2 (using dry air). In this case, we light soak with a helium-neon (HeNe) laser at 633 nm for 30 mins with an intensity of around 10 mW/cm^2. Then, we compare PEEM images of the traps (4.65 eV photon energy) before and after the light-soaking, at the same spatial location (figure 6.3 a and b, respectively). Contrary to the results in section 6.1, we see for this case that the intensity of the traps is greatly reduced after treatment with light and O_2. Again, we also see that the spatial distribution of traps remains identical. Looking at the overall intensity histograms (figure 6.3 c) and the image ratio (figure 6.3 d), we see that the trap intensity is reduced to roughly 1/5 after the treatment. In addition, figure 6.3 d also shows that there are local areas where the intensity drops to 1/10 or even lower after treatment.

We also compare the changes in the photoemission spectrum after treatment. Here, for simplicity, we only consider measurements which were spatially averaged over several micrometers in order to reduce the required measurement time and allow for a finer energy step. Following the trend observed from the PEEM images of the traps, we see that there is a significant reduction in the mid gap state intensity after light-soaking in O_2 (figure 6.4 a). In addition, there is an increase in the work function (reduction

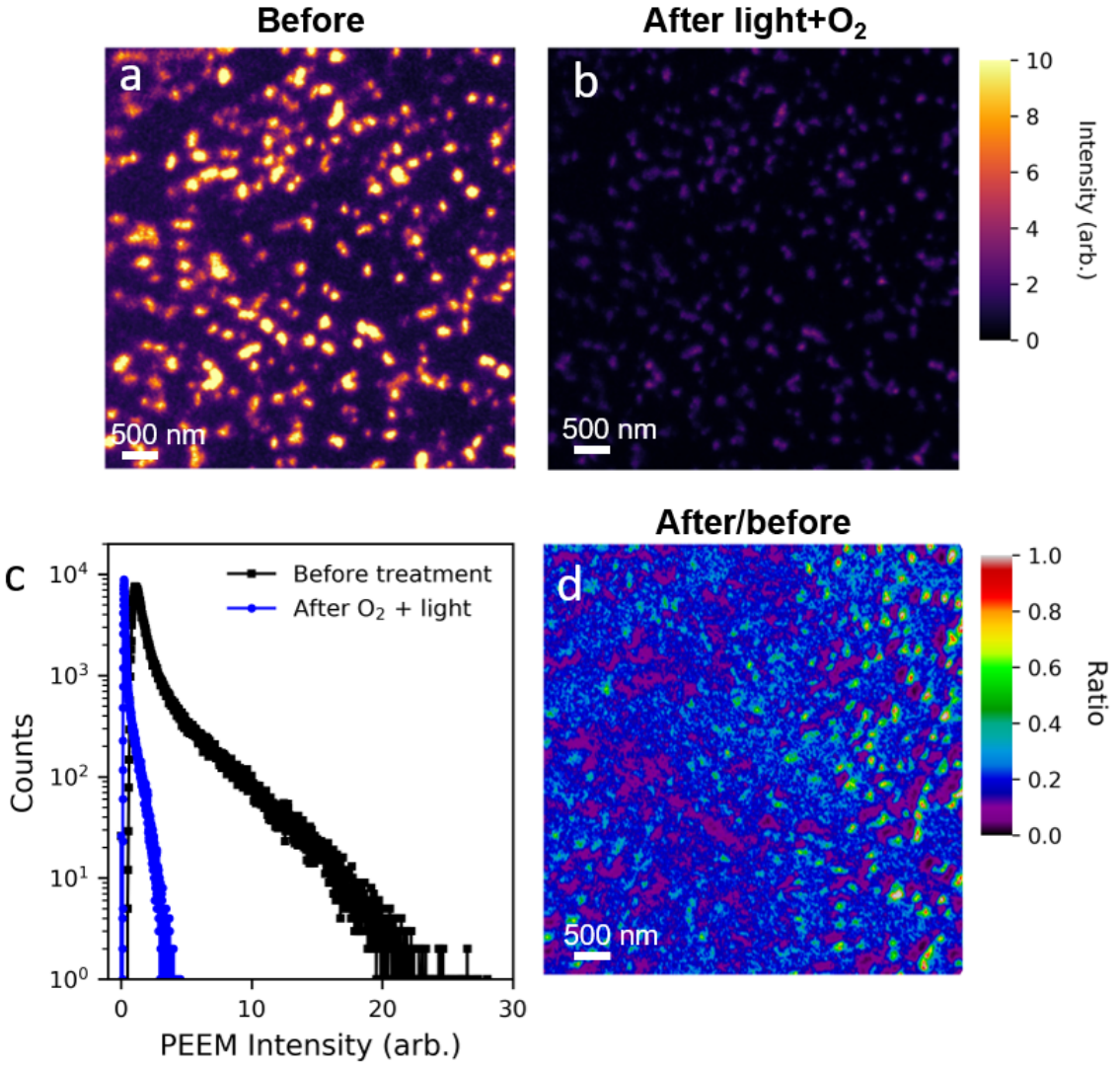

Figure 6.3: PEEM images of traps (4.65 eV probe) in an I-Br sample a) before and b) after light soaking ex-situ in O_2. The images are scaled by laser power and exposure time and plotted on the same intensity scale. Note that these images are taken at the same spatial location. c) Intensity histograms of images (a) and (b). d) Ratio of image (b) to (a). Note that because the sample is removed for the ex-situ soaking, the microscope alignment, and hence image distortions, are slightly different and cause some artifacts when taking the ratio of the images.

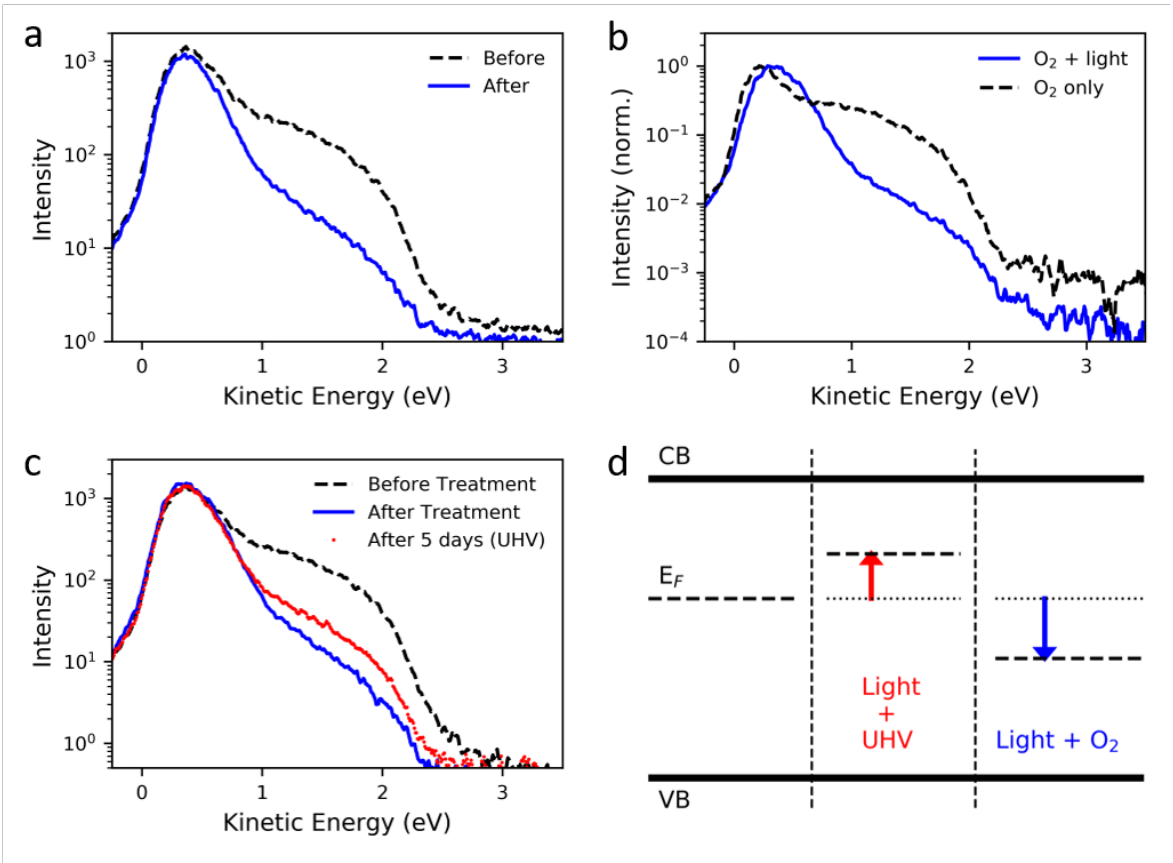

Figure 6.4: a) Photoemission spectra (6.2 eV photon energy), averaged over a 5 μm area, before and after ex-situ light soaking in O_2. The spectrum are scaled by laser power and exposure time. Note that the intensity scale is logarithmic. b) Normalized photoemission spectrum from a sample area exposed to ex-situ light and O_2 compared to an area only exposed to O_2. c) Photoemission spectrum (scaled by laser power and exposure time) of a sample before treatment with O_2 and light, after treatment, and then after 5 days under UHV and dark conditions. d) Energy schematic of the changes in the Fermi level (E_F) under the different light soaking conditions.

in the maximum kinetic energy emitted) of roughly 100-200 meV after the treatment, similar to results from a recent systematic study of water and O_2 exposure [83]. We also check the effect of oxygen exposure in the dark, and we confirm that there is no significant suppression of traps without the addition of light (figure 6.4 b). Lastly, we see that the chemical changes induced through light-soaking in O_2 are stable over several days of storage under UHV in the dark (figure 6.4 c), with only a slow recovery of the mid gap intensity over time. Here again, the increase in the work function is also visible. The general trends in the changing work function (Fermi level E_F) are summarized in figure 6.4 d for the case of light-soaking in vacuum and light-soaking in O_2. As mentioned in section 6.1, the energy shifts after light soaking in vacuum are harder to resolve, but show a slight increase in E_F (decrease in work function), while the treatments with O_2 show the opposite trend.

Our results so far are in agreement with the reaction model proposed by Anaya [103], where Pb reacts with O_2, in the presence of free carriers, to form a superoxide. The superoxide induces ion migration, which redistributes the halide species between the surface and bulk, causing a reduction in the density of surface halide vacancies or interstitial defects [26, 85, 88, 90, 103]. This in turn may also explain our results of light-soaking under UHV, where the light-induced ion migration is now opposite to the case with a layer of superoxides at the surface, causing formation of additional surface defects. However, the interesting point of our results here is that we can spatially visualize where these reactions are happening. We see that the most significant effects happen at the existing trap sites, both for trap formation and passivation. These suggest that the chemistry of the local traps we observe is considerably different than the pristine material.

As a final point, we also show the effects of light-soaking in O_2 on the trapping kinetics. After the light-soaking treatment, we see that there is a significant reduction in the trapping signal measured in TR-PEEM (800 nm excitation). At low pump fluence, the signal vanishes below our sensitivity, while at higher pump fluence we can see that both the amplitude and kinetics are reduced (figure 6.5 a and b, respectively). In particular, following the diffusion-limited trapping model proposed in section 5.2.3, we see that the initial signal at short time delays is reduced in intensity and slows down (figure 6.5 c and d), consistent with SRH trapping kinetics. This shows that light-soaking in O_2 significantly reduces the effect of the mid gap trap states involved in hole trapping.

6.3 Light-treatment Discussion

Thus, in this chapter I have shown how PEEM can be used as a novel method for viewing changes in the nanoscale traps in HOIP films. We have explored two cases of light-induced changes, where light-soaking under UHV conditions induces trap states, while light-soaking in an O_2 environment can passivate the traps. We see that these effects are most significant at existing trap sites, which combined with the local chemical information discussed in section 3.3, suggests that these trap sites are involved with halide migration and/or light-induced chemical reactions, in line with several recent reports in the literature. As part of the ongoing collaborative work for this project,

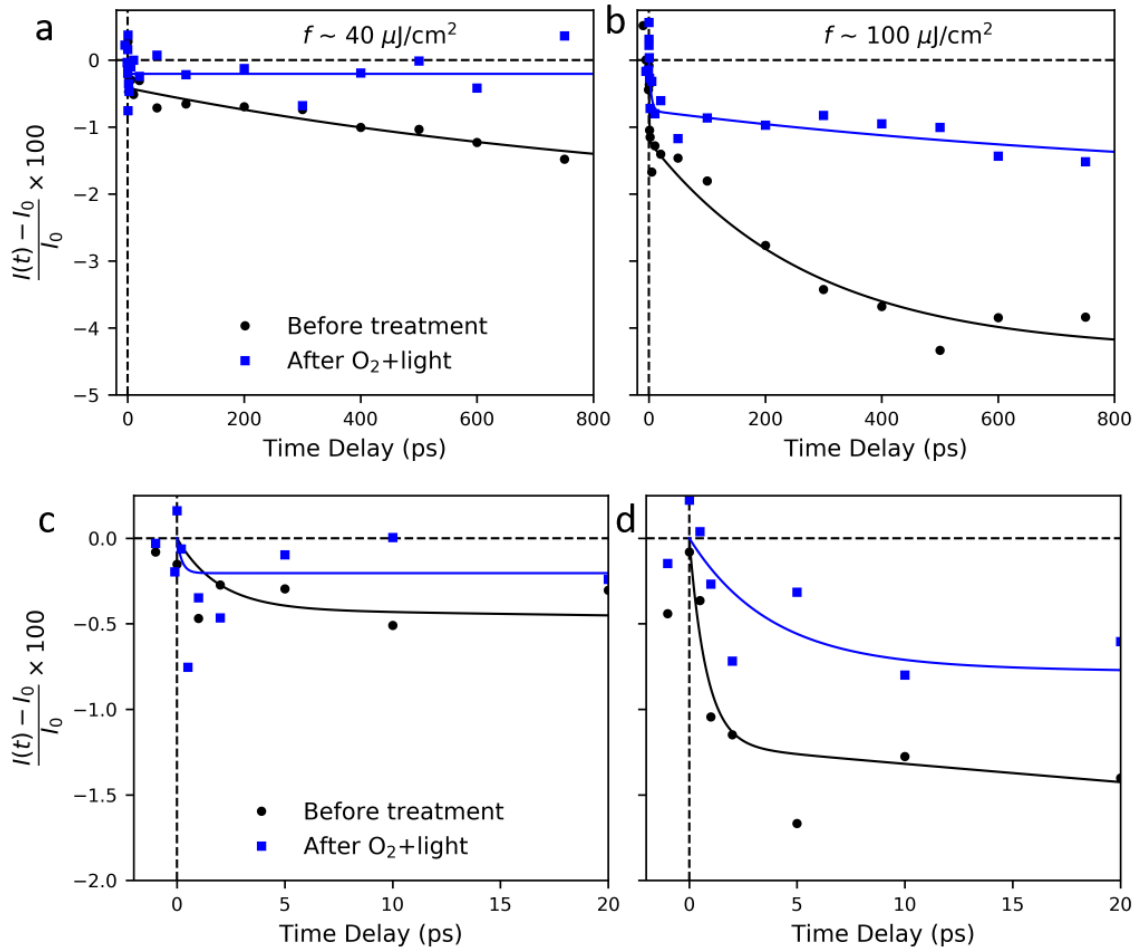

Figure 6.5: TR-PEEM measurement of the trapping dynamics (4.65 eV probe, 1.55 eV pump) in an I-Br sample at a) lower fluence and b) higher fluence, before (black circles) and after (blue squares) ex-situ light soaking in O_2. The solid lines are double exponential fits, as guides to the eye. c, d) Zoomed in views of the dynamics at shorter time delays for (a) and (b), respectively.

future work between OIST and Cambridge will aim to better understand the chemical or structural differences at these trap sites, in particular how they change under different environmental conditions, and how this ultimately influences device properties. For the final part of this thesis, in chapter 7 I will next show how PEEM can also give information about the morphological aspects of the trap sites.

Chapter 7

Film morphology from PEEM

Up to now, I have developed a detailed understanding of the trap sites in mixed cation HOIP films, particularly of their electronic properties and interactions with photoexcited carriers. Following that, in this chapter I want to give some future direction towards studying them from a morphological perspective. As a starting point, one of the unresolved issues in research on deep level traps in HOIP has been on understanding whether they form primarily at grain boundaries, and hence if the grain boundaries will act as centers for recombination [23, 25, 27–30, 106–109]. Due to the limited spatial resolution of optical techniques like PL, which are normally used to infer trap states, and complications due to effects such as carrier diffusion as discuss previously, it becomes beneficial to look to other techniques to accurately locate trap states. As I have shown before in chapter 3, PEEM provides a very powerful tool to identify and study the trap states with a higher spatial resolution than regular optical techniques. However, we also want to be able to relate the trap information to the morphology of the films, in particular to the grain structure. Beyond the point of contention mentioned above, this information will also be very valuable for determining the origins and mechanisms behind the formation of traps in HOIPs. Techniques such as atomic force microscopy (AFM) and scanning electron microscopy (SEM) will of course be indispensable and are already routinely used for examining the grain structure in HOIP films. However, as a surface-sensitive microscopy technique, I want to motivate and show that there is a possibility for PEEM to directly image not only the trap states, but also the grain structure *in-situ*. While there are some challenges with doing this directly in PEEM, it also offers several advantages, which I will discuss more in this chapter.

As a first point, I want to show that PEEM can give information about the surface morphology in HOIP films. In figure 7.1 a I show an AFM image of an iodine-only film, near one of the gold markers, where the grain structure and film morphology can be easily observed. Now, we consider the information we can measure in PEEM. Using the 4.65 eV photon energy, as discussed in chapter 3, only gives photoemission intensity from the trap states. However, the 6.2 eV photon energy was sufficient to photoemit electrons from valence band states. Assuming that the valence band states do not vary dramatically in space, we could expect that imaging this energy range should give information about the surface morphology of the film. Examining the spectroscopic images taken at the valence band peak intensity (figure 7.1 b), we can observe some spatially-varying features. Looking closely, the features resemble grains in the film,

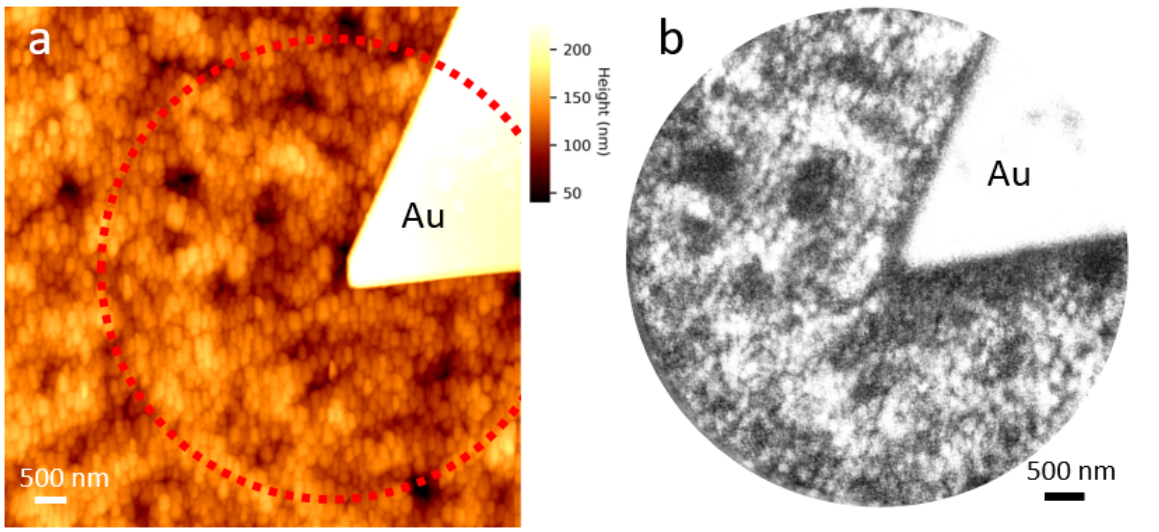

Figure 7.1: Comparison of AFM images to the morphology measured in PEEM. a) AFM image around an Au marker (Bruker Dimension ICON3-OS1707, tapping mode). b) Energy resolved PEEM image (6.2 eV photon energy) of the valence band peak of the region marked by the red dotted line in (a). Note the similarity between the bright and dark regions in PEEM compared to the high and low areas in AFM.

though with some intensity variations. If we compare the PEEM image to the AFM image, which was taken at the same location, then it becomes evident that there is a relation between the film height and the PEEM intensity. At this point, the exact relationship between the two is unclear, however this shows that the energy resolved 6.2 eV probe PEEM images can give similar morphological features as AFM.

Following this observation, I then optimized the PEEM imaging conditions in order to obtain clearer information. For PEEM, in order to obtain higher spatial resolution, we generally want to insert a smaller contrast aperture to restrict the angular distribution and hence reduce the effect of lens aberrations, as discussed in section 2.1.2. However, this presents a challenge for acquiring the images at high magnification, when the photoemission yield is limited by space charge (as discussed in section 2.3.1). For the case of figure 7.1 b, which used a large contrast aperture (essentially open), the integration time for each image (in the spectroscopic series) was 60 seconds with four averages. Reducing the transmitted photoelectrons would then make image acquisition prohibitively long. To balance this, I then use a wider energy analyzer slit, moving from 250 meV to 500 meV, which still allows for energetic separation of the trap states from the valence band states. In this case, the energy resolution loss is not as important for single images, but the larger slit allows for higher transmission. I also optimize the probe beam by reducing its size on the sample as much as possible, while maintaining a similar energy per pulse. This helps to reduce space charge effects from areas of the sample which are illuminated but outside the field of view at high magnification. Lastly, I take many individual image frames, instead of one single acquisition. The images can then be corrected for position drift over time, then averaged off-line.

With these optimizations, I can then obtain much better quality images at high

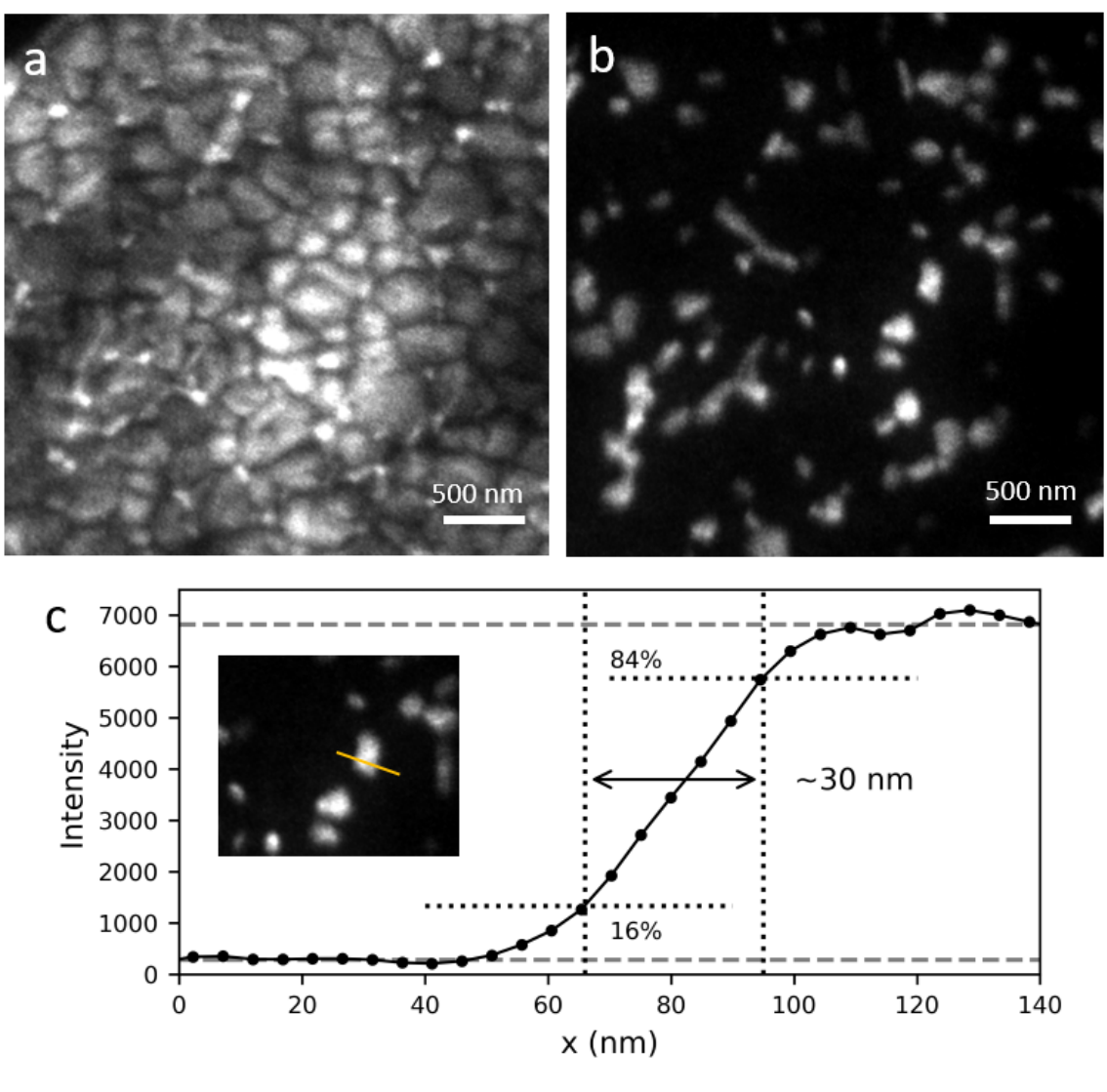

Figure 7.2: High resolution PEEM images (6.2 eV photon energy). a) PEEM image of the valence band peak. b) PEEM image of the mid gap traps at the same location. c) Line profile at the edge of a trap spot (inset), giving a 84-16% resolution of about 30 nm.

magnifications. In figure 7.2 a, I show an optimized image at high magnification of the valence band states of an I-Br sample in PEEM. For this case, the exposure time was 30 seconds with 20 averages, with a 0.57 $Å^{-1}$ diameter contrast aperture and 500 meV wide energy analyzer slit. Despite using the contrast aperture to limit the photoelectron beam, the other optimizations allow for a slight overall increase in the image intensity, which makes the image alignment and acquisition easier. In the end, the information quality is quite good, as many grains can be individually resolved. Following this, the most important advantage of imaging the grains this way in PEEM is that, by simply changing the start voltage of the microscope, the mid gap trap states at a different energy can then be imaged without needing to change any other condition of the microscope except very slightly the focus of the objective lens. Thus, the image of the trap states shown in figure 7.2 b was taken at exactly the same location as figure 7.2 a, without having to move any components or change the microscope alignment. This has the very important advantage that when comparing the images, differences due to lens aberrations and distortions will be minimized and will not need to be explicitly accounted for in the analysis. Additionally, these optimizations also improve the achieved spatial resolution to roughly 30 nm (figure 7.2 c), compared to the 40 nm shown earlier (figure 3.2 a) which was taken without a small contrast aperture.

At this time, the optimized, high resolution images are presented here mainly as a proof of concept. Therefore, I will not go into much detailed discussion about analysis or results, which will explored in depth by other group members in the near future. During the writing of this thesis, in fact, this experiment was pushed further by a junior student (Sofiia Kosar) in our group, who was able to achieve an even better spatial resolution and take very high quality PEEM images. From her analysis, we were able to show that the majority of trap clusters do indeed form at the boundaries of morphological grains. One of the grains at the junction where the trap forms is the compositionally and structurally distorted grain described previously in section 3.3 and in the published work [89]. The fact that the traps are randomly distributed at grain boundaries in the presence of local differences in composition and crystal structure sheds deeper understanding of some recent observations by other groups, where local variations in crystal strain and composition have been correlated with reduced PL emission in mixed cation mixed halide HOIP films [110, 111]. Our PEEM imaging of the formation of trap clusters provides a missing link between variations in the physical crystal properties and the reduction in PL.

Beyond studying just the physical aspects of the traps, it will also be interesting to compare the behavior of photoexcited carriers to the morphology. For example, as discussed in sections 1.2 and 5.2.3, the random connectivity of individual grains has implications for how carriers are trapped over larger areas of the film. Therefore, a combined analysis of the grain morphology, trap position, and high-resolution PL imaging could provide an interesting way to show the true spatial extent of carrier trapping within HOIP films. Thus, combined PEEM imaging of the traps and grain morphology, in conjunction with other complementary techniques, should continue to provide for very interesting futures studies.

Conclusion

At the outset of this thesis work, the overreaching goal was to utilize TR-PEEM as a novel technique to gain a deeper understanding of the nanoscale properties of photoexcited carriers in semiconductor materials. This manifested in the investigation into the properties of traps in hybrid organic inorganic perovksite material, which is a leading candidate for future low cost, flexible, and high efficiency photovoltaic devices. Using TR-PEEM, I was able to investigate the nanoscale distribution of traps and their impact on non-radiative carrier losses in triple cation HOIP materials. As shown in chapters 3 and 4, the deep level traps in these materials have a discreet nanoscale distribution which leads to local trapping of free carriers. Following this, in chapter 5, I discussed two possible mechanisms behind the photohole trapping process at these local sites. Trap assisted Auger recombination and diffusion-limited trapping processes could explain the hole trapping on a picosecond timescale in different carrier density regimes, with the diffusion-limited trapping model showing promise for interesting future studies. Beyond these results, I also showed how the direct access to trap states through PEEM allows for other novel studies. I first showed in chapter 6 the effects of different light treatments for control of the nanoscale traps, while in chapter 7 I explained how morphological information could also be obtained with PEEM for studying the properties of traps related to the film grain structure.

At this time, this work represents the cutting edge work in two separate fields; in applying TR-PEEM as a novel technique in semiconductors, and for studying the properties of traps in HOIP material with high spatial resolution in such a direct manner. This thesis work is one of the first applications of TR-PEEM to study a cutting edge material, and one of only a handful so far to apply the technique in semiconductors. The first work really displaying the possibility of using TR-PEEM to study ultrafast dynamics in semiconductors was published only in 2014 by Fukumoto [60], just over a year before I started working with TR-PEEM. Following this, TR-PEEM has only been successfully applied in a few cutting edge materials systems, such as twisted bilayer graphene by Fukumoto et al. [63], monolayer WSe_2 by Wang et al. [64], and our previous work on indium selenide [65]. Other TR-PEEM work during this time has studied interesting nanoscale phenomenon in more traditional semiconductors [62, 66]. The first publication resulting from my thesis work was recently published[89], and will represent another important milestone for this developing field. This early work on scientifically relevant materials is crucial because it demonstrates the strengths behind how PEEM and TR-PEEM can be utilized with laboratory-based light sources to provide important and new information about nanoscale properties and carrier recombination kinetics. As shown throughout this thesis work, this kind of information

is invaluable for characterizing and understanding the processes behind carrier losses in photovoltaic materials, for example. Therefore, I sincerely hope that my work in the field of PEEM and TR-PEEM will inspire and encourage others to develop and work on such experimental systems. While technically challenging, these kinds of novel techniques will likely play key roles in unveiling nanoscale properties of new materials and will be invaluable for studying novel phenomenon and physics. This is already evident from the increasing interest in TR-PEEM over the last few years, with more and more laboratories and universities seeking to develop their own systems.

At the same time, in the field of HOIP, this work represents an important step forward in understanding the nanoscale properties of traps in triple cation HOIP films. The major finding from my work was the direct observation of a discreet nanoscale arrangement of the deep level traps which are responsible for non-radiative carrier recombination. This work will provide a basis for a deeper microscopic understanding of important carrier loss pathways. Further, through our collaboration with Cambridge[89], we have shown evidence for the underlying chemical and structural variations related to the formation of trap clusters, providing the starting point for targeted research to develop new strategies for controlling traps. Thus, I hope that my work has clarified some of the controversies surrounding traps in HOIP, and will lead to new directions for studying and eventually tackling the issue of carrier traps in HOIP, which will be essential for developing more efficient next-generation solar cell and LED devices.

Bibliography

[1] Chapin, D. M.; Fuller, C. S.; Pearson, G. L. A New Silicon p-n Junction Photocell for Converting Solar Radiation into Electrical Power. *J. Appl. Phys.* **1954**, *25*, 676–677.

[2] Park, J. S.; Kim, S.; Xie, Z.; Walsh, A. Point defect engineering in thin-film solar cells. *Nat. Rev. Mater.* **2018**, *3*, 194–210.

[3] Egger, D. A.; Bera, A.; Cahen, D.; Hodes, G.; Kirchartz, T.; Kronik, L.; Lovrincic, R.; Rappe, A. M.; Reichman, D. R.; Yaffe, O. What Remains Unexplained about the Properties of Halide Perovskites? *Adv. Mater.* **2018**, *30*, 1–11.

[4] Flannigan, D. J.; Zewail, A. H. 4D Electron Microscopy: Principles and Applications. *Acc. Chem. Res.* **2012**, *45*, 1828–1839.

[5] Petek, H. Photoemission electron microscopy: Photovoltaics in action. *Nat. Nanotechnol.* **2017**, *12*, 3–4.

[6] Goldschmidt, V. M. Die Gesetze der Krystallochemie. *Naturwissenschaften* **1926**, *14*, 477–485.

[7] Weber, D. CH3NH3PbX3, ein Pb(II)-System mit kubischer Perowskitstruktur / CH3NH3PbX3, a Pb(II)-System with Cubic Perovskite Structure. *Zeitschrift für Naturforsch. B* **1978**, *33*, 1443–1445.

[8] Akihiro Kojima,; Teshima, K.; Shirai, Y.; Miyasaka, T. Organometal Halide Perovskites as Visible- Light Sensitizers for Photovoltaic Cells. *J Am Chem Soc* **2009**, *131*, 6050–6051.

[9] Kim, H.-S.; Lee, C.-R.; Im, J.-H.; Lee, K.-B.; Moehl, T.; Marchioro, A.; Moon, S.-J.; Humphry-Baker, R.; Yum, J.-H.; Moser, J. E.; Grätzel, M.; Park, N.-G. Lead Iodide Perovskite Sensitized All-Solid-State Submicron Thin Film Mesoscopic Solar Cell with Efficiency Exceeding 9%. *Sci. Rep.* **2012**, *2*, 591.

[10] Lee, M. M.; Teuscher, J.; Miyasaka, T.; Murakami, T. N.; Snaith, H. J. Efficient Hybrid Solar Cells Based on Meso-Superstructured Organometal Halide Perovskites. *Science (80-.).* **2012**, *338*, 643–647.

[11] Snaith, H. J. Perovskites: The Emergence of a New Era for Low-Cost, High-Efficiency Solar Cells. *J. Phys. Chem. Lett.* **2013**, *4*, 3623–3630.

[12] Green, M. A.; Jiang, Y.; Soufiani, A. M.; Ho-Baillie, A. Optical Properties of Photovoltaic Organic-Inorganic Lead Halide Perovskites. *J. Phys. Chem. Lett.* **2015**, *6*, 4774–4785.

[13] Ponseca, C. S.; Savenije, T. J.; Abdellah, M.; Zheng, K.; Yartsev, A.; Pascher, T.; Harlang, T.; Chabera, P.; Pullerits, T.; Stepanov, A.; Wolf, J. P.; Sundström, V. Organometal halide perovskite solar cell materials rationalized: Ultrafast charge generation, high and microsecond-long balanced mobilities, and slow recombination. *J. Am. Chem. Soc.* **2014**, *136*, 5189–5192.

[14] Stranks, S. D.; Eperon, G. E.; Grancini, G.; Menelaou, C.; Alcocer, M. J. P.; Leijtens, T.; Herz, L. M.; Petrozza, A.; Snaith, H. J. Electron-Hole Diffusion Lengths Exceeding 1 Micrometer in an Organometal Trihalide Perovskite Absorber. *Science (80-.).* **2013**, *342*, 341–344.

[15] Xing, G.; Mathews, N.; Sun, S.; Lim, S. S.; Lam, Y. M.; Gratzel, M.; Mhaisalkar, S.; Sum, T. C. Long-Range Balanced Electron- and Hole-Transport Lengths in Organic-Inorganic CH3NH3PbI3. *Science (80-.).* **2013**, *342*, 344–347.

[16] Eperon, G. E.; Stranks, S. D.; Menelaou, C.; Johnston, M. B.; Herz, L. M.; Snaith, H. J. Formamidinium lead trihalide: a broadly tunable perovskite for efficient planar heterojunction solar cells. *Energy Environ. Sci.* **2014**, *7*, 982.

[17] NREL, NREL Best Research-Cell Efficiencies. 2019; `https://www.nrel.gov/pv/assets/pdfs/pv-efficiency-chart.20190103.pdf`.

[18] Richter, J. M.; Abdi-Jalebi, M.; Sadhanala, A.; Tabachnyk, M.; Rivett, J. P.; Pazos-Outón, L. M.; Gödel, K. C.; Price, M.; Deschler, F.; Friend, R. H. Enhancing photoluminescence yields in lead halide perovskites by photon recycling and light out-coupling. *Nat. Commun.* **2016**, *7*.

[19] Stranks, S. D. Nonradiative Losses in Metal Halide Perovskites. *ACS Energy Lett.* **2017**, *2*, 1515–1525.

[20] Pazos-Outón, L. M.; Xiao, T. P.; Yablonovitch, E. Fundamental Efficiency Limit of Lead Iodide Perovskite Solar Cells. *J. Phys. Chem. Lett.* **2018**, *9*, 1703–1711.

[21] Shockley, W.; Read, W. T. Statistics of the Recombinations of Holes and Electrons. *Phys. Rev.* **1952**, *87*, 835–842.

[22] Karpov, S. ABC-model for interpretation of internal quantum efficiency and its droop in III-nitride LEDs: a review. *Opt. Quantum Electron.* **2015**, *47*, 1293–1303.

[23] Draguta, S.; Thakur, S.; Morozov, Y. V.; Wang, Y.; Manser, J. S.; Kamat, P. V.; Kuno, M. Spatially Non-uniform Trap State Densities in Solution-Processed Hybrid Perovskite Thin Films. *J. Phys. Chem. Lett.* **2016**, *7*, 715–721.

[24] Wen, X.; Feng, Y.; Huang, S.; Huang, F.; Cheng, Y.-B.; Green, M.; Ho-Baillie, A. Defect trapping states and charge carrier recombination in organic–inorganic halide perovskites. *J. Mater. Chem. C* **2016**, *4*, 793–800.

[25] de Quilettes, D. W.; Vorpahl, S. M.; Stranks, S. D.; Nagaoka, H.; Eperon, G. E.; Ziffer, M. E.; Snaith, H. J.; Ginger, D. S. Impact of microstructure on local carrier lifetime in perovskite solar cells. *Science (80-.).* **2015**, *348*, 683–686.

[26] DeQuilettes, D. W.; Zhang, W.; Burlakov, V. M.; Graham, D. J.; Leijtens, T.; Osherov, A.; Bulović, V.; Snaith, H. J.; Ginger, D. S.; Stranks, S. D. Photo-induced halide redistribution in organic–inorganic perovskite films. *Nat. Commun.* **2016**, *7*, 11683.

[27] DeQuilettes, D. W.; Jariwala, S.; Burke, S.; Ziffer, M. E.; Wang, J. T.; Snaith, H. J.; Ginger, D. S. Tracking Photoexcited Carriers in Hybrid Perovskite Semiconductors: Trap-Dominated Spatial Heterogeneity and Diffusion. *ACS Nano* **2017**, *11*, 11488–11496.

[28] Yang, M.; Zeng, Y.; Li, Z.; Kim, D. H.; Jiang, C. S.; Van De Lagemaat, J.; Zhu, K. Do grain boundaries dominate non-radiative recombination in CH3NH3PbI3perovskite thin films? *Phys. Chem. Chem. Phys.* **2017**, *19*, 5043–5050.

[29] Tian, W.; Cui, R.; Leng, J.; Liu, J.; Li, Y.; Zhao, C.; Zhang, J.; Deng, W.; Lian, T.; Jin, S. Limiting Perovskite Solar Cell Performance by Heterogeneous Carrier Extraction. *Angew. Chemie Int. Ed.* **2016**, *55*, 13067–13071.

[30] Uratani, H.; Yamashita, K. Charge Carrier Trapping at Surface Defects of Perovskite Solar Cell Absorbers: A First-Principles Study. *J. Phys. Chem. Lett.* **2017**, *8*, 742–746.

[31] Rehman, W.; McMeekin, D. P.; Patel, J. B.; Milot, R. L.; Johnston, M. B.; Snaith, H. J.; Herz, L. M. Photovoltaic mixed-cation lead mixed-halide perovskites: Links between crystallinity, photo-stability and electronic properties. *Energy Environ. Sci.* **2017**, *10*, 361–369.

[32] Saliba, M.; Matsui, T.; Seo, J. Y.; Domanski, K.; Correa-Baena, J. P.; Nazeeruddin, M. K.; Zakeeruddin, S. M.; Tress, W.; Abate, A.; Hagfeldt, A.; Grätzel, M. Cesium-containing triple cation perovskite solar cells: Improved stability, reproducibility and high efficiency. *Energy Environ. Sci.* **2016**, *9*, 1989–1997.

[33] Yi, C.; Luo, J.; Meloni, S.; Boziki, A.; Ashari-Astani, N.; Grätzel, C.; Zakeeruddin, S. M.; Röthlisberger, U.; Grätzel, M. Entropic stabilization of mixed A-cation ABX3metal halide perovskites for high performance perovskite solar cells. *Energy Environ. Sci.* **2016**, *9*, 656–662.

[34] Abdi-Jalebi, M. et al. Maximizing and stabilizing luminescence from halide perovskites with potassium passivation. *Nature* **2018**, *555*, 497–501.

[35] Damascelli, A. Probing the Electronic Structure of Complex Systems by ARPES. *Phys. Scr.* **2004**, *T109*, 61.

[36] Ziaja, B.; London, R. A.; Hajdu, J. Ionization by impact electrons in solids: Electron mean free path fitted over a wide energy range. *J. Appl. Phys.* **2006**, *99*, 033514.

[37] Nguyen-Truong, H. T. Electron inelastic mean free path at energies below 100 eV. *J. Phys. Condens. Matter* **2017**, *29*, 215501.

[38] Bauer, E. Low energy electron microscopy. *Reports Prog. Phys.* **1994**, *57*, 895–938.

[39] Bauer, E. Cathode lens electron microscopy: past and future. *J. Phys. Condens. Matter* **2009**, *21*, 314001.

[40] Bauer, E. *Surf. Microsc. with Low Energy Electrons*; Springer New York: New York, NY, 2014; Vol. 9781493909; pp 1–496.

[41] Menteş, T. O.; Zamborlini, G.; Sala, A.; Locatelli, A. Cathode lens spectromicroscopy: Methodology and applications. *Beilstein J. Nanotechnol.* **2014**, *5*, 1873–1886.

[42] Locatelli, A.; Aballe, L.; Mentes, T. O.; Kiskinova, M.; Bauer, E. Photoemission electron microscopy with chemical sensitivity: SPELEEM methods and applications. *Surf. Interface Anal.* **2006**, *38*, 1554–1557.

[43] Barinov, A.; Dudin, P.; Gregoratti, L.; Locatelli, A.; Onur Menteş, T.; Ángel Niño, M.; Kiskinova, M. Synchrotron-based photoelectron microscopy. *Nucl. Instruments Methods Phys. Res. Sect. A Accel. Spectrometers, Detect. Assoc. Equip.* **2009**, *601*, 195–202.

[44] Sundaram, S. K.; Mazur, E. Inducing and probing non-thermal transitions in semiconductors using femtosecond laser pulses. *Nat. Mater.* **2002**, *1*, 217–224.

[45] Kubo, A.; Pontius, N.; Petek, H. Femtosecond microscopy of surface plasmon polariton wave packet evolution at the silver/vacuum interface. *Nano Lett.* **2007**, *7*, 470–475.

[46] Aeschlimann, M.; Bauer, M.; Bayer, D.; Brixner, T.; Cunovic, S.; Dimler, F.; Fischer, A.; Pfeiffer, W.; Rohmer, M.; Schneider, C.; Steeb, F.; Struber, C.; Voronine, D. V. Spatiotemporal control of nanooptical excitations. *Proc. Natl. Acad. Sci.* **2010**, *107*, 5329–5333.

[47] Kahl, P.; Podbiel, D.; Schneider, C.; Makris, A.; Sindermann, S.; Witt, C.; Kilbane, D.; von Hoegen, M. H.; Aeschlimann, M.; zu Heringdorf, F. M. Direct Observation of Surface Plasmon Polariton Propagation and Interference by Time-Resolved Imaging in Normal-Incidence Two Photon Photoemission Microscopy. *Plasmonics* **2018**, *13*, 239–246.

[48] Ringling, J.; Korn, G.; Squier, J.; Kittelmann, O.; Noack, F. Tunable femtosecond pulses in the near vacuum ultraviolet generated by frequency conversion of amplified Ti:sapphire laser pulses. *Opt. Lett.* **1993**, *18*, 2035.

[49] Rotermund, F.; Petrov, V. Generation of the fourth harmonic of a femtosecond Ti:sapphire laser. *Opt. Lett.* **1998**, *23*, 1040.

[50] Schmidt, O.; Bauer, M.; Wiemann, C.; Porath, R.; Scharte, M.; Andreyev, O.; Schönhense, G.; Aeschlimann, M. Time-resolved two photon photoemission electron microscopy. *Appl. Phys. B* **2002**, *74*, 223–227.

[51] Petek, H.; Sametoglu, V.; Pontius, N.; Kubo, A. Imaging of surface plasmon dynamics in nanostructured silver films. Int. Quantum Electron. Conf. 2005. 2005; pp 112–112.

[52] Cinchetti, M.; Gloskovskii, A.; Nepjiko, S. A.; Schönhense, G.; Rochholz, H.; Kreiter, M. Photoemission Electron Microscopy as a Tool for the Investigation of Optical Near Fields. *Phys. Rev. Lett.* **2005**, *95*, 047601.

[53] Aeschlimann, M.; Bauer, M.; Bayer, D.; Brixner, T.; García De Abajo, F. J.; Pfeiffer, W.; Rohmer, M.; Spindler, C.; Steeb, F. Adaptive subwavelength control of nano-optical fields. *Nature* **2007**, *446*, 301–304.

[54] Chelaru, L. I.; Meyer zu Heringdorf, F.-J. In situ monitoring of surface plasmons in single-crystalline Ag-nanowires. *Surf. Sci.* **2007**, *601*, 4541–4545.

[55] Bayer, D.; Wiemann, C.; Gaier, O.; Bauer, M.; Aeschlimann, M. Time-resolved 2PPE and time-resolved PEEM as a probe of LSP's in silver nanoparticles. *J. Nanomater.* **2008**, *2008*.

[56] Buckanie, N. M.; Kirschbaum, P.; Sindermann, S.; zu Heringdorf, F. J. M. Interaction of light and surface plasmon polaritons in Ag Islands studied by nonlinear photoemission microscopy. *Ultramicroscopy* **2013**, *130*, 49–53.

[57] Dabrowski, M.; Dai, Y.; Argondizzo, A.; Zou, Q.; Cui, X.; Petek, H. Multiphoton Photoemission Microscopy of High-Order Plasmonic Resonances at the Ag/Vacuum and Ag/Si Interfaces of Epitaxial Silver Nanowires. *ACS Photonics* **2016**, *3*, 1704–1713.

[58] Mårsell, E.; Losquin, A.; Svärd, R.; Miranda, M.; Guo, C.; Harth, A.; Lorek, E.; Mauritsson, J.; Arnold, C. L.; Xu, H.; L'Huillier, A.; Mikkelsen, A. Nanoscale Imaging of Local Few-Femtosecond Near-Field Dynamics within a Single Plasmonic Nanoantenna. *Nano Lett.* **2015**, *15*, 6601–6608.

[59] Sun, Q.; Yu, H.; Ueno, K.; Kubo, A.; Matsuo, Y.; Misawa, H. Dissecting the Few-Femtosecond Dephasing Time of Dipole and Quadrupole Modes in Gold Nanoparticles Using Polarized Photoemission Electron Microscopy. *ACS Nano* **2016**, *10*, 3835–3842.

[60] Fukumoto, K.; Yamada, Y.; Onda, K.; Koshihara, S. Y. Direct imaging of electron recombination and transport on a semiconductor surface by femtosecond time-resolved photoemission electron microscopy. *Appl. Phys. Lett.* **2014**, *104*, 0–5.

[61] Fukumoto, K.; Onda, K.; Yamada, Y.; Matsuki, T.; Mukuta, T.; Tanaka, S.-i.; Koshihara, S.-y. Femtosecond time-resolved photoemission electron microscopy for spatiotemporal imaging of photogenerated carrier dynamics in semiconductors. *Rev. Sci. Instrum.* **2014**, *85*, 083705.

[62] Fukumoto, K.; Yamada, Y.; Koshihara, S. Y.; Onda, K. Lifetimes of photogenerated electrons on a GaAs surface affected by nanostructural defects. *Appl. Phys. Express* **2015**, *8*.

[63] Fukumoto, K.; Boutchich, M.; Arezki, H.; Sakurai, K.; Di Felice, D.; Dappe, Y. J.; Onda, K.; ya Koshihara, S. Ultrafast electron dynamics in twisted graphene by femtosecond photoemission electron microscopy. *Carbon N. Y.* **2017**, *124*, 49–56.

[64] Wang, L.; Xu, C.; Li, M.-Y.; Li, L.-J.; Loh, Z.-H. Unraveling Spatially Heterogeneous Ultrafast Carrier Dynamics of Single-Layer WSe 2 by Femtosecond Time-Resolved Photoemission Electron Microscopy. *Nano Lett.* **2018**, *18*, 5172–5178.

[65] Man, M. K.; Margiolakis, A.; Deckoff-Jones, S.; Harada, T.; Wong, E. L.; Krishna, M. B. M.; Madéo, J.; Winchester, A.; Lei, S.; Vajtai, R.; Ajayan, P. M.; Dani, K. M. Imaging the motion of electrons across semiconductor heterojunctions. *Nat. Nanotechnol.* **2017**, *12*, 36–40.

[66] Wong, E. L.; Winchester, A. J.; Pareek, V.; Madéo, J.; Man, M. K. L.; Dani, K. M. Pulling apart photoexcited electrons by photoinducing an in-plane surface electric field. *Sci. Adv.* **2018**, *4*, eaat9722.

[67] Gilton, T. L.; Cowin, J. P.; Kubiak, G. D.; Hamza, A. V. Intense surface photoemission: Space charge effects and self-acceleration. *J. Appl. Phys.* **1990**, *68*, 4802–4810.

[68] Buckanie, N. M.; Göhre, J.; Zhou, P.; Von Der Linde, D.; Horn-Von Hoegen, M.; Meyer Zu Heringdorf, F. J. Space charge effects in photoemission electron microscopy using amplified femtosecond laser pulses. *J. Phys. Condens. Matter* **2009**, *21*.

[69] Berndt, M.; Görlich, P. Studies of the Photoemission of Semiconductors. *Phys. status solidi* **1963**, *3*, 963–981.

[70] Faure, J.; Mauchain, J.; Papalazarou, E.; Yan, W.; Pinon, J.; Marsi, M.; Perfetti, L. Full characterization and optimization of a femtosecond ultraviolet laser source for time and angle-resolved photoemission on solid surfaces. *Rev. Sci. Instrum.* **2012**, *83*.

[71] Heyl, C. M.; Güdde, J.; L'Huillier, A.; Höfer, U. High-order harmonic generation with μJ laser pulses at high repetition rates. *J. Phys. B At. Mol. Opt. Phys.* **2012**, *45*, 074020.

[72] Yang, S.-L.; Sobota, J. A.; Kirchmann, P. S.; Shen, Z.-X. Electron propagation from a photo-excited surface: implications for time-resolved photoemission. *Appl. Phys. A* **2014**, *116*, 85–90.

[73] Pan, Y. Y.; Su, Y. H.; Hsu, C. H.; Huang, L. W.; Dou, K. P.; Kaun, C. C. First-Principles Study on Electronic Structures of FAPbX 3 (X = Cl, Br, I) Hybrid Perovskites. *J. Adv. Nanomater.* **2016**, *1*, 33–38.

[74] Nazarenko, O.; Yakunin, S.; Morad, V.; Cherniukh, I.; Kovalenko, M. V. Single crystals of caesium formamidinium lead halide perovskites: Solution growth and gamma dosimetry. *NPG Asia Mater.* **2017**, *9*, e373–8.

[75] Xie, L. Q.; Chen, L.; Nan, Z. A.; Lin, H. X.; Wang, T.; Zhan, D. P.; Yan, J. W.; Mao, B. W.; Tian, Z. Q. Understanding the Cubic Phase Stabilization and Crystallization Kinetics in Mixed Cations and Halides Perovskite Single Crystals. *J. Am. Chem. Soc.* **2017**, *139*, 3320–3323.

[76] Wu, X.; Trinh, M. T.; Niesner, D.; Zhu, H.; Norman, Z.; Owen, J. S.; Yaffe, O.; Kudisch, B. J.; Zhu, X. Y. Trap states in lead iodide perovskites. *J. Am. Chem. Soc.* **2015**, *137*, 2089–2096.

[77] Kong, W.; Ding, T.; Bi, G.; Wu, H. Optical characterizations of the surface states in hybrid lead–halide perovskites. *Phys. Chem. Chem. Phys.* **2016**, *18*, 12626–12632.

[78] Kollár, M.; Ćirić, L.; Dil, J. H.; Weber, A.; Muff, S.; Ronnow, H. M.; Náfrádi, B.; Monnier, B. P.; Luterbacher, J. S.; Forró, L.; Horváth, E. Clean, cleaved surfaces of the photovoltaic perovskite. *Sci. Rep.* **2017**, *7*, 1–4.

[79] Wetzelaer, G.-J. A. H.; Scheepers, M.; Sempere, A. M.; Momblona, C.; Ávila, J.; Bolink, H. J. Trap-Assisted Non-Radiative Recombination in Organic-Inorganic Perovskite Solar Cells. *Adv. Mater.* **2015**, *27*, 1837–1841.

[80] Leijtens, T.; Eperon, G. E.; Barker, A. J.; Grancini, G.; Zhang, W.; Ball, J. M.; Kandada, A. R. S.; Snaith, H. J.; Petrozza, A. Carrier trapping and recombination: The role of defect physics in enhancing the open circuit voltage of metal halide perovskite solar cells. *Energy Environ. Sci.* **2016**, *9*, 3472–3481.

[81] Landi, G.; Neitzert, H. C.; Barone, C.; Mauro, C.; Lang, F.; Albrecht, S.; Rech, B.; Pagano, S. Correlation between Electronic Defect States Distribution and Device Performance of Perovskite Solar Cells. *Adv. Sci.* **2017**, *4*, 1700183.

[82] Heo, S.; Seo, G.; Lee, Y.; Lee, D.; Seol, M.; Lee, J.; Park, J. B.; Kim, K.; Yun, D. J.; Kim, Y. S.; Shin, J. K.; Ahn, T. K.; Nazeeruddin, M. K. Deep level trapped defect analysis in CH3NH3PbI3perovskite solar cells by deep level transient spectroscopy. *Energy Environ. Sci.* **2017**, *10*, 1128–1133.

[83] Ralaiarisoa, M.; Salzmann, I.; Zu, F.; Koch, N. Effect of Water, Oxygen, and Air Exposure on CH 3 NH 3 PbI 3– x Cl x Perovskite Surface Electronic Properties. *Adv. Electron. Mater.* **2018**, *4*, 1800307.

[84] Du, M.-H. Density Functional Calculations of Native Defects in CH 3 NH 3 PbI 3 : Effects of Spin–Orbit Coupling and Self-Interaction Error. *J. Phys. Chem. Lett.* **2015**, *6*, 1461–1466.

[85] Mosconi, E.; Meggiolaro, D.; Snaith, H. J.; Stranks, S. D.; De Angelis, F. Light-induced annihilation of Frenkel defects in organo-lead halide perovskites. *Energy Environ. Sci.* **2016**, *9*, 3180–3187.

[86] Whalley, L. D.; Crespo-Otero, R.; Walsh, A. H-Center and V-Center Defects in Hybrid Halide Perovskites. *ACS Energy Lett.* **2017**, *2*, 2713–2714.

[87] Li, W.; Liu, J.; Bai, F.-Q.; Zhang, H.-X.; Prezhdo, O. V. Hole Trapping by Iodine Interstitial Defects Decreases Free Carrier Losses in Perovskite Solar Cells: A Time-Domain Ab Initio Study. *ACS Energy Lett.* **2017**, *2*, 1270–1278.

[88] Meggiolaro, D.; Motti, S. G.; Mosconi, E.; Barker, A. J.; Ball, J.; Andrea Riccardo Perini, C.; Deschler, F.; Petrozza, A.; De Angelis, F. Iodine chemistry determines the defect tolerance of lead-halide perovskites. *Energy Environ. Sci.* **2018**, *11*, 702–713.

[89] Doherty, T. A. S. et al. Performance-limiting nanoscale trap clusters at grain junctions in halide perovskites. *Nature* **2020**, *580*, 360–366.

[90] Barker, A. J.; Sadhanala, A.; Deschler, F.; Gandini, M.; Senanayak, S. P.; Pearce, P. M.; Mosconi, E.; Pearson, A. J.; Wu, Y.; Srimath Kandada, A. R.; Leijtens, T.; De Angelis, F.; Dutton, S. E.; Petrozza, A.; Friend, R. H. Defect-Assisted Photoinduced Halide Segregation in Mixed-Halide Perovskite Thin Films. *ACS Energy Lett.* **2017**, *2*, 1416–1424.

[91] Hoke, E. T.; Slotcavage, D. J.; Dohner, E. R.; Bowring, A. R.; Karunadasa, H. I.; McGehee, M. D. Reversible photo-induced trap formation in mixed-halide hybrid perovskites for photovoltaics. *Chem. Sci.* **2015**, *6*, 613–617.

[92] Stranks, S. D.; Burlakov, V. M.; Leijtens, T.; Ball, J. M.; Goriely, A.; Snaith, H. J. Recombination Kinetics in Organic-Inorganic Perovskites: Excitons, Free Charge, and Subgap States. *Phys. Rev. Appl.* **2014**, *2*, 034007.

[93] Kirchartz, T.; Markvart, T.; Rau, U.; Egger, D. A. Impact of Small Phonon Energies on the Charge-Carrier Lifetimes in Metal-Halide Perovskites. *J. Phys. Chem. Lett.* **2018**, *9*, 939–946.

[94] Hu, Y. et al. Understanding the Role of Cesium and Rubidium Additives in Perovskite Solar Cells: Trap States, Charge Transport, and Recombination. *Adv. Energy Mater.* **2018**, *8*, 1703057.

[95] Staub, F.; Rau, U.; Kirchartz, T. Statistics of the Auger Recombination of Electrons and Holes via Defect Levels in the Band Gap—Application to Lead-Halide Perovskites. *ACS Omega* **2018**, *3*, 8009–8016.

[96] Polyakov, A. Y.; Smirnov, N. B.; Shchemerov, I. V.; Saranin, D. S.; Le, T. S.; Didenko, S. I.; Kuznetsov, D. V.; Agresti, A.; Pescetelli, S.; Matteocci, F.; Di Carlo, A. Trap states in multication mesoscopic perovskite solar cells: A deep levels transient spectroscopy investigation. *Appl. Phys. Lett.* **2018**, *113*, 263501.

[97] Troughton, J.; Gasparini, N.; Baran, D. Cs 0.15 FA 0.85 PbI 3 perovskite solar cells for concentrator photovoltaic applications. *J. Mater. Chem. A* **2018**, *6*, 21913–21917.

[98] Zou, W. et al. Minimising efficiency roll-off in high-brightness perovskite light-emitting diodes. *Nat. Commun.* **2018**, *9*, 608.

[99] Rahaman, M. M.; Sikdar, M.; Hossain, M. B.; Rahaman, M.; Hossain, M.; Professor, A. Numerical Solution of Diffusion Equation by Finite Difference Method. *IOSR J. Math.* **2015**, *11*, 2278–5728.

[100] Levine, I.; Gupta, S.; Bera, A.; Ceratti, D.; Hodes, G.; Cahen, D.; Guo, D.; Savenije, T. J.; Ávila, J.; Bolink, H. J.; Millo, O.; Azulay, D.; Balberg, I. Can we use time-resolved measurements to get Steady-State Transport data for Halide perovskites? **2018**, *103103*, 1–26.

[101] Sherkar, T. S.; Momblona, C.; Gil-Escrig, L.; Ávila, J.; Sessolo, M.; Bolink, H. J.; Koster, L. J. A. Recombination in Perovskite Solar Cells: Significance of Grain Boundaries, Interface Traps, and Defect Ions. *ACS Energy Lett.* **2017**, *2*, 1214–1222.

[102] Yang, C.-W.; Su, P. Simulation and Investigation of Random Grain-Boundary-Induced Variabilities for Stackable NAND Flash Using 3-D Voronoi Grain Patterns. *IEEE Trans. Electron Devices* **2014**, *61*, 1211–1214.

[103] Anaya, M.; Galisteo-López, J. F.; Calvo, M. E.; Espinós, J. P.; Míguez, H. Origin of Light-Induced Photophysical Effects in Organic Metal Halide Perovskites in the Presence of Oxygen. *J. Phys. Chem. Lett.* **2018**, *9*, 3891–3896.

[104] Kim, G. Y.; Senocrate, A.; Yang, T.-Y.; Gregori, G.; Grätzel, M.; Maier, J. Large tunable photoeffect on ion conduction in halide perovskites and implications for photodecomposition. *Nat. Mater.* **2018**, *17*, 445–449.

[105] Motti, S. G.; Gandini, M.; Barker, A. J.; Ball, J. M.; Srimath Kandada, A. R.; Petrozza, A. Photoinduced Emissive Trap States in Lead Halide Perovskite Semiconductors. *ACS Energy Lett.* **2016**, *1*, 726–730.

[106] Mastroianni, S.; Heinz, F. D.; Im, J.-H.; Veurman, W.; Padilla, M.; Schubert, M. C.; Würfel, U.; Grätzel, M.; Park, N.-G.; Hinsch, A. Analysing the

effect of crystal size and structure in highly efficient CH 3 NH 3 PbI 3 perovskite solar cells by spatially resolved photo- and electroluminescence imaging. *Nanoscale* **2015**, *7*, 19653–19662.

[107] De Marco, N.; Zhou, H.; Chen, Q.; Sun, P.; Liu, Z.; Meng, L.; Yao, E.-P.; Liu, Y.; Schiffer, A.; Yang, Y. Guanidinium: A Route to Enhanced Carrier Lifetime and Open-Circuit Voltage in Hybrid Perovskite Solar Cells. *Nano Lett.* **2016**, *16*, 1009–1016.

[108] Yin, W.-J.; Shi, T.; Yan, Y. Unique Properties of Halide Perovskites as Possible Origins of the Superior Solar Cell Performance. *Adv. Mater.* **2014**, *26*, 4653–4658.

[109] Guo, Y.; Wang, Q.; Saidi, W. A. Structural Stabilities and Electronic Properties of High-Angle Grain Boundaries in Perovskite Cesium Lead Halides. *J. Phys. Chem. C* **2017**, *121*, 1715–1722.

[110] Wieghold, S.; Tresback, J.; Correa-Baena, J.-P.; Hartono, N. T. P.; Sun, S.; Liu, Z.; Layurova, M.; VanOrman, Z. A.; Bieber, A. S.; Thapa, J.; Lai, B.; Cai, Z.; Nienhaus, L.; Buonassisi, T. Halide Heterogeneity Affects Local Charge Carrier Dynamics in Mixed-Ion Lead Perovskite Thin Films. *Chem. Mater.* **2019**, *31*, 3712–3721.

[111] Jones, T. W. et al. Lattice strain causes non-radiative losses in halide perovskites. *Energy Environ. Sci.* **2019**, *12*, 596–606.